Development and Characterization of Chemical Resistant Water Separation Composite Membranes by Using Impermeable Polymer Matrix

by

Afsaneh Khosravi

A Dissertation Presented in Partial Fulfillment
of the Requirements for the Degree
Doctor of Philosophy

Approved September 2016 by the
Graduate Supervisory Committee:

Mary Laura Lind, Chair
Lenore L. Dai
Matthew Green
Jerry Lin
Don Seo

Arizona State University

December 2016

ABSTRACT

Water recovery from impaired sources, such as reclaimed wastewater, brackish groundwater, and ocean water, is imperative as freshwater resources are under great pressure. Complete reuse of urine wastewater is also necessary to sustain life on space exploration missions of greater than one year's duration. Currently, the Water Recovery System (WRS) used on the National Aeronautics and Space Administration (NASA) shuttles recovers only 70% of generated wastewater.[1] Current osmotic processes show high capability to increase water recovery from wastewater. However, commercial reverse osmosis (RO) membranes rapidly degrade when exposed to pretreated urine-containing wastewater. Also, non-ionic small molecules substances (i.e., urea) are very poorly rejected by commercial RO membranes.

In this study, an innovative composite membrane that integrates water-selective molecular sieve particles into a liquid-barrier chemically resistant polymer film is synthetized. This plan manipulates distinctive aspects of the two materials used to create the membranes: (1) the innate permeation and selectivity of the molecular sieves, and (2) the decay-resistant, versatile, and mechanical strength of the liquid-barrier polymer support matrix.

To synthesize the membrane, Linde Type A (LTA) zeolite particles are anchored to the porous substrate, producing a single layer of zeolite particles capable of transporting water through the membrane. Thereafter, coating the chemically resistant latex polymer filled the space between zeolites. Finally, excess polymer was etched from the surface to expose the zeolites to the feed solution. The completed membranes were

tested in reverse osmosis mode with deionized water, sodium chloride, and rhodamine solutions to determine the suitability for water recovery.

The main distinguishing characteristics of the new membrane design compared with current composite membrane include: (1) the use of an impermeable polymer broadens the range of chemical resistant polymers that can be used as the polymer matrix; (2) the use of zeolite particles with specific pore size insures the high rejection of the neutral molecules since water is transported through the zeolite rather than the polymer; (3) the use of latex dispersions, environmentally friendly water based-solutions, as the polymer matrix shares the qualities of low volatile organic compound, low cost, and non-toxicity.

DEDICATION

I dedicate this dissertation to my amazing beloved husband, Daryoush. Thank you for your remarkable patience and support over the course of my research.

To my lovely son, Sepanta, who is my life. Please forgive me for all the hours I spent with my face glued to a computer screen.

To my parents who taught me a love of learning and the confidence that I could achieve any goal in life. To my lovely mother, Akhtar, who spreads love to me from the other side of the world with her calls and encouragement. To the memory of my wonderful father, Jahanshah, whose embrace I have missed since September 23, 2009. Thank you for being such a good example to follow. I will never stop loving you.

ACKNOWLEDGMENTS

First and foremost, I want to express my greatest gratitude to my advisor, Prof. Mary Laura Lind. I appreciate all of her patience, flexibility and guidance to make my doctoral experience productive and stimulating. She has been a tremendous mentor for me throughout the course of my research.

My profound gratitude also extends to all my doctoral committee members, Profs. Lenore L. Dai, Matthew Green, Jerry Lin, and Don Seo for generously providing me with their time and support to improve my work. Every result described in this thesis was accomplished with the help and support of fellow labmates and collaborators, Huidan Yin, Julia A. King, Andrew Dopilka, Katelyn Kline, Alexander Maltagliati, Tony Nguyen, Tianmiao Lai, Pinar Cay Durgun, Heather Jamieson, Stewart Mann, and Yifei Xu. I am grateful for having had the opportunity to work with a team of wonderful colleagues throughout this journey.

I would like to give special thanks to the following professors for use of their scientific instruments: Prof. Jerry Lin for his Langmuir Blodgett instrument and UV-vis spectrophotometer, Prof. Lenore Dai for her differential scanning calorimetry instrument, Prof. Sefaattin Tongay for his Raman instrument, and Prof. Paul Westerhoff for his dynamic light scattering instrument. I gratefully acknowledge the use of facilities within the LeRoy Eyring Center for Solid State Science at Arizona State University. I thank 3M Company for donating the perfluoroalkoxy fluorothermoplastic dispersion and Dow Chemical Company for donating the polyolefin latex solution.

This work was supported by NASA Office of the Chief Technologist's Space Technology Research Opportunity – Early Career Faculty Grant #NNX12AQ45G and Graduate Research Support Program (GRSP) at ASU.

TABLE OF CONTENTS

Page

LIST OF TABLES x

LIST OF FIGURES xi

CHAPTER

1. MOTIVATION AND MAIN IDEA OF THE RESEARCH 1

1.1. Water Shortage 1

1.2. NASA Water Recovery Challenges 2

1.3. Desalination Processes 3

1.3.1. Thermal Processes 4

1.3.2. Membrane Processes 4

1.4. Limitations of Commercial Membranes in Wastewater Treatment 7

1.4.1. Fouling 7

1.4.2. Chemical Degradation of Membrane 9

1.4.3. Low Rejection for Non-Ionic Molecules 9

1.5. Innovative Mixed Matrix Membrane Design 10

1.5.1. Polymer Matrix 11

1.5.2. Molecular Sieve 12

1.5.3. Substrate 13

2. LATEX FILM FORMATION ON POROUS SUBSTRATES 15

2.1. Introduction 15

2.1.1. Latex Film Formation Stages 16

2.1.2. Effective Parameters Influencing Latex Film Formation 20

CHAPTER Page

2.1.3. Effective Parameters to Control the Thickness of Latex Film 21

2.2 Materials 22

2.3. Characterization 24

2.3.1. Measurement of Film Thickness and Particle Size 24

2.3.2. Crystallinity and the Glass Transition Temperatures of Polymers 24

2.3.3. Film Morphology 26

2.3.4. Contact Angle and Surface Tension Measurements 26

2.3.5. Water Flux Measurements 27

2.4. Synthesis of Latex Film on Porous Substrates 27

2.5. Results and Discussion 28

2.5.1. Measurement of Film Thickness 28

2.5.2. Impact of Drying Condition on Latex Film Formation 30

2.5.3. Impact of Substrate Material and Pore Size on Film Formation 34

2.5.4. Comparison of Films Cast on Nonporous and Porous Substrates 34

2.5.5. Combined Role of Pore Size and Hydrophilicity on Latex Film Formation .. 39

2.6. Conclusion 48

3. CHEMICAL RESISTANCE OF MEMBRANE 50

3.1. Introduction 50

3.2. Materials 52

3.3. Methods 52

3.3.1. Preparation of Ersatz Space Mission Wastewaters 52

3.3.2. Fabrication of Stand-Free PVDC Film 52

CHAPTER Page

3.4. Characterization 53

3.5. Result and Discussion 54

3.5.1. ATR-FTIR Results of PVDC 54

3.5.2. ATR-FTIR results of Hypod 56

3.5.3. XRD Results 58

3.5.4. Water Permeation Results 59

4. MOLECULAR SIEVES SYNTHESIS 61

4.1. Introduction 61

4.1.1. Principle of Crystallization 63

4.1.2. Effect of Aging on Crystallization 66

4.2. Materials 69

4.3. Synthesis Procedure 69

4.4. Characterization 71

4.5. Results and Discussion 72

4.5.1. Effect of Reaction Temperature on Zeolite LTA Crystal Size 72

4.5.2. Effect of Reaction Time on Zeolite LTA Crystal Size 74

4.5.3. Effect of Time of Gel Aging On Zeolite LTA Crystal Size 75

4.5.4. Effect of Temperature of Gel Aging on Zeolite LTA Particle Size 78

4.5.5. Effect of Precursor Gel Aging Temperature on Particle Crystallinity 83

4.6. Conclusion 86

5. SYNTHESIS OF INNOVATIVE MIXED MATRIX MEMBRANES 88

5.1. Introduction 88

CHAPTER Page

5.2. Materials 91

5.3. Methods..... 92

5.4. Characterization 93

5.5. Results and Discussion 94

5.5.1. Effective Procedure to Synthesize the Innovative Mixed Matrix Membrane 94

5.5.2. Anchoring Zeolite Particles on Porous Substrate Using Silane Linkages..... 95

5.5.3. Remove Impermeable Polymer Layer from Zeolite Surface..... 105

5.5.4. Permeation Results 107

6. SUMMARY AND FUTURE WORK 111

6.1. Conclusion 111

REFERENCES 113

LIST OF TABLES

Table Page

1-1. One Estimate of Global Water Distribution.[6,7] 1

1-2. Size of the Hydrated Ions[48,49] 13

2-1. Approximate Compositions of the Latexes 22

2-2. Properties of the Porous Substrates Used in this Study 24

2-3. Glass Transition Temperature and Particle Size of Latex Particles 25

2-4. Summary of Drying Conditions of Coated Latex Film on Porous Supports[90] 30

2-5. Contact Angle of Diluted Latex Solutions (6%) on the Porous Substrates[90] 41

3-1. Composition of Ersatz Space Mission Wastewaters Used to Initially Test the Corrosion Resistance of Polymer Latex, Table Reproduced From Jamieson.[110] 53

3-2. Absorption Frequencies of Characteristic Vibrations of PVDC 55

3-3. Absorption Frequencies of Characteristic Vibrations of Hypod 57

4-1. Composition of Synthetized Zeolite from Aged Precursor at Different Temperatures. Based on PANalytical X'Pert HighScore Plus Analysis[192] 85

LIST OF FIGURES

Figure Page

1-1. This Map Shows the State of Freshwater on the Planet on 2007. No Water Scarcity is in the Blue Areas; The Red Areas are in Crisis; The Orange Areas are Approaching or Experiencing Physical Water Scarcity. Image Reproduced From Finkbeiner.[9] 2

1-2. Natural Osmosis vs. Reverse Osmosis, Image Reproduced from Bergman.[24] 5

1-3. Comparing Water Production Cost with Common Desalination Processes, Image Reproduced from Kesieme et al.[26] 6

1-4. Design of Innovative Mixed Matrix Membrane 11

2-1. Schematic Shows Three Stages of Latex Film Formation: (1) Constant Water Evaporation/Homogeneous Drying, (2) Particle Deformation, (3) Particle Coalescence. Image Reproduced From Keddie[50] 16

2-2. Cross Section Schematic of Three Contiguous Spheres of Latex Particles 19

2-3. SEM Images of Porous Substrates Used in this Study 23

2-4. DSC Curves of Latexes Polymers; (a) PTFE, (b) PFA, (c) PVDC and (d) Hypod… 25

2-5. Procedure of Porous Substrate Dip Coating in the Latex Solution 28

2-6. Thickness of PVDC Latex Films Cast on Anodisc Supports as a Function of Total Solid Content of Latex Solution and Dip-Coating Time.[90] 29

2-7. Pure Water Permeation through 600–800 nm PVDC Films on Anodisc Supports. Films are Dried at the Conditions Presented in Table 2-4.[90] 31

2-8. SEM Images of 9% Hypod Films on Anodisc Dried in Different Drying Conditions. (a, d, g) Process A: Dried at 65 °C and 5% RH for 2 h. (b, e, h) Process B: Dried at 22 °C

and 25% RH for 24 h. (c, f, i) Process C: Dried at 22 °C and 95% RH for 24 h, and for 24 h at 22 °C, and 25% RH. 32

2-9. PFA Deformed Particles on Nonporous Substrate (Glass) Dried at 22 °C and 25% RH for 24 h 34

2-10. SEM Images of (a, e) PTFE, (b, f) PFA, (c, g) Hypod and (d, h) PVDC on Glass, a Nonporous Substrate (top) and Anodisc, a Porous Substrate (bottom), Dried for 24 h at 22 °C, 95% RH and then for 24 h at 22 °C, 25% RH.[90] 36

2-11. XRD Patterns of Latex Films and Arrays 38

2-12. SEM Images of Hypod on (a) PSF (Pore Size: <10 nm), (b) Anodisc (Pore Size: 20 nm), (c) Nylon-100 (Pore Size: 100 nm), (d) PVDF (Pore Size: 200nm), PVDC on (e) PSF (Pore Size: <10 nm), (f) Anodisc (Pore Size: 20 nm), (g) nylon-100 (Pore Size: 100 nm), and (h) PVDF (Pore Size: 200nm).[90] 43

2-13. SEM Images of a Cross Section of (a,b) 27% PVDC Film on Anodisc and (c,d) 27% Hypod Film on Anodisc. 45

2-14. Atomic Force Microscopy Images of PVDC and Hypod Films Cast on Anodisc and Glass Substrates 46

2-15. Atomic Force Microscopy Results of PVDC and Hypod Films Cast on Anodisc and Glass Substrates.[90] 47

3-1. Chemical Attack of TFC Membrane by Chlorine (image drawn by Pinar Cay Durgun) 51

3-2. FTIR Spectra of PVDC Film Before and After Exposure to Synthetic Brine 55

Figure Page

3-3. Chemical Structure of Hypod (Ethene-1-Octene Copolymer (Left) and Ethylene Acrylic Acid Copolymer (Right)) 57

3-4. FTIR Spectra of Hypod Film Before and After Exposure to Synthetic Brine 57

3-5. XRD Spectra of PVDC Film Before and After Exposure to Synthetic Brine 58

3-6. XRD Spectra of Hypod Film Before and After Exposure to Synthetic Brine 59

4-1. Zeolite Structure and Pore Size; (a) Zeolite LTA, (b) Zeolite MFI (Reproduced from Ref.[130]) 62

4-2. Solubility and Supersolubility Curve (Redrawn from Ref.[152] 64

4-3. Thermodynamic Effects of Formation of a Second Phase Based on Classical Nucleation Theory: Increase in Interfacial Energy and Decrease in Bulk Free Energy. Image Reproduced From Gebauer[157] 65

4-4. Procedure of Zeolite LTA Synthesis Including Precursor Preparation, Aging, and Hydrothermal Reaction 70

4-5. Effect of Reaction Temperature on Zeolite Particle Size 72

4-6. Effect of Reaction Temperature on Crystallinity of Zeolite Particles 73

4-7. Effect of Reaction Time on Zeolite Particle Size 74

4-8. SEM Images of Zeolite LTA Synthetized with Different Reaction Time 74

4-9. SEM Images Show Effect of Aging the Precursor Gel at Room Temperature on Size and Morphology of Synthetized Zeolite 76

4-10. Effect of Time of Aging at Room Temperature on the Zeolite Particle Size 77

4-11. Effect of Long Room Temperature Aging on Crystallinity of Zeolite Particles, (Reaction: 72 h at 100 ºC) 78

Figure Page

4-12. Effect of Aging Temperature on Zeolite Morphology (Crystallization Conditions: 72 h at 100 ˚C).[192] 79

4-13. Effect of Temperature on Aged Zeolite Particle Size (Crystallization Conditions: 72 h at 100 ˚C). Each Aging Time Consists of Three Replicates. Error Bars Represent the Standard Error of the Mean.[192] 80

4-14. TEM of (a) Unaged Gel, and Gels Aged for Two Weeks at (b) -8 ºC, (c) 8 ºC, and (d) 40 ºC Before Crystallization Reaction at 100 ºC with the Corresponding FFT Electron Diffraction Diagram in the Insets. [192] 83

4-15. Effect of Aging Temperature on Crystallinity of Zeolites Aged for Two Weeks at Different Temperatures (Crystallization Conditions: 72 h at 100 ºC). The Label “A” Indicates the Zeolite LTA Identification Peaks. The Label “X” Indicates the Zeolite X Identification Peaks. 85

4-16. Raman Spectra of Zeolite Precursor Gels Aged for Two Weeks at -20 ˚C, 40 ˚C, and the Unaged Gel. [192] 86

5-1. Schematic of Innovative Mixed Matrix Membrane in which the polymeric barrier film acts as a glue binding the molecular sieve particles. 91

5-2. SEM Images of Zeolite in Composite Membrane Covered by the Impermeable Polymer 94

5-3. Schematic Procedure to Anchor Zeolite LTA to a Porous Substrate Using a Silane Agent (Left, (a), (b), and (c)), and the Mechanism of Reactions between Silane Agent and Zeolite (Right) 98

5-4. Chemical structure of silane agents used in this study 99

Figure Page

5-5. SEM Images showing the LTA Zeolites Anchored to Anodisc Substrate Using Various Silane Agent and Solvents; (a) CPTCS in Toluene, (b) CPTES in Toluene, (c) CPTCS in DMF, (d) CPTES in DMF, (e) APTES in Acetone, and (f) GPTMS in Acetone. 101

5-6. SEM Images of the Zeolite Anchored to Anodisc Substrate Using APTES at Room Temperature through (a) Silanization of Zeolite, (b) Silanization of Anodisc, and (c) Silanization of Both Zeolite and Anodisc 102

5-7. Schematic of Anchoring Zeolite to Not-Smooth Substrate, Image Reproduced from Kulak.[207] 104

5-8. SEM Images of Membrane Cross Section Show (a) High Density of Large Zeolite (1 wt% Loading 6 μm Zeolite) Anchored to Anodisc Substrate Without Aggregation, (b) Aggregation of Small Zeolite (1 wt% Loading of 0.45 μm Zeolite). 104

5-9. PVDC-Zeolite Composite After Chemical Etching by (a) 100% TMSO for 1 min, (b) 40% TMSO for 1 min and (c) 40% TMSO for 2 min..... 106

5-10. SEM Image of PVDC-Zeolite Composite After 20 min Oxygen Plasma 106

5-11. Overall Procedure of Making Innovative Mixed Matrix Membrane; Tethering LTA Zeolites to Anodiscs with Silane linkage, Forming a Latex PVDC Film, and Oxygen Plasma Etching to Remove Excess PVDC. 107

5-12. Permeation Results of the Prepared Membranes. 108

5-13. Defects in Top Layer of Anodisc. 109

MOTIVATION AND MAIN IDEA OF THE RESEARCH

1.1. Water Shortage

Although water, the most essential component to life, covers 72% of earth's surface, about a billion people do not have access to clean water.[2] For drinking use, water should contain less than 250 mg/L; however, 97% of the earth's water is seawater with about 35,000 mg/liter salt.[3] The estimate of global water distribution (Table 1-1) shows that all freshwater—in lakes, rivers, and groundwater—amounts to only 2.5%.[4] Current fresh water supplies are under great pressure (Figure 1-1) with increasing demand and decreasing supply, partly due to global warming and population growth.

Water shortages are not limited to a specific region of the world. In the USA water shortages affects human life, the economy, production of energy, and agriculture. Consequently water shortages lead to increased unemployment and consumer prices.[5] For example, in 2011, the cost of water shortage for the Texas economy was assessed between $3 and $5 billion.

Table 1-1. One Estimate of Global Water Distribution.[6,7]

Water source	Percent of total water	Water source	Percent of total water
Freshwater	2.50	Surface water and other freshwater	1.30
		Groundwater	30.10
		Glaciers and ice caps	68.60
Saline groundwater	0.93		
Saline lakes	0.07		
Oceans	96.50		

The water stress will be worse in near future, the United Nation's "World Water Development Report" stated that by 2025, more than 50% of the world's nations will face water shortages; by 2050, as much as 75% of the world's nations.[8] Therefore, providing potable water for world populations is a serious issue in most part of the world. Reclaimed wastewater, brackish groundwater, and ocean water are alternative sources for the production of fresh water.

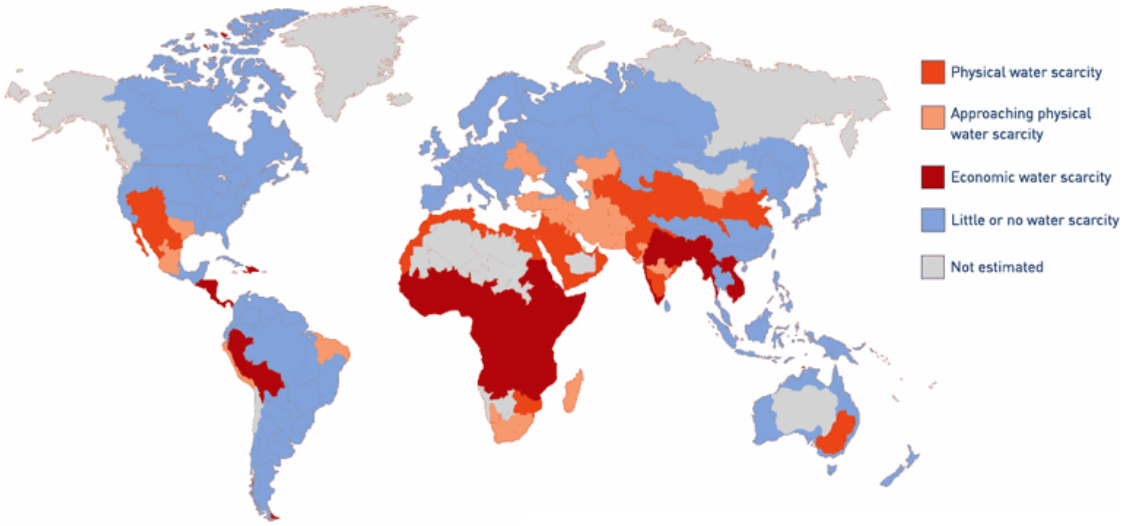


Figure 1-1. This Map Shows the State of Freshwater on the Planet on 2007. No Water Scarcity is in the Blue Areas; The Red Areas are in Crisis; The Orange Areas are Approaching or Experiencing Physical Water Scarcity. Image Reproduced From Finkbeiner.[9]

1.2. NASA Water Recovery Challenges

Water is one of the most vital requirements astronauts need in order to live and work in space. A long mission, such as a stay on the international space station (up to 1 year) or a future trip to Mars that could take roughly one to three years[10], necessitates reducing resupply from Earth. One of the ways to reduce resupply is to recover as much water as

possible from the wastewater generated. The National Aeronautics and Space Administration (NASA) has set a goal of dramatically advancing today's systems for water recovery and management, in the process addressing human health needs as well as the requirements of space flight and travel.[11] A long-term target for NASA is to increase water recovery from wastewater, thereby crafting a closed-loop system for water recycling.[12] Attaining this goal would have substantial positive implications for the existing water recovery system used on the ISS. Although the new water recovery system gives ISS the opportunity to increase the number of crew aboard, only 70% of wastewater generated is recovered; the remaining 30%, brine, must be stored for later disposal.[1] At present, wastewater cannot be recycled without water being resupplied from the ground to the ISS. The space shuttle fleet has been retired, so minimizing the use of ground-based resources has become a higher priority.[13] Consequently, NASA confronts the challenge of optimizing existing wastewater recycling systems, or creating new ones with the capability to maximize water recovery. NASA wastewater is an acidic solution containing several acids which are either naturally in urine or are added to control microbial growth.[1,109]

1.3. Desalination Processes

Desalination refers to a wide range of techniques that can be used to remove dissolved salt from seawater/brackish water in order to producing fresh water. The common processes used throughout the world for seawater desalination include: thermal processes, membrane processes and chemical approaches.[14,15] Ettouney reported that

worldwide, there were more than 12,500 industrial-scale desalination plants, producing fresh water from seawater and brackish water in 2002.[14,16]

1.3.1. Thermal Processes

Thermal desalination (distillation) is one of the most ancient technologies of produce potable water from seawater and brackish water.[17] In thermal desalination, saline source is boiled to produce water vapor and then condensed to form fresh water. Therefore, distillation methods require significant amounts of energy.

The most common thermal desalination processes are: multi-stage flash distillation (MSF), multiple-effect distillation (MED), vapor-compression evaporation (VC), solar water desalination.[17] MED has a high ratio of water produced to steam consumed, with the objective of producing the greatest amount of water with the minimum energy input. While multi-stage flash (MSF) is the most popular technology, it requires more energy than MED.[18]

1.3.2. Membrane Processes

Common membrane processes include reverse osmosis (RO), forward osmosis (FO), nanofiltration (NF), ultrafiltration (UF), microfiltration (MF), electrodialysis (ED), and electrodialysis reversal (EDR).[19] MF membranes only can reject large particles and microorganisms since they have the largest pore size (100 nm - 100 µm).[20,21] UF membranes with the pore size of 1 nm to 100 nm[20] not only reject the large particles and microorganisms, but also they are able to reject soluble macromolecules (i.e. proteins) and bacteria.[21] RO membranes have nonporous structure and eliminate particles and even salt ions, organics.[21]

To understand the osmotic process, comprised of reverse osmosis and forward osmosis, one must first understand osmosis phenomenon. When two different concentration solutions are separated by a semipermeable membrane, water tends to flow from low concentration to high concentration (Figure 1-2). This natural movement will be continued until the chemical potential of the solutions on both sides of the semi-permeable membrane is equal, i.e., when equilibrium is reached.

RO is a process in which water is demineralized or deionized by pushing it under pressure through a semi-permeable membrane. The applied external pressure must be higher than osmotic pressure on the highly concentrated part, in order to force water flow from high concentration to low concentration (Figure 1-2). The semi permeable membrane rejects dissolved contaminations and transport ultra-pure water. While RO requires high hydraulic pressures to pull the water through the membrane, FO works at very low pressure. FO uses osmotic pressure gradient between the feed and the draw solution, a high concentrated solution,[22] to force the water through the membrane.[23]

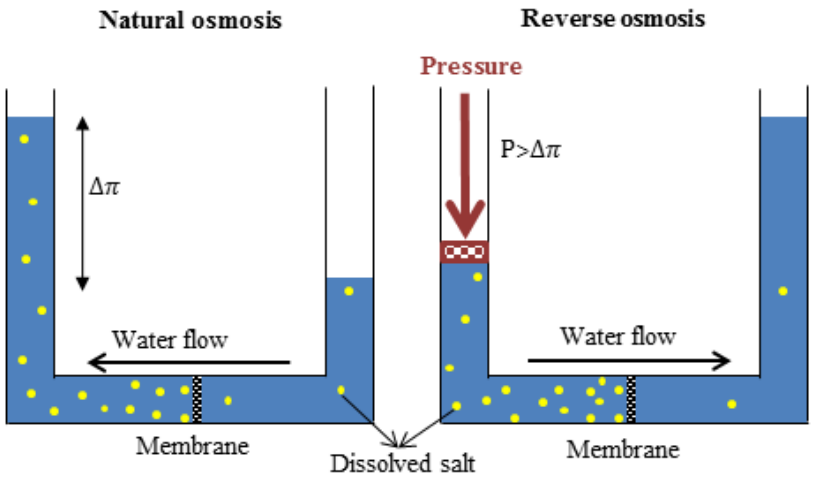


Figure 1-2. Natural Osmosis vs. Reverse Osmosis, Image Reproduced from Bergman.[24]

Today's desalination know-how has contributed to making membrane process very viable in competition with current desalination methods for seawater purification.[25,6,7,15,18] Because the membrane process lacks an evaporation step, it importantly consumes less energy than the thermal desalination processes.[18] The low production cost of membrane separation, arising from its low capital cost, compact size, modular configuration, and low specific power consumption, makes it highly competitive with other processes (Figure 1-3).[25,26]

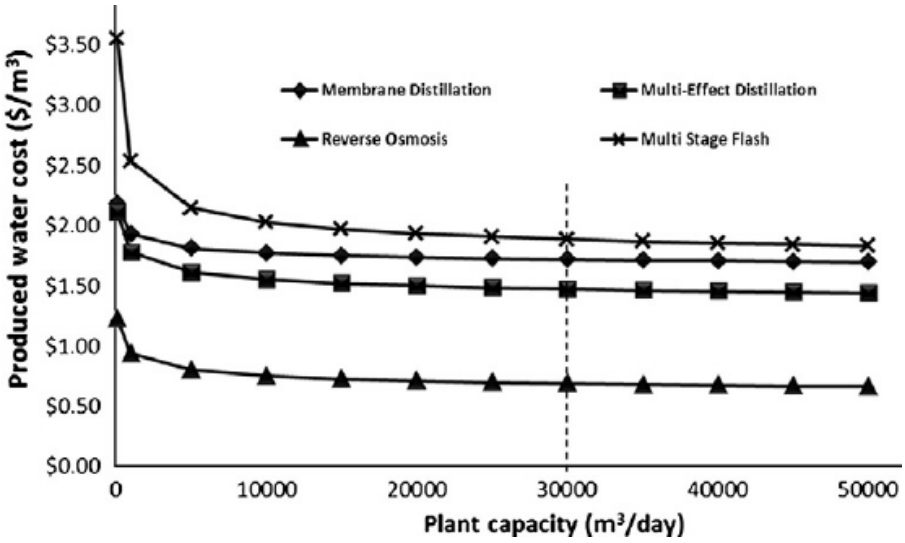


Figure 1-3. Comparing Water Production Cost with Common Desalination Processes, Image Reproduced from Kesieme et al.[26]

As a result of increasing environmental concerns, the osmotic process has earned significant consideration, not only because of its low energy consumption, but also because it plays an important role as augmenter in decreasing greenhouse gases' impact.

1.4. Limitations of Commercial Membranes in Wastewater Treatment

Asymmetric cellulose acetate (CA) membranes were the initial membranes used in RO systems. Although they exhibit high sodium chloride (NaCl) rejection, they require high feed pressures ranging from 1500 to 2000 psig.[27,21] After introduction of the aromatic polyamide thin film composite (TFC) membranes to the RO market, TFC became the dominant choice. Not only do TFC membranes show higher flux and rejection in comparison with CA membranes, TFC membranes also need a lower pressure. For example, for a feed with 2000mg/L NaCl, pH 7.5, a CA membrane displays 97.5% rejection with 27 GFD flux (gallons/ft^2/day), and needs 425 psig feed pressure, while polyamide TFC membrane exhibits 99.5% rejection with 27 GFD flux, and needs only 225 psig feed pressure.[21] The reason for the lower pressure requirement of polyamide TFC membranes is their highly permeable porous substrate such as polysulfone. Although the success of TFC membranes has been proven in the water treatment field, the following issues still require specific attention: membrane fouling, chemical degradation of the polyamide, and low-rejection of non-ionic solutes.[28]

1.4.1. Fouling

Fouling is an increase in hydraulic resistance through the membrane because solute adsorption on membrane surface or blocking of membrane pores. Fouling is a common problem of pressure-driven membrane filtration systems.[29] Fouling results in poor performance of RO membranes especially when they are used for wastewater treatment by decreasing the flux to uneconomical levels.[30] Energy demands on pumping systems are increased by fouling. Furthermore, fouling drives higher costs, for cleanup

and membrane replacement. Fouling increases transmembrane pressure (TMP) if flux is fixed, or will decrease permeate flux if TMP is fixed.[31] The rate of membrane fouling depends on characteristics of the membrane (i.e., roughness, surface charge, and hydrophobicity) and the particle (i.e., size and concentration), membrane hydrodynamics (i.e., crossflow velocity and permeation velocity), and feed solution chemistry (i.e., ionic strength).[8] Fouling is caused by scaling, colloidal particles, dissolved organic substances, and biofouling (microbial growth):[32,33]

- Scaling, depositing salt on the membrane surface, is caused by an increase in concentration of one or more inorganic salts (i.e., calcium carbonate ($CaCO_3$), calcium sulfate ($CaSO_4$), or calcium phosphate ($Ca_3(PO_4)_2$)), greater than their solubility. Scaling can be controlled by injection of antiscaling, decrease the pH, and reducing the recovery rate.[33]
- Colloidal fouling is often driven by bacteria, clay, colloidal silica and iron corrosion products with a size range of a nanometer to a few micrometers.[34,35] Commonly, colloidal fouling is controlled before RO step, during ultrafiltration/microfiltration steps.[33]
- Organic fouling caused by organic compounds, such as natural organic matter (i.e., sugar, amino acids, proteins, polysaccharides, humic substances), is strong and irreversible fouling. Organic fouling is a main problem in wastewater treatment due to higher concentration of orgonic chemicals.[33]
- Biofouling is caused by the adsorption and adhering of living microorganism onto the surface of the membrane and leads to producing a microbial biofilm.[34,35]

Addition of chlorine prevents the microbial growth, however, it degrades the polyamide RO membrane.[33]

1.4.2. Chemical Degradation of Membrane

RO pretreatment and treatment processes typically use chlorine, the most common water disinfectant chemical, before the desalination membrane to control microorganisms that biofoul and clog the membrane. Furthermore, chlorine is usually added to water sources to prevent water-borne diseases.[36] However, current commercially available RO membranes (polyamide based) degrade rapidly with exposure to chlorine.[30] Therefore, to prevent degradation of RO membrane, a pre-treatment dechlorination step is necessary, however, dechlorination prior to the PA membrane creates additional costs to the RO process. There is therefore a need in the art for a chlorine-tolerant composite membrane to tailor the performance and add new functionality to membranes for water purification applications.[37,38] Improving the chemical resistance of RO membrane against chlorine would reduce operation costs by excluding dechlorinating the feed.

1.4.3. Low Rejection for Non-Ionic Molecules

While commercially available RO membranes, charged membranes such as polyamide, demonstrated very high rejection (>99%) for ionic solutes (such as sodium chloride), they have very low rejection for neutral solutes such as urea (~ 20%).[39] Very poor rejection of commercial RO membranes for non-ionic small molecules substances (i.e., urea) leads to complete inapplicability of them in such separations. [40] Therefore,

polyamide membranes are not applied for treatment of urine-containing wastewaters due to the presence of high concentrations of urea.

1.5. Innovative Mixed Matrix Membrane Design

While polymeric membranes offer low cost and good processability, their permeability/selectivity tradeoff (more permeable polymers mostly have less selectivity and vice versa) creates an obstacle to their widespread use. On the other hand, the use of inorganic membranes (i.e., carbon, zeolites, and amorphous oxides) with excellent separation performance, thermal stability, mechanical properties, and chemical resistance, is limited because of their higher expense and low processability. Mixed matrix membranes (MMMs) are created by embedding inorganic particles into a polymer matrix. The act of adding inorganic particles to a polymeric phase is essentially an attempt to synergize the effect of both components by combining the advantages of each phase: the high selectivity and desirable mechanical properties of the dispersed fillers, as well as the economic advantages and ease of processing of polymers.[40] The broad goal of our research is to develop strong MMMs that will fortify the performance and speed up the execution of membrane-based water production technologies.

In the case of corrosive wastewater feed, a polymer matrix of the common MMMs not only should have high permeability and high selectivity, but should have high chemical resistance to feed. These criteria limit the range of polymers that can be used in a polymer matrix, or alternatively, one criterion will have to be passed up in selecting a matrix. We have designed a new class of MMMs in which the matrix is an impermeable chemical-resistant polymer, which binds molecular sieves into a flexible thin polymer

layer (Figure 1-4). By using molecular sieves that are somewhat larger than the expected film thickness, we can ensure that molecular sieves penetrate the entire thickness of the polymer film.[41]

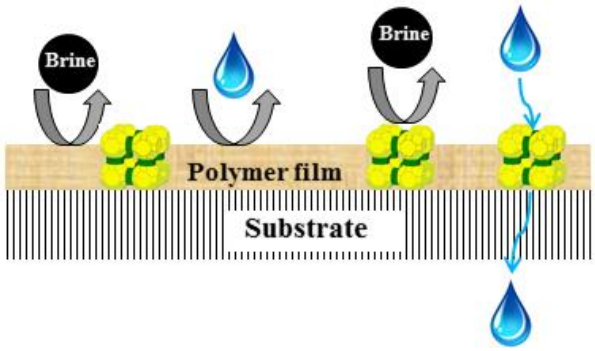


Figure 1-4. Design of Innovative Mixed Matrix Membrane

1.5.1. Polymer Matrix

In the innovative MMM design, the polymer is the matrix for the particles and should have good chemical resistance, since it is exposed to an aggressive feed. A key unique feature of the membrane design is that the polymer does not need to possess permeability/selectivity for water, thereby broadening the range of materials with high chemical resistance that can be selected as the membrane polymer matrix. Therefore, we can use highly chemically resistant polymers regardless of their water permeability as a polymer matrix.

In making our mixed matrix membrane, we use latexes that are submicrometer dispersions of polymer particles in water.[42] Increasing environmental concerns encourages us to use the polymer latex dispersions instead of common polymers that should dissolve in harsh solvents.

1.5.2. Molecular Sieve

Molecular sieves play a significant role in the innovative membrane design because water is transported through the molecular sieves rather than the polymer. Therefore, not only should the molecular sieve particles have good chemical resistance, they also should have high permeability and selectivity for water. We use zeolites, aluminasilica framework structures with uniform pore structure, as the molecular sieves. The pore size of zeolite was the initial primary criterion to choose the most suitable zeolite between 229 different zeolite frameworks. The water molecular diameter is about 2.76 Å - 3.8 Å.[43-46] On the other hand, all water contaminant ions and molecules are larger than 4.5 Å. Urea as the smallest contaminant molecule in the NASA wastewater and has a diameter larger than 5.4 Å (Table 1-2).[47-49] Therefore, the zeolites that the size of their openings is larger than 3.8 Å and smaller than 5.4 Å prepare the suitable pathway for transport the water through the membrane while rejected all contaminant molecules and ions. Therefore, the zeolite LTA which has opening pores of 4.21 × 4.21 × 4.21 Å and MFI (ZSM-5, Silicate-1) which has pores with opening of 4.7× 4.46 × 4.46 Å are suitable candidate as the water-selective particles.

Another criterion for selecting the zeolite type is chemical resistance of zeolite to the feed water. Since zeolites are exposed to the feed water, they should have high chemical resistant to corrosive wastewater. Previous research shows that by increasing the Si/Al ratio, the chemical resistance of the zeolite increases. So, we supposed that silicate-1 (with a Si/Al ratio of infinity) has the highest chemical resistance.

The last criterion, we considered through selection of zeolite type is the symmetry of zeolite particles. As mentioned, in order to ensure that zeolites expose to the feed water,

the zeolite should be slightly larger than the thickness of polymer film. In the other words, the thickness of the polymer film is adjusted corresponding to the zeolite size. However, when zeolite is not symmetrical, it will be complicated to adjust the thickness of the film with zeolite size.

Table 1-2. Size of the Hydrated Ions[48,49]

Ions	Symbol	Crystal diameter [Å]	Hydrated diameter [Å]
Aluminum	Al^{3+}	1	9.5
Lithium	Li^{+}	1.2	7.64
Iron (III)	Fe^{3+}	1.2	9.14
Magnesium	Mg^{2+}	1.3	8.56
Copper	Cu^{2+}	1.44	8.38
Zinc	Zn^{2+}	1.48	8.6
Iron (II)	Fe^{2+}	1.5	8.56
Sodium	Na^{+}	1.9	7.16
Calcium	Ca^{2+}	1.98	8.24
Potassium	K^{+}	2.66	6.62
Ammonium	NH_4^{+}	2.96	6.62
Chloride	Cl^{-}	3.62	6.64
Bromide	Br^{-}	3.9	6.6
Nitrate	NO^{3-}	5.28	6.7
Carbonate	Co_3^{2-}	5.32	7.88
Sulfate	SO_4^{2-}	5.8	7.58

1.5.3. Substrate

The substrate does not require chemical resistance because it is not exposed to the feed; substrate simply provides mechanical strength to the membrane. The main characteristic we considered when selecting porous substrates was their pore size relative

to the average size of the polymer particles in the latex solutions. In general, we selected substrates with characteristic pore sizes that are smaller than the diameters of the polymer particles in the latex solutions we used, so that only the solvent penetrates the substrate. The substrates with various pore size (mesoporous and microporous) and materials (polymeric and inorganic) are potentially suitable for the innovatively designed mixed matrix membrane.

LATEX FILM FORMATION ON POROUS SUBSTRATES

2.1. Introduction

Latex solutions consist of polymer particles dispersed in an aqueous medium.[50] Using water as a solvent has many advantages over organic solvents, including no volatile organic compounds (VOC), reduced odor, inflammability, and nontoxicity.[51,52] Polymer latexes are frequently coated onto solid substrates to make thin films for applications ranging from paint to encapsulated vitamins.[53-55] Although there have been many attempts to define effective parameters to make a defect-free film on nonporous substrates,[56,53,57-66] to date very few of these attempts[60] have been formulated to understand latex film formation onto porous substrates.

Latex film formation on porous substrates (e.g., painting of wood) is commonplace and has both similarities and differences with the system we are studying. However, despite being an everyday household and commercial activity, there is limited scientific literature on this topic, as much of this research is performed within proprietary regimes. Primary differences between our system and that of painting wood are that (1) wood surfaces are rougher[67] than the substrates we studied, (2) wood surfaces have a larger pore size distribution than the surfaces we studied, and (3) wood surfaces swell and shrink significantly based on relative humidity.[68,69] Additionally, many wood surfaces are coated with a priming layer that fills the pores, essentially creating a solid surface that is protected from water sorption prior to paint application.[70]

Our research focuses on latex film formation on uniform porous substrates. The aims of our research were (1) to produce a void-free structure on porous substrates, (2) to

define the effective parameters influencing the thicknesses of formed films, and (3) to evaluate the effects of substrate porosity on latex film formation.

2.1.1. Latex Film Formation Stages

The formation of a continuous polymer film from a latex solution occurs in the three stages (Figure 2-1).

2.1.1.1. Evaporation

Evaporation of the water concentrates the particles into a dense pack of spheres. In this stage, all parts of the film dry at the same rate.[61,64,65]

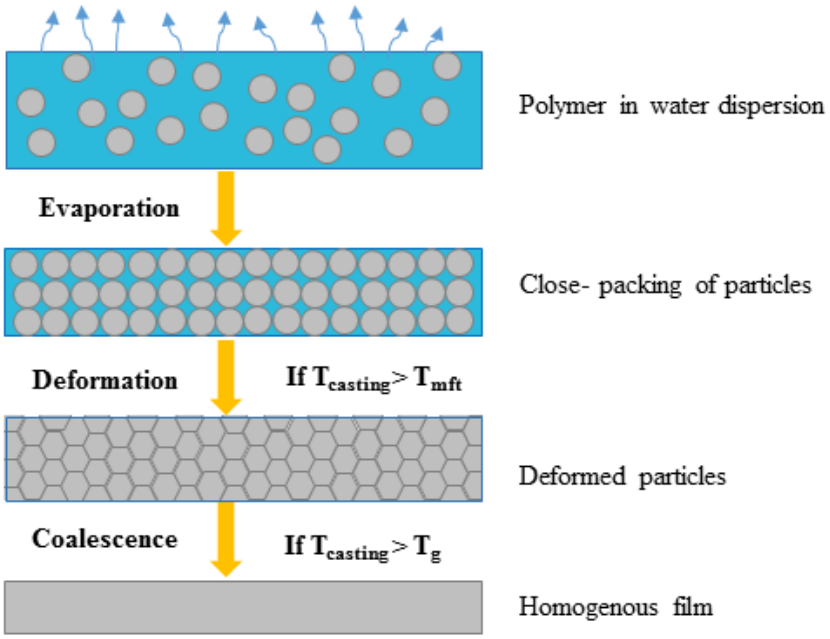


Figure 2-1. Schematic Shows Three Stages of Latex Film Formation: (1) Constant Water Evaporation/Homogeneous Drying, (2) Particle Deformation, (3) Particle Coalescence. Image Reproduced From Keddie[50]

2.1.1.2. Deformation

Through further evaporation, the rate of water evaporation decreases; stage two commences when the particles are initially brought into contact. Capillary pressure induces more particles to enter the liquid menisci arising between the particles. If the capillary pressure is greater than the elastic response of the particles (the polymer's shear modulus), deformation will occur. Deformation force causes the particles to fill the entire space and deform into rhombic dodecahedra, forming a film that is still mechanically weak.[71,64,65,72]

The micromechanical processes during particle deformation have been the subject of considerable debate.[73,74] Many hypotheses have been offered to explain the origin of the deforming forces.[59] Here, we mention four most important theories:

2.1.1.2.1. Wet Sintering (Vanderhoff)

Vanderhoff suggested that the deforming forces result from the pressure created by the interfacial tension (γ_{PW}) of the water and polymer particles with radius of r.[66] So, deformation force is:

$$F \sim \frac{\gamma_{PW}}{r}$$ **Equation 2-1**

2.1.1.2.2. Dry Sintering (Dillon)

Dillon proposed that postulated interfacial tension between the polymer particles and surrounding air (γ_{PA}) drives particle deformation, which occurs after all of the solvent has evaporated.[57]

$$F \sim \frac{\gamma_{PA}}{r}$$ **Equation 2-2**

2.1.1.2.3. Capillary Pressure (Brown)

The capillary theory was proposed by Brown in 1956.[56] Brown stated that the capillary force ensuing from the presence of liquid menisci of negative curvature between closely packed particles is responsible for the polymer particle deformation and film formation. Capillary forces are generated due to water/air interfacial tension (γ_{WA}) during the period of water loss.

Deformation can begin only as soon as the forces that favor film formation, like Van der Waals attraction (F_{vw}), gravity (F_G), surface tension forces (F_s), and capillary forces (F_C) are greater than the repulsive forces, i.e., electrostatic repulsion (Coulombic repulsion) (F_{EL}) and elastic resistance of the particle against deformation (F_R), which are a result of the charged polymer chain end group or surfactant.[71,75]

$$F_{vw} + F_G + F_S + F_C > F_{EL} + F_R$$ **Equation 2-3**

Brown considered F_{vw}, F_G, F_s, and F_{EL} are negligible. The condition reduces then to:

$$F_C > F_R$$ **Equation 2-4**

which is the necessary condition for film formation.[76] Laplace's equation for capillary pressure, created by water stuck between three contiguous spheres of latex particles, is related to the principal radii of curvatures of the shared interface and the interfacial

tension. Considering a system of three contiguous spheres of radius r (Figure 2-2) yields the following relationship for capillary force and elastic resistance force,[56,76]

$$F_C = 12.9\left(\frac{\gamma_{wA}}{r}\right)A$$ **Equation 2-5**

$$F_R = 0.37 G_t A$$ **Equation 2-6**

where γ_{WA} is the water/air interfacial tension, r is the particle radius, A is surface area and G_t is the shear modulus. From these, the condition for film formation is:

$$G_t < 35\frac{\gamma_{wA}}{r}$$ ***Equation 2-7***

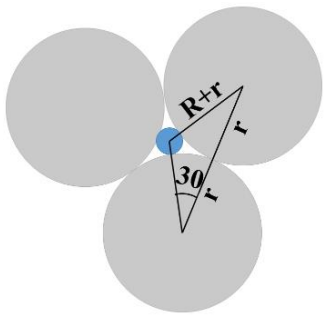


Figure 2-2. Cross Section Schematic of Three Contiguous Spheres of Latex Particles

2.1.1.2.4. Surface Layer Theory (Sheetz)

Sheetz believed that the effect of the capillary forces and wet sintering are limited to the first stages of the coalescence process.[63] In his theory, particle deformation and coalescence must be attributed to the osmotic pressure difference, i.e., that caused by a dry skin layer on top of the wet polymer film. Sheetz suggested the surface layer of latex that dries first forms a membrane. Then, water evaporates by diffusion throughout the

dried layer (membrane), applying a compressive force on the latex particles till the latex film is dry.[59,75,63]

However, none of the theories seem to be universally valid in describing the complicated process of latex film formation. Thus far, current experimental data have not satisfactorily proven either theory.[75]

2.1.1.3. Coalescence

In this stage, the interdiffusion of polymer chains across particle-particle (interparticle) causes the boundaries between the particles disappear, and the original particles are no longer distinguishable.[77,74] Remaining water left in the film would diffuse through capillary channels between the deformed particles or through the polymer itself.[78] Coalescence means the union of two particles which reduces their total surface area and provides the entanglements that give strength to the film. Coalescence arises if drying occurred at temperatures well above its glass transition temperature (T_g). At the end of this stage, film develops its final toughness and strength. [71,79,60,74,73,72] The ultimate physical and mechanical properties of the latex film are defined by the degree to which latex particles can coalesce and fuse into one another.[78] From an energy point of view, the process of coalescence of polymer droplets into a film is favorable, because total surface is minimized, and consequently the free energy decreases.[56]

2.1.2. Effective Parameters Influencing Latex Film Formation

One of the most operative parameters affecting latex film formation is minimum film-forming temperature (T_{mft}). T_{mft} is the minimum temperature at which particles'

deformation and make a void-free film because of the water evaporation force.[80] T_{mft} is usually close to (but not necessarily equal to) the glass temperature T_g of the polymer.[74] Below this critical temperature, the material cannot transform into a homogeneous film, as it remains brittle and turbid.[74] Below T_{mft}, the spheres are too rigid for deformation and coalescence.[81,74] Therefore, soft particles, which have a T_g lower than the casting temperature, easily deform and have polymer chains that readily diffuse.[81] Hard particles, that have a T_g higher than the casting temperature, do not easily deform, and produce ordered arrays of particles.[58,64,65] These materials are termed "non-film-forming latexes".

One other important parameter influencing latex film formation is latex particle size. T_{mft} has been found to increase as a function of latex particle size.[82,76,83,59] Additionally, researchers believe that capillary pressure, the primary force influencing particle deformation, is also a function of latex particle size (Equation 2-5).[56,53]

2.1.3. Effective Parameters to Control the Thickness of Latex Film

A matter of considerable theoretical interest and practical importance is the identification of the parameters that affect the "thickness of deposit"[84] built up on the substrates in a latex dip-coating process. "Thickness of deposit" refers to the total thickness of the polymer film after it is completely dry.[85] Previous research showed the dependency of the dip-coating thickness of latex films on solid surfaces on dipping time[82,84] and coating solution properties (e.g., viscosity,[85,82,84] total solid content,[85] density,[82] concentration,[82] and surface tension[82]). However, paradoxical correlations are reported from these research efforts.[82,84] These results cannot be compared directly because the materials and substrates used differ. For example, Gorton et al.[84] found that

the dry film thickness of rubber deposited on the nonporous substrate relates to the square root of the dipping time and logarithm of viscosity. However, Cisneros et al.[82] showed that the dry film thickness of hydroxypropyl methylcellulose solutions coated on Fuji apples relates to the square root of viscosity and the inverse square root of dipping time.

2.2 Materials

We investigated latex film formation from four different polymer latex solutions: polytetrafluoroethylene (DuPont™ PTFE, Teflon® TE 3859), perfluoroalkoxy fluorothermoplastic (3M™ Dyneon PFA™ 6900G Z), polyvinylidene chloride (Solvay PVDC, PVDC Diofan® B 204), and a polyolefin-based latex (Dow Hypod™ XU 31683). Table 2-1 presents a more specific summary of the compositions of each as-received

Table 2-1. Approximate Compositions of the Latexes

Latex	Components	Concentration (%)
PVDC	PVDC	51
	Surfactant	~9
	Water	~40
Hypod	Ethene-1-octene copolymer	≤ 30
	Ethylene, acrylic acid polymer, potassium salt	≤20
	Water	~60
PTFE	Tetrafluoroethylene	60
	Linear alkyl ethoxylate (based on the PTFE solids)	6
	Water	~34
PFA	Tetrafluoroethylene-Perfluor(Propyl Vinyl Ether) Copolymer	50
	Polyether polymer (nonionic)	7
	Water	~43

commercial latexes solution, as reported from manufacturer's data sheets and communications. Regardless of the specific composition of these commercial latexes (i.e., whether they are homopolymer or copolymer, additives, surfactants), we considered the properties that we measured (T_g, crystallinity, contact angle, and surface tension) as an indicator of their behavior during their film formation.

We used six porous substrates, Al_2O_3 porous ceramic discs (Anodisc), polysulfone (PSF) with a dense skin layer and a molecular weight cutoff of 20 Kd, a nylon substrate with two different pore sizes (100nm and 200nm), polyvinylidene fluoride (PVDF), and polytetrafluoroethylene (laminated PTFE), Polyethersulfone (PES), and one nonporous substrate (borosilicate glass plates). Figure 2-3 and Table 2-2 show the surface morphology and the characteristics of porous substrates used in this study.

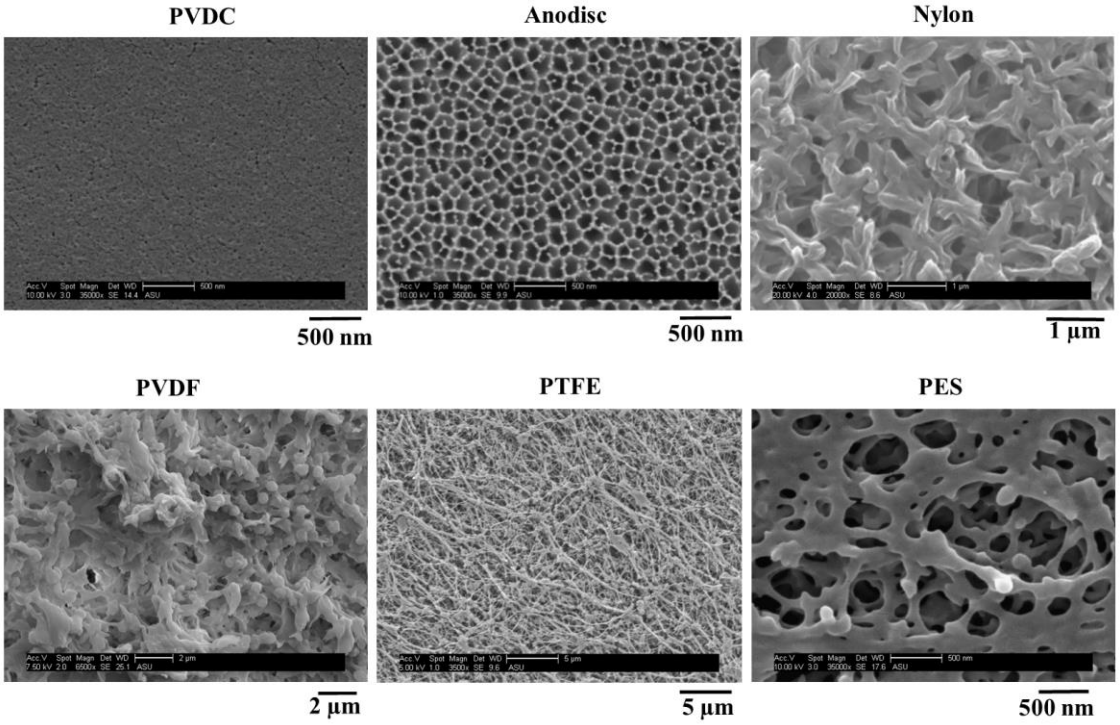


Figure 2-3. SEM Images of Porous Substrates Used in this Study

Table 2-2. Properties of the Porous Substrates Used in this Study

Short name	Chemical name	Manufacturer	Pore size of substrate (nm)
PSF	Polysulfone	Sepro	<10
Anodisc	Aluminium oxide(Al_2O_3)	Whatman	20
Nylon	Polyamide	Sterlitech	100
PVDF	Polyvinylidene fluoride	Sterlitech	200
PTFE	Polytetrafluoroethylene	Sterlitech	200
PES	Polyethersulfone	Sterlitech	300

2.3. Characterization

2.3.1. Measurement of Film Thickness and Particle Size

We used scanning electron microscopy (SEM, FEI/Philips, XL30 ESEM-FEG Hillsboro, USA) to estimate the thickness of the formed films from their cross-sectional SEM images and measured the average particle size of latex particles. To obtain the cross sections, we fractured samples in liquid nitrogen, mounted them on aluminum disks, and then sputter-coated them with gold-palladium. The size of particles reported in Table 2-3.

2.3.2. Crystallinity and the Glass Transition Temperatures of Polymers

We used X-ray diffraction (X'pert Pro, PANalytical, USA) and differential scanning calorimetry (DSC Q20, TA Instruments, USA) to evaluate the extent of crystallinity and the glass transition temperatures of polymers. We used 5–10 mg of dried films of the polymers for the DSC samples. We dried these films in a Pyrex Petri dish at the laboratory conditions (~22 ºC and 25% RH). We ran the DSC scans at a heating rate of 5 ºC/min. Table 2-3 and Figure 2-4 presents the glass transition temperature of the

latex solutions we used. We do not report a T_g for PTFE and PFA because these hard particles are highly crystalline (as shown later in XRD results). With increasing the

Table 2-3. Glass Transition Temperature and Particle Size of Latex Particles

Short name	Chemical name	Manufacturer	Particle size of latex particles (nm)	T_g of latex polymers (°C)
PTFE	Polytetrafluoroethylene	DuPont	150–300	–
PFA	Perfluoroalkoxy fluorothermoplastic	3M	225–245	–
PVDC	Polyvinylidene chloride	Solvay	100–120	12.5
Hypod	Polyolefin-based latex	Dow	100–3000	22

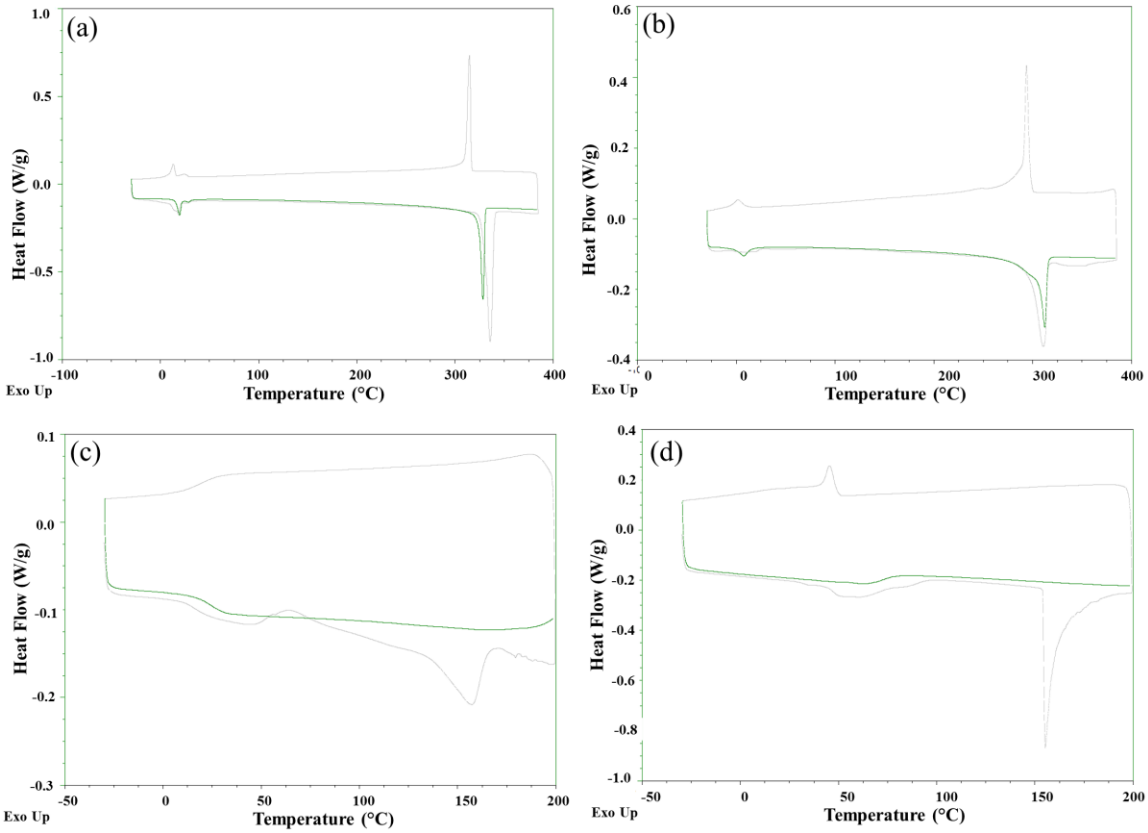


Figure 2-4. DSC Curves of Latexes Polymers; (a) PTFE, (b) PFA, (c) PVDC and (d) Hypod.

crystallinity of the sample, detection of T_g is difficult because the crystalline region restricts the mobility of molecules in the amorphous region; consequently, the deflection temperature at the baseline cannot be defined.[86] Therefore, we were not able to measure the T_g with our DSC.

2.3.3. Film Morphology

We investigated the morphology of the films using SEM and atomic force microscopy (AFM). For SEM surface imaging, we mounted the membranes as for SEM cross sections (mentioned in 2.3.1). We used tapping mode atomic force microscopy (Dimension 3000 AFM, Digital Instruments, USA) to measure the average roughness, root mean squared roughness (RMS), and surface area difference (SAD) of the latex film surfaces. We performed all of the AFM measurements under ambient conditions and without any sample pretreatment. We analyzed three measurements in each of the duplicate samples.

2.3.4. Contact Angle and Surface Tension Measurements

To understand the behavior of a latex solution droplet after it is placed on substrates, we performed contact angle and surface tension tests using a goniometer (DSA100, Krüss GmbH, Germany). We measured contact angle and surface tension according to the drop shape analysis method and the pendant drop method, respectively. We measured quadruplicate samples at room temperature (~22 °C) with a microsyringe steel needle of 1.83 mm outer diameter.

2.3.5. Water Flux Measurements

To evaluate the presence of defects within the latex films deposited onto the porous substrates, we performed water permeation tests using a hydraulic dead-end filtration system (HP4750 Stirred Cell, Sterlitech Corp., USA). All of the polymers we investigated are impermeable to water when they are in the form of continuous macroscopic films.[87-89] Therefore, for a defect-free thin film we expect a permeation flux of zero. If water flux is measurable, this indicates there are defects in the polymer film. Experimentally, the water permeability coefficient, A [μm s^{-1} MPa^{-1}], is the measured liquid flux through a membrane normalized by the pressure applied across a membrane:

$$A = \frac{J_W}{(\Delta P - \Delta \pi)} \qquad \textbf{Equation 2-8}$$

here, J_W [μm s^{-1}] is the osmotic water flux calculated by dividing the volumetric flux by the membrane area, ΔP [MPa] is the applied pressure, and Δπ [MPa] is the osmotic pressure. For a pure water solution, osmotic pressure is zero. Initially, we pressurized the feed of the permeation cell to 1 MPa. If we observed no measurable water flux at this condition, then we increased the pressure to 2 MPa.

2.4. Synthesis of Latex Film on Porous Substrates

We prepared the coating solutions by diluting the latexes to solid concentrations of approximately 6, 12, 24, and 35 wt% using Milli-Q® water (Millipore Corp.). We used dip coating to deposit a thin layer of the polymer latex solutions onto the porous substrates. We used the following general procedure to dip coat the substrates. First, we placed the substrate with the active side (the desired side to be coated) down into a dish

filled with the latex solution; we partially immersed the substrate into the solution such that no polymer solution reached the back side (Figure 2-5.a). Second, after holding the substrate for a specified time (from 2 to 40 sec) within the latex solution (Figure 2-5.b), we removed it and held it vertically (allowing the excess solution to drip from the surface) under one of the different drying conditions (Figure 2-5.c).



Figure 2-5. Procedure of Porous Substrate Dip Coating in the Latex Solution

2.5. Results and Discussion

2.5.1. Measurement of Film Thickness

We studied the effect of the solid content and dipping time on the latex film formation properties. Our initial visual observations during these experiments indicated that the substrates coated with as-received PTFE and PFA solutions (40–60 wt%) had poorly formed films with large cracks. When we dipped substrates in the as-received high solid concentration PVDC latex solutions (51 wt%), the latex solutions did not wet the substrate completely, resulting in a nonuniform coating on the substrate surface. When we diluted all of the latex solutions with deionized water (DI) to concentrations less than 40 wt% solid, we formed dense, even coatings on top of the porous substrates. Based on

these initial observations, we diluted the latex solutions with water to enhance film formation.

Figure 2-6 presents the thickness of the PVDC coatings as a function of dipping time and total solid content of the latex solutions. Our results indicate that a small increase in the solid content of the latex solution yields a change in coating thickness. However, the film thickness is largely independent of the dipping time (from 2 seconds to 40 seconds) at a particular solution solid concentration. Together, these results indicate that dipping times of less than one minute do not significantly impact deposit thickness.

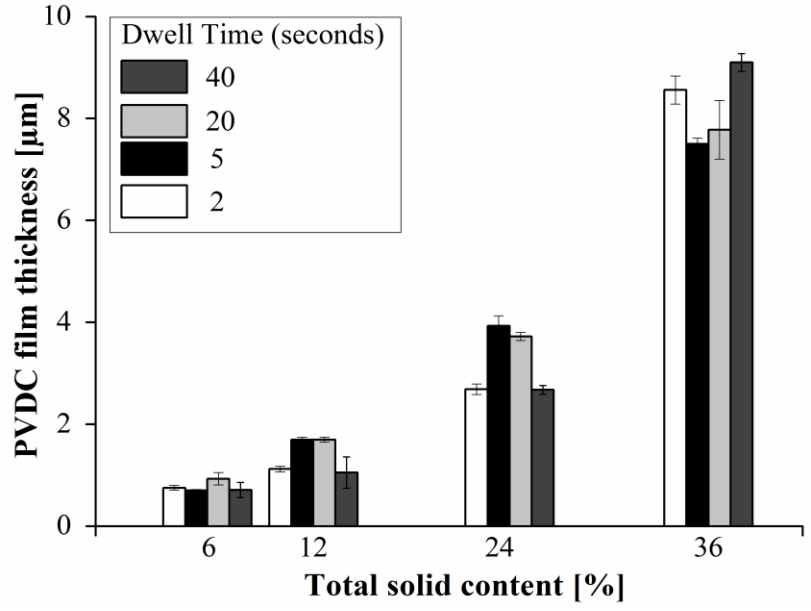


Figure 2-6. Thickness of PVDC Latex Films Cast on Anodisc Supports as a Function of Total Solid Content of Latex Solution and Dip-Coating Time.[90]

We found that Hypod films exhibited a similar trend in behavior to PVDC: by increasing the solid content of the casting solution we obtained thicker films, while dipping times of less than one minute did not significantly change the thickness of the

film at a fixed casting concentration. Additionally, although PTFE and PFA do not deform into a continuous film on porous substrates, they formed an array of particles which exhibited similar behavior (thicker arrays of particles were formed from higher solid concentrations in the casting solution).

2.5.2. Impact of Drying Condition on Latex Film Formation

We cast 600–800 nm thin films of PVDC, PTFE, PFA, and Hypod (from 5–8 wt% latex solutions) onto the Anodisc supports and dried these films according to the methods presented in Table 2. For brevity, Figure 2-7 presents the water permeation results only for the PVDC/Anodisc samples. As described in the experimental section, we consider a defect-free film to be one that has no measurable water flux on the laboratory timescale (and a corresponding permeability of zero).

Table 2-4. Summary of Drying Conditions of Coated Latex Film on Porous Supports[90]

Process	Initial drying time (hours)	Initial drying temperature (°C)	Initial drying relative humidity (%)	Second drying time (hours)	Second drying temperature (°C)	Second drying relative humidity (%)
A	2	65	~ 5	0	-	-
B	24	22	~ 25	0	-	-
C	24	22	~ 95	24	22	~ 25

In process A, the fast drying procedure at high temperature and low humidity, we dried coated substrates for 2 hours at 65 °C and 5% RH. The average water permeation coefficient (10.56 ± 1.93 μm s^{-1} MPa^{-1}) for these samples shows that there are defects large enough for water molecules to pass through. These results indicate that drying latex

solutions at high temperatures gives the latex particles sufficient energy to overcome their mutual repulsion, resulting in films that form before the particles are closed-packed.[55] Some, but not all, of the films prepared by process A were defect-free as indicated by the permeation tests, but as the error bar shows the process is not repeatable. Our SEM images of Hypod film on Anodisc verify the formation of defects in the formed film (Figure 2-8 a, d, g).

In process B, the moderate drying procedure at lower temperature and humidity, we dried the samples for 24 hours at 22 °C and 25% RH. These samples had higher permeation coefficients (average permeation coefficient 35.79 ± 7.68 μm s^{-1} MPa^{-1}) than the films formed by process A, indicating even more defects. However, we supposed that process B show lower defects than process A. The reason for the lower water permeation flux of process A is related to polymer softening at high temperature. We conclude that

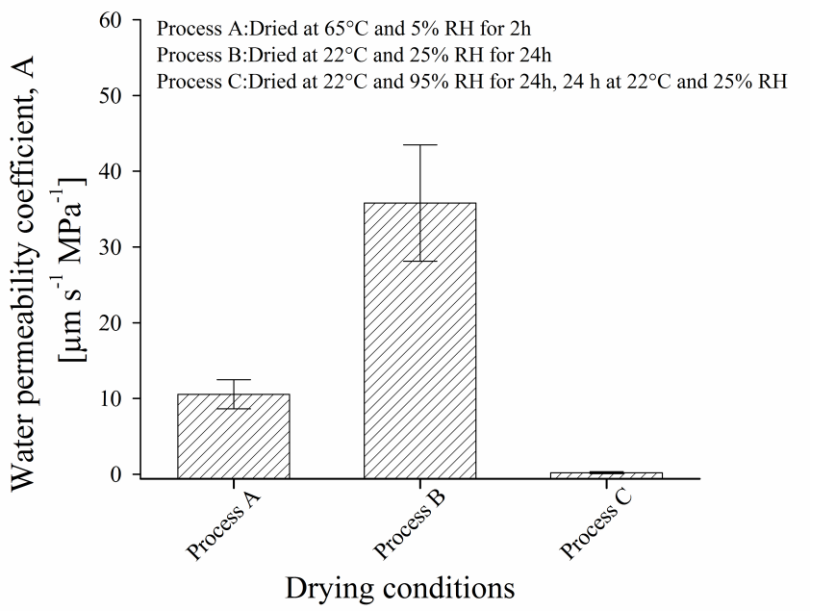


Figure 2-7. Pure Water Permeation through 600–800 nm PVDC Films on Anodisc Supports. Films are Dried at the Conditions Presented in Table 2-4.[90]

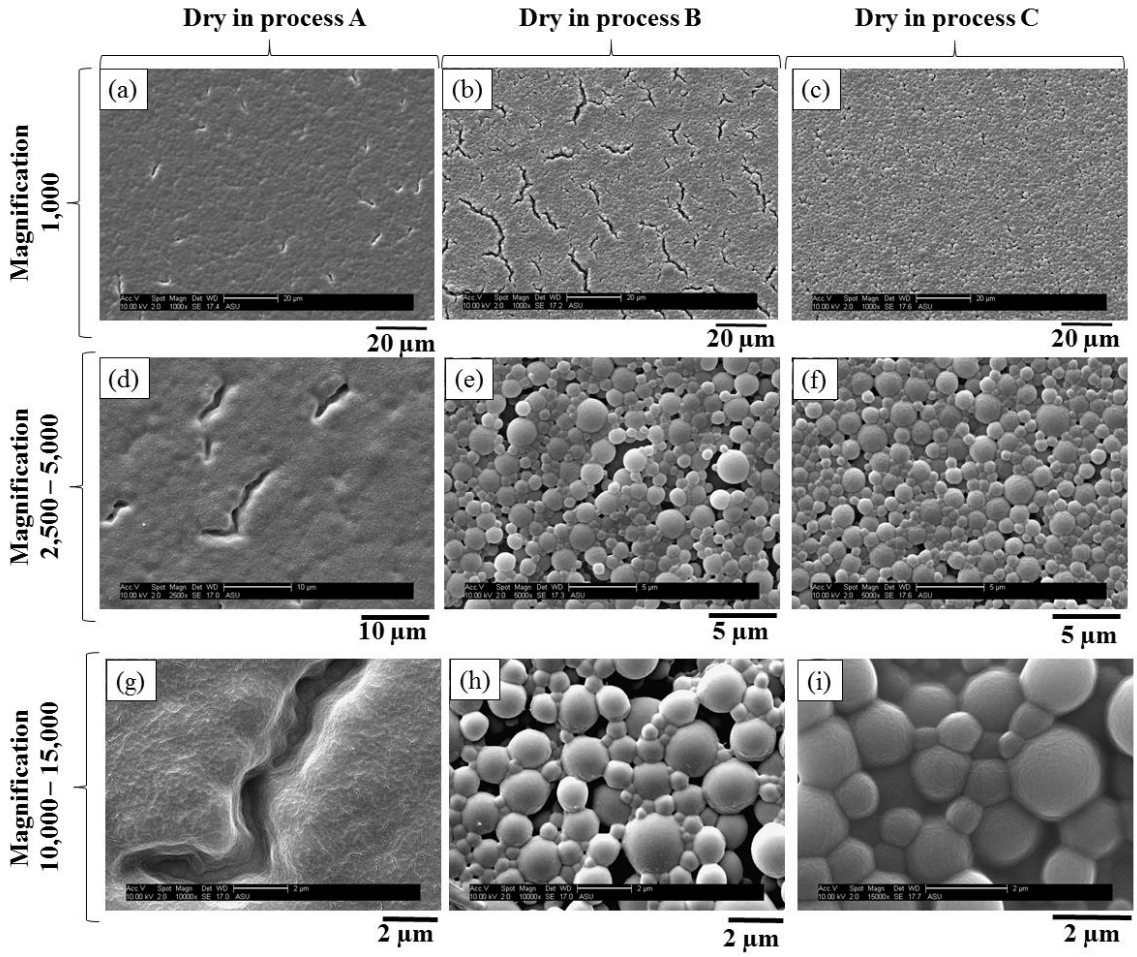


Figure 2-8. SEM Images of 9% Hypod Films on Anodisc Dried in Different Drying Conditions. (a, d, g) Process A: Dried at 65 °C and 5% RH for 2 h. (b, e, h) Process B: Dried at 22 °C and 25% RH for 24 h. (c, f, i) Process C: Dried at 22 °C and 95% RH for 24 h, and for 24 h at 22 °C, and 25% RH.

partial particle softening occurs at the higher drying temperature in process A, which does not occur at the lower temperatures of process B; this softening results in some particles filling the interparticle spaces, and consequently show lower water permeation flux. The SEM images (Figure 2-8 a, d, and g) obviously show the high temperature softening of Hypod particles.

In process C, the slow drying procedure at high humidity, we dried the samples for 24 hours at 22 °C and 95% RH, followed by 24 hours at 22 °C and 25% RH. The samples formed through process C had the lowest permeation coefficients (0.21 ± 0.12 μm s^{-1} MPa^{-1}) of the three drying methods. The combined conditions of lower temperatures, longer times, and high relative humidities reduced the rate of evaporation of water from the latex solution. This slower rate of solvent evaporation may lead to improvement in the quality of films (Figure 2-8 c, f, i), because the particles have more time to come into a close-packed structure prior to coalescence.[60,91,55] Furthermore, the slower evaporation of water gives the particles more exposure time to deforming forces, leading to enhanced deformation and coalescence of soft particles.[56 78,91]

We conclude that samples dried through process C have formed essentially defect-free films, as indicated by no water permeation flux (almost all of the films we made had no permeation, one or two may have had defects resulting in very low permeation). The effect of the drying conditions for Hypod films is similar to PVDC films. However, if the particles are hard (e.g., PTFE and PFA), none of the drying conditions (even the slow evaporation process) we present in Table 2-4 yielded solid films on porous substrates. Though, drying conditions influence on hard latexes deformation on nonporous substrate. For example, SEM images in Figure 2-9 present the fast drying procedure (Process B) caused that water leaves the PFA particles before they come in the close contact, and leads to form an un-continuous film on glass. We show in next section (section 2.05.4) that slow drying of PFA particles (Process A) makes continuous close packed of particles on non-porous substrates.

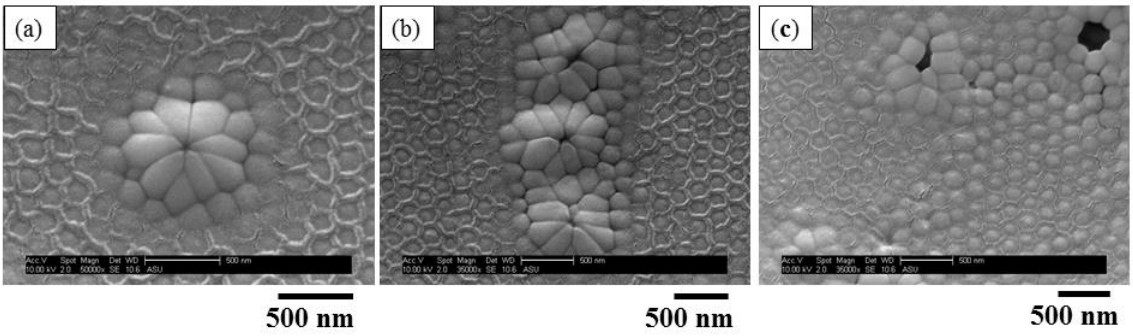


Figure 2-9. PFA Deformed Particles on Nonporous Substrate (Glass) Dried at 22 °C and 25% RH for 24 h

2.5.3. Impact of Substrate Material and Pore Size on Film Formation

After we established that the conditions of process C yielded formation of impermeable thin films of soft latex solutions on porous Anodisc, we studied the effect of the substrate type on film formation properties. We did this by casting PTFE, PFA, PVDC, and Hypod on both nonporous substrates (glass plates) and porous substrates (Anodisc, polysulfone, nylon, PVDF, PTFE, and PES). We dried all cast films according to process C (24 hours at 22 °C, 95% RH, followed by 24 h at 22 °C, 25% RH).

2.5.4. Comparison of Films Cast on Nonporous and Porous Substrates

Figure 2-10 presents SEM images of the surfaces of the latex films cast on nonporous glass substrates and porous Anodisc substrates. The hard particles, PTFE and PFA, deform into a polyhedral structure on nonporous substrates (Figure 2-10 a and b). However, the discernible particle boundaries in Figure 2-10 a and b are evidence that coalescence has not yet occurred. Therefore, the resulting PTFE and PFA films are segmented and are mechanically weak and brittle. Hard PTFE and PFA particles cast on a porous substrate (Figure 2-10 e and f) show no visible deformation. Hypod and PVDC

(Figure 2-10 c, d, g and h) are soft latexes and deform into continuous films on both porous (Anodisc) and nonporous (glass) substrates.

When latex solutions are coated onto nonporous glass substrates, the water leaves the spaces between particles solely by evaporation.[66,74] Particles are concentrated into a closely packed array through evaporation. Further evaporation causes the liquid menisci (which have negative curvature) between closely packed particles to exert compressive capillary forces on the particle network.[71,73,64,65,72] However, when latex solutions are cast onto the porous Anodisc substrate, the water leaves the spaces between particles through two methods: (1) evaporation and (2) wicking into the pores of the substrate. We held all substrates vertically during the initial drying period; therefore, water can evaporate from the backside of the support. Because water is removed by two methods from the porous substrate, the overall rate of water removal from the latex solution is greater on the porous Anodisc substrate than on the nonporous substrate. This increased rate of water removal in porous substrates limits the amount of time the particles have to pack closely, leaving more space between the particles. Consequently, this additional spacing between particles causes less negative curvature of the menisci between the not closely-packed particles.[60] Not only is the capillary pressure from the water trapped between particles lower on a porous support than on a nonporous support, but the exposure time to the capillary pressure decreases significantly for particles coated on porous, hydrophilic substrates due to rapid water removal.

Typically, water has two major roles in latex film formation: (1) it provides a suspending and stabilizing medium for the particles, and (2) it is important in establishing polymer-polymer contact through surface-tension driven capillary forces.[92] However,

when water is rapidly removed from the latex solution, such as on a porous substrate, its typical roles are eliminated.

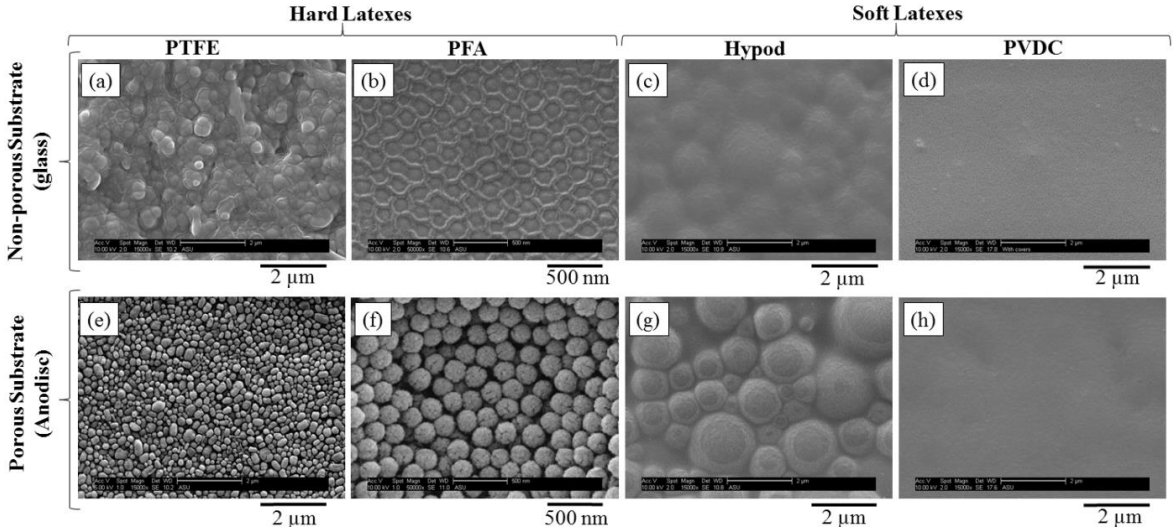


Figure 2-10. SEM Images of (a, e) PTFE, (b, f) PFA, (c, g) Hypod and (d, h) PVDC on Glass, a Nonporous Substrate (top) and Anodisc, a Porous Substrate (bottom), Dried for 24 h at 22 °C, 95% RH and then for 24 h at 22 °C, 25% RH.[90]

Despite the decrease in magnitude of the deforming force as well as the decrease in exposure time to the deforming force on porous substrates, soft latexes make continuous films while hard latexes do not. This difference in film formation ability results from the different shear modulus of the hard and soft polymers. In general, the shear modulus quantifies a material's resistance to deformation; the larger the magnitude of the shear modulus, the more a material resists deformation and flow.[56,76,93,92] The soft particles have a lower shear modulus than the hard particles. For the soft particles, the resistive force of the low shear modulus is less than the reduced capillary pressure on a porous substrate, so the particles deform (Equation 2-7). However, the reduced deforming forces on porous substrates compared to nonporous substrates (because of capillary

pressure reduction) are not strong enough to overcome the large shear modulus of the hard particles and their resultant greater resistance to deformation (than the soft particles).

Polymer viscoelastic relaxation plays an important role in elimination of space between particles.[92] Therefore, it is expected that an increase in the interparticle spacing over which the polymer chain must diffuse would require a simultaneous increase in the time necessary for closure of voids at a specified temperature.[92] Only the DSC scan of PVDC shows the crystallization peak. Therefore, we conclude that some portions of other three polymers (Hypod, PTFE, and PFA) were already in crystalline state. Figure 2-11 presents the XRD patterns of the four polymers we used. Here there are crystalline peaks around 45° for PTFE and PFA. PVDC and Hypod exhibit broad diffuse peaks in their XRD patterns, indicative of their amorphous structure. In general, the increase in crystallinity of a polymer is associated with a decrease in mobility of polymer segments and, consequently, an increase in the rigidity, shear modulus, and hardness of polymer.[94,95] As PTFE and PFA latex particles have a crystalline structure, they have little mobility of polymer segments;[96,97] and as a result the polymer chain diffusion is much slower in these more rigid structures. In separate studies, Lively[60] and Kodani[98] showed that the increase in crystallinity inhibits proper latex film formation by limiting the ability of the particles to deform by limiting polymer-polymer interdiffusion. [98,60]

Overall, film formation of PTFE and PFA on nonporous substrates shows that these hard particles deform on nonporous substrates because of high capillary pressure between the particles. However, coalescence of these hard particles cannot occur on either porous or nonporous substrates because of their viscoelastic properties (high shear

moduli). Our results clearly demonstrate the significant effect of the substrate porosity on the deformation of the latex particles and resultant film formation.

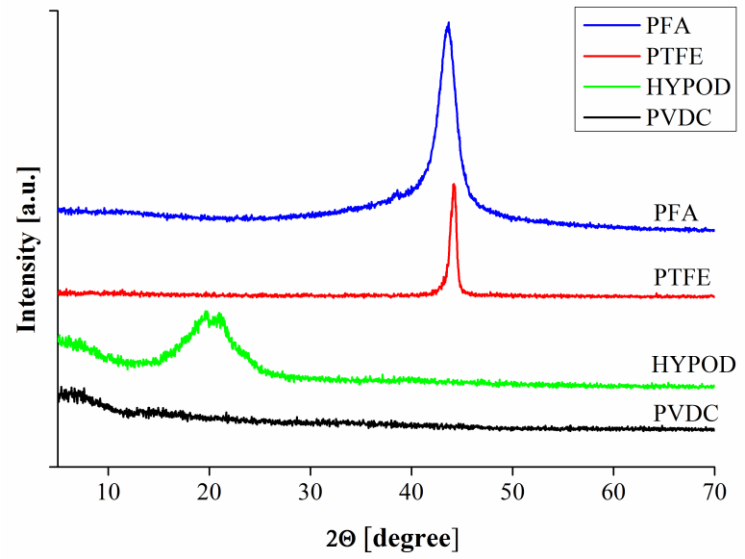


Figure 2-11. XRD Patterns of Latex Films and Arrays

Here, we roughly estimate the degree of crystallinity of these polymers from measurement of the area under the DSC melting peak by using the following equation:[99]

$$Degree\ of\ crystallinity = \frac{\Delta H_m - \Delta H_C}{\Delta H_{m,100\%}} \qquad \textbf{Equation 2-9}$$

where ΔH_m is melting enthalpy (the area under the DSC melting curve), ΔH_C is crystallization enthalpy, $H_{m100\%}$ is melting enthalpy fully crystalline polymer (obtained from the literature). However, there are following limitations for this method:

1- Determination of baseline is arbitrarily chosen when polymers have low crystalline structure as well as when the polymers degrade at low temperature in melting range and show extremely broad melting peak (such as PVDC).[100]

2- The heat of fusion is temperature-dependent. The selection of the temperature is crucial too.[100]

3- When rate of crystallization is slow, the rate of DSC scan will impact the results.

4- There is no comprehensive data base for the melting enthalpy of the fully crystalline polymer. For example, we couldn't find melting enthalpy of the fully crystalline polymer for Hypod (Tetrafluoroethylene-Perfluor(Propyl Vinyl Ether) Copolymer) in the literature, so we are not able to calculate the degree of the crystallinity of Hypod.

Based on this calculation, we found that the polymers had the following enthalpies of melting ΔH_m; PTFE: 71.11 J/g; PFA: 35.01 J/g; PVDC: 14.21 J/g and Hypod: 47.01 J/g. We found that only PVDC had a measurable enthalpy of crystallization of 3.44 J/g.

2.5.5. Combined Role of Pore Size and Hydrophilicity on Latex Film Formation

To investigate the combined effect of pore size and hydrophilicity of porous substrates on latex film formation we measured the contact angles of the latex solutions on the four porous substrates. We successfully cast PVDC and Hypod (from approximately 6 wt% latex solutions) onto the five porous substrates. The porous substrates we used were PSF (pore size: < 10 nm), Anodisc (pore size: 20 nm), nylon (pore size: 100 nm, 200nm), PVDF (pore size: 200 nm), and PES (pore size: 300 nm). We attempted to cast the latex films on hydrophobic porous supports (PTFE); however, the latex solution would not wet the hydrophobic support and we could not successfully

form a film. The results obtained for casting latex solution on PVDF and PES are so similar, therefore for brevity we didn't discuss the PES data separately.

2.5.6.1. Contact Angle and Surface Tension Measurements

In order to form a film, it is important that the latex solution wets the substrate surface. However, for latex film formation on the porous substrates that we used, the role of hydrophobicity/hydrophilicity of the substrate surface is coupled with the role of pore size of the substrate. Much literature[101-106] discusses in detail the effect of roughness and porosity on contact angle and wetting. Here, we simply considered the measured contact angle of the diluted latex solutions on our porous substrates and the surface tension of the solutions; Table 2-5 presents these results.

We found that when the measured contact angle of the latex solution is between 30° and 90°, the diluted latexes easily spread on the porous substrates. However, when the measured contact angle is less than 30°, the diluted latex solutions did not uniformly coat the porous substrate; this is because of rapid wicking of the water into their pores.

On PSF the contact angles of diluted latex solutions of Hypod and PVDC are between 77° and 87°, while pure water has a contact angle of 100°. These solutions readily spread across the surface of the PSF and form a film because the solvent is not rapidly wicked into the PSF substrate. However, on PSF the contact angles of diluted solutions of PTFE and PFA are very low (< 30°); this indicates that the solvent is rapidly adsorbed into the substrate pores and limits time for ordering of these particles. The different behavior of the diluted latex solutions on the PSF substrate is related to the difference in the surface tension of the solutions. As shown in Table 2-5, water has the

highest surface tension among these casting solutions. This implies that the cohesive forces between the molecules in the bulk water are greater than the forces resulting from the interaction between water and the PSF surface.[107] The lower surface tension of the PTFE and PFA solutions indicates that the interaction forces between these liquids and the PSF surface are greater than the cohesive forces between the molecules in the bulk solution.

Table 2-5. Contact Angle of Diluted Latex Solutions (6%) on the Porous Substrates[90]

Latex Solution Type	Surface Tension [mN/m]	Contact Angle [°]					
		Glass	PSF	Anodisc-20	Nylon-100	Nylon-200	PVDF
PTFE	28.15 ± 0.17	<15	26.14 ± 1.01	47.39 ± 0.82	18.33 ± 0.30	<15	<15
PFA	26.37 ± 0.07	<15	<15	57.12 ± 2.43	<15	<15	<15
PVDC	52.30 ± 0.12	<15	86.70 ± 0.47	76.50 ± 1.54	37.10± 1.52	21.125±1.10	30.58 ± 1.48
Hypod	49.72 ± 0.08	<15	78.48 ± 0.57	57.48 ± 2.05	59.54 ±4.39	35.57 ± 3.35	38.86 ± 0.85
Deionized Water	72.48 ± 0.15	<15	100 ± 1.63	<15	<15	<15	<15

All diluted latex solutions have contact angles greater than 47° on the Anodisc substrate. Even though the Anodisc substrates have open pore structures with pore diameters around 20nm, the higher contact angles of the PTFE and PFA latex solutions on the Anodisc compared to other substrates indicate the low surface energy nature of the Anodisc substrate. This low surface energy of the Anodisc substrate compared to the surface tension of the latex solutions results in the wetting, allowing the latex solution to remain in contact with its surface long enough to form an ordered particle array.

On nylon-100, nylon-200, and PVDF substrates, the diluted solutions of PTFE and PFA have contact angles less than 20°, the diluted solutions of PVDC have contact angles less than 40°, and the diluted solutions of Hypod have contact angles less than 60°. The lower contact angles of diluted PTFE, PFA, and PVDC solutions on nylon and PVDF than on the Anodisc and PSF substrates can be attributed either to the high surface energy of these substrates (nylon and PVDF) or to the wicking action of their large pores. If the effect of the surface energy of the substrates were dominant, we would expect the Hypod solutions to have a low contact angle, similar to the other latex solutions. The high observed contact angle of Hypod is evidence that the wicking action in the large pores of these substrates must control the contact angle of the solutions on these substrates. However, the very large particles present in the Hypod solution (up to 3 μm) are significantly larger than the pores of the substrates; these may block the substrate pores and prevent the normally prevalent wicking action. We observe lower contact angles in the other latex solutions as the particle sizes are smaller than those found in the Hypod solution, and may not block the substrate pores as significantly.

2.5.6.2. Effect of Pore Size of Substrate on Latex Film Formation

Figure 2-12 presents SEM images of the surface morphology of the films cast from diluted PVDC and Hypod solutions (6 wt% and 9 wt%, respectively) on substrates with different pore sizes. Figure 2-12 a and e show formation of a smooth, even, defect-free film of PVDC and Hypod on PSF (a polymeric porous substrate with a small pore size). Figure 2-12 b shows that Hypod forms a rough, but defect-free film on an Anodisc substrate (which has a larger pore size than PSF), with less particle deformation than on

PSF. PVDC makes defect free films on both PSF and Anodisc, however, as the SEM images (Figure 2-12 e and f) show, the film formed on PSF is smoother than that formed on Anodisc.

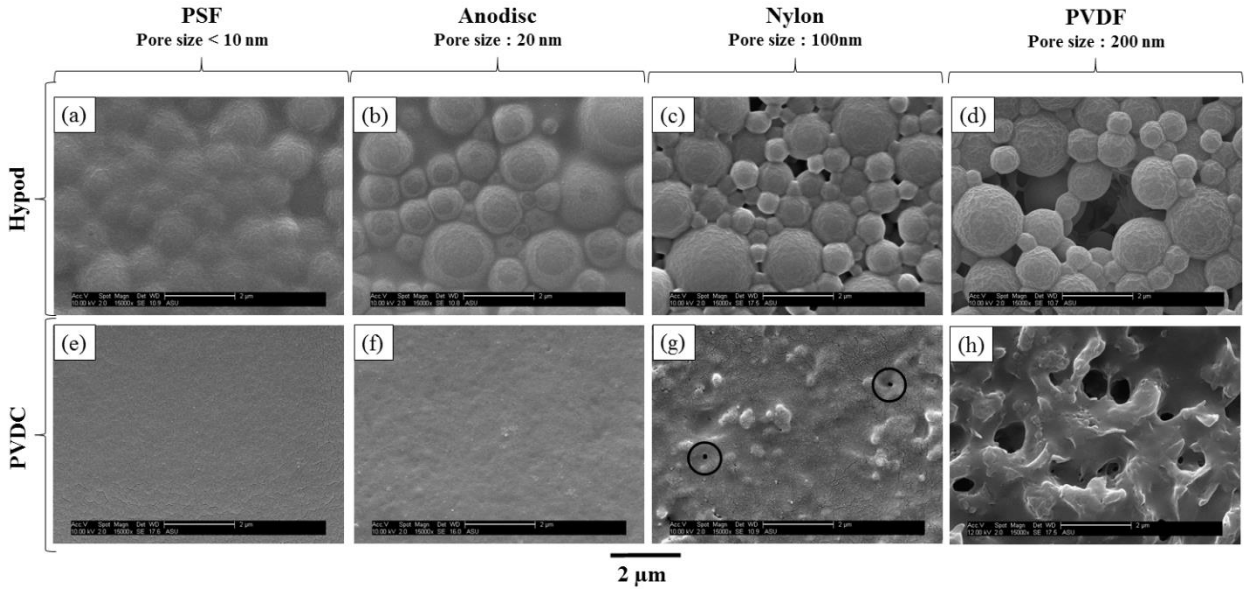


Figure 2-12. SEM Images of Hypod on (a) PSF (Pore Size: <10 nm), (b) Anodisc (Pore Size: 20 nm), (c) Nylon-100 (Pore Size: 100 nm), (d) PVDF (Pore Size: 200nm), PVDC on (e) PSF (Pore Size: <10 nm), (f) Anodisc (Pore Size: 20 nm), (g) nylon-100 (Pore Size: 100 nm), and (h) PVDF (Pore Size: 200nm).[90]

Based on the large interparticle spacing seen in Figure 2-12 c, d, g, and h, we conclude that Hypod and PVDC form discontinuous films on macroporous substrates. This is because the larger pores of the nylon and PVDF supports result in greater wicking by gravitational effects than the smaller pores of the PSF and Anodisc substrates. The water is more quickly removed from the latex solution into the larger pores before the particles are close-packed. This fast wicking of water into the pores of the support limits the particle wetting, increases spaces between particles and reduces the interfacial tension between the water and air. As the pressure differential across the meniscus is inversely

proportional to its radius of curvature,[50] larger spaces between the particles reduce the interfacial forces felt by the particles and result in less particle deformation. A more tightly curved water surface will create a greater capillary pressure.[50] Our results indicate that the extent of water wicking by the porous substrates depends on its pore size. As a larger pore size in the support results in rapid wicking and larger spaces between particles, we conclude that increasing the pore size of the substrate significantly limits latex film formation.

To control for the substrate material, we synthesized latex films on substrates made of the same material with different pore sizes. Specifically, we used nylon-100 (~100 nm pores) and nylon-200 (~200 nm pores). Our SEM and permeation results show that PVDC and Hypod both form defective films on nylon-200 (SEM images depicted in Figure 2-12). These results are comparable to those that we found for PVDF with 200nm pore size. We conclude that the relative pore size diameter of the substrates compared to the average diameters of the polymer particles in the latex solutions is important to latex film formation. Also, water permeation results verify the defective nature of PVDC and Hypod films on macroporous substrates (nylon-100, nylon-200, and PVDF).

Both Hypod and PVDC form continuous films on porous substrates, however the PVDC shows a greater degree of coalescence. As we report in Table 2-3, the Hypod latex dispersion has a broad size distribution of particles - with particles ranging from 100 nm to 3000 nm in diameter. The PVDC latex dispersion has a narrow size distribution of particles centered around 100 nm in diameter.

Figure 2-13 a and b shows the cross section of a thick PVDC film (from 27 wt% latex solution) and Figure 2-13 c and d shows thick Hypod film (from 27 wt% latex

solutions) both on Anodisc supports. Here, the larger diameter Hypod particles (>500 nm) retain their shape while small particles readily deform into a continuous network around the large particles. Small particles of PVDC result in more even coalescence than observed in the Hypod film.

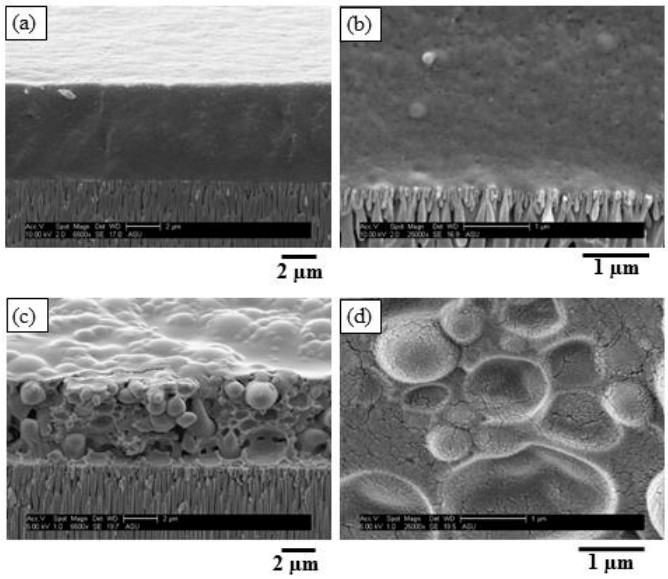


Figure 2-13. SEM Images of a Cross Section of (a,b) 27% PVDC Film on Anodisc and (c,d) 27% Hypod Film on Anodisc.

2.5.6.3. Atomic Force Microscopy Results

Figure 2-14 shows AFM picture of PVDC and Hypod films cast on Anodisc and glass substrates. Figure 2-15 presents the root mean squared (RMS) roughness of Hypod and PVDC films on Anodisc and glass substrates. Our AFM results show that Hypod films have the highest surface roughness on Anodisc (RMS = 369.69 ± 65.91 nm, SAD = 54.67 ± 11.57%) compared to Hypod films on glass (RMS = 136.24 ± 35.11 nm, SAD =

8.273 ± 3.21%), PVDC films on Anodisc (RMS = 28.11 ± 12.06 nm, SAD = 5.00 ± 0.80%), and PVDC films on glass (RMS = 12 ± 8.56, SAD = 3.83 ± 0.78).

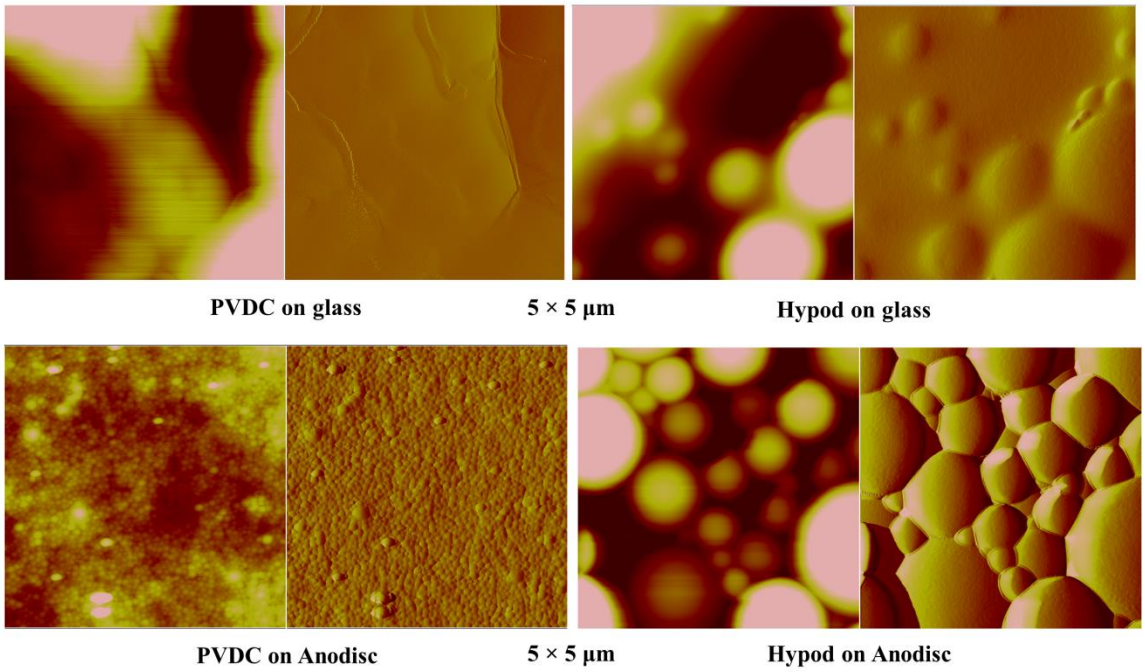


Figure 2-14. Atomic Force Microscopy Images of PVDC and Hypod Films Cast on Anodisc and Glass Substrates

Coalescence refers to the flattening and disappearance of the inter-particle boundaries within the latex films. A decrease in the surface roughness is considered a measurement of the increased extent of coalescence.[108,109] Therefore, the low surface roughness of the PVDC and Hypod films on glass compared to the PVDC and Hypod films on Anodisc indicates a difference in extent of coalescence forces during film formation.

Leonardo[108] believed that viscoelastic properties (affected by polymer average molecular weight and filmification temperature) determine how polymer chains migrate

across particle-particle interfaces.[108] In both cases, forming films on the porous and nonporous substrates, we used the same polymers with the same drying conditions - thus, the particles we used had the same viscoelastic properties. However, in both cases, when comparing Hypod on the Anodisc support to Hypod on the glass support and PVDC on the Anodisc support to PVDC on the glass support, we obtained a rougher (less coalesced surface) on the Anodisc supports. This indicates that the roughness differences we observed are attributable to other effective parameters separate from viscoelastic properties.

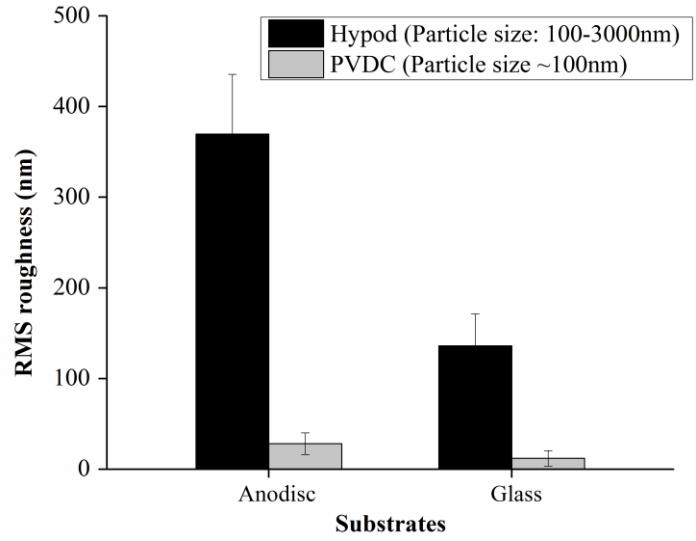


Figure 2-15. Atomic Force Microscopy Results of PVDC and Hypod Films Cast on Anodisc and Glass Substrates.[90]

Brown's theory indicated that the capillary forces depend inversely on latex particle size.[56,76] From Equation 2-6, we see that reducing the particle size causes a greater driving force from capillary forces because of the increased curvature of the solvent surface. Therefore, when the particles are smaller they can pack more closely and

particle flattening occurs more easily.[92] This theory may explain why the smaller PVDC particles form a more homogenous film than the larger Hypod particles.

We hypothesize the roughness difference we observe (for the same type of polymer) on the porous Anodisc versus the nonporous glass substrate is a result of a lower capillary pressure on the porous support. Because the solvent (water) is rapidly wicked into the substrate pores of the Anodisc, the polymer particles do not obtain a close-packed configuration. Therefore, Equation 2-6 does not completely apply – it is necessary to make adjustments for the larger interparticle spaces found in a non-close packed configuration.

2.6. Conclusion

In summary, we have described the synthesis of latex films on porous substrates. Our results show that a latex concentration of less than 10% in the casting solution leads to formation of thin latex films from soft polymers. We found that the latex solid concentration in the casting solution is the most important parameter in determining the ultimate film thickness. For latex film formation two conditions are needed: (1) sufficient exposure time to strong deforming forces and (2) deformable polymers. Although capillary forces are necessary to form a latex film, alone they are not sufficient. To obtain a latex film, the polymer chains of each particle need to diffuse into the surrounding particles, which may occur slowly in comparison to solvent (water) evaporation. We found that decreasing the rate of drying for soft latexes enables film formation even when the solvent (water) is rapidly drawn into the pores of the porous substrate. Consequently, under the appropriate drying conditions, soft particles are deformable into a defect-free

film. However hard latexes only create close-packed structures (that are not defect free) on porous substrates with no polymer chain diffusion. Finally, we found that an increase in the pore size of a porous substrate limits the ability to form defect-free films.

CHEMICAL RESISTANCE OF MEMBRANE

3.1. Introduction

Polyamide (PA) thin film composite (TFC) membrane dominates desalination membrane sales, with more than 90% market share.[37] TFC membranes considerably improved separation performance with their high water flux, high salt retention, and wider operating pH and temperature ranges. However, TFC membranes have low chemical resistance, especially in the case of corrosive feeds such as NASA wastewater which has the low-pH. NASA wastewater is a complex solution (Table 3-1) that contains a number of organic components and four acid-producing components: sodium phosphate, and potassium phosphate, sulfuric acid, and chromium trioxide. Human urine naturally contains sodium phosphate and potassium phosphate.[1,110] However, the sulfuric acid and chromium trioxide are added to the raw wastewater to impede microbial growth and to prevent urea from reacting with ammonia.[1] The stability of membranes in wastewater operations is evidenced by chemical resistance to all components of the wastewater. Materials selection for membrane is complicated due to the low pH and complex composition of the wastewater brine since material should have both chemical resistance to all components and acid stability.[110]

There is a great deal of research[111-115] analyzing commercial RO membranes' chemical resistance. Glater et al.[113] investigated the effect of different halogen disinfection and ozone on the commercial RO membranes.[113] They showed that homogeneous aromatic polyamide is more sensitive to halogen at low pH than at high pH.[113] In another study, Glater et al.[112] studied the structural changes in polyamide type RO membranes in response to exposure to chlorine.[112] They showed that changes in

polyamide membrane structure is resulted from attack of chlorine to amide nitrogen and aromatic rings (Figure 3-1.[112] Aromatic rings bonded to the N-H group have high electron density, therefore, they are sensitive to attack by chlorine radicals.[116] The hyperchlorite (-OCl) induced the attack of chlorine by convert the N - H group to an N - Cl group.[116] Then, the formed N - chloroamide is rearranged to form varied aromatic substitution products and leads to the collapse of the polyamide.[116]

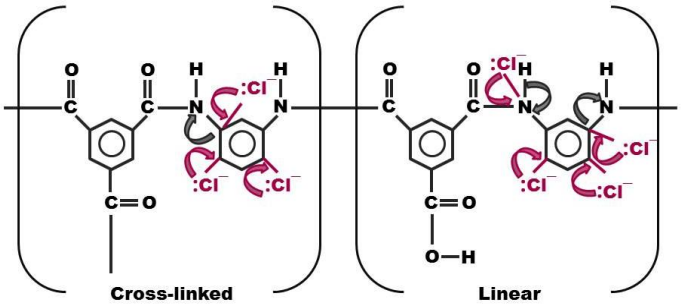


Figure 3-1. Chemical Attack of TFC Membrane by Chlorine (image drawn by Pinar Cay Durgun)

Here, we evaluated the long-term tolerance of PVDC and Hypod to synthetic urine-containing wastewaters. In past research, no pertinent data were found relating to the acid resistance of PVDC and Hypod. We exposed the latex polymer films used in the membrane to a synthetic urine brine solution simulating that produced on the ISS to confirm compatibility and stability for 15 months. We confirmed the highly chemically-resistant nature of PVDC latex thin films through hydraulically-driven water permeation tests, attenuated total reflectance Fourier transform infrared spectroscopy (ATR-FTIR), and X-ray diffraction (XRD).

3.2. Materials

Polyvinylidene chloride (PVDC Diofan® B 204) was purchased from Solvay and a polyolefin-based latex (Hypod™ XU 31683) was donated by Dow chemical. Creatinine, urea, gelatin, sodium chloride (NaCl), sodium sulfite (Na_2SO_3), disodium phosphate (Na_2HPO_4), monopotassium phosphate (Na_2HPO_4), and ammonium chloride (NH_4Cl) were purchased from Sigma Aldrich.

3.3. Methods

3.3.1. Preparation of Ersatz Space Mission Wastewaters

We prepared synthetic wastewater brine based on communications with researchers at NASA.[110] The chemicals are mentioned in Table 3-1 were mixed with Milli-Q® water to make 1 L of solution and continuously stirring them for 2 hours. The pH of prepared solution is 1.94 ± 0.11.

3.3.2. Fabrication of Stand-Free PVDC Film

The PVDC and Hypod films are prepared by the solution casting method. Latex solutions are diluted to a solid concentration of approximately 28%, cast in a Petri dish, and placed in humidity controlled glove bag at 22 °C and 90% RH for 24 h, then at 22 °C and 25% RH for 24 h. We made a defect-free film of PVDC and Hypod with thickness of 150–200 µm. We characterized PVDC/ Hypod films before soaking in synthetic brine. After 15 soaking in synthetic brine, we washed films five times with Milli-Q® water, dried them at room temperature, and then characterized them.

Table 3-1. Composition of Ersatz Space Mission Wastewaters Used to Initially Test the Corrosion Resistance of Polymer Latex, Table Reproduced From Jamieson.[110]

Component	Amount (g)
Ammonium chloride	3.00
Calcium chloride	0.66
Chromium trioxide	2.00
Gelatin	1.00
Nutrient broth	0.16
Potassium phosphate	2.50
Sodium chloride	9.00
Sodium phosphate	2.50
Sodium sulfate	3.06
Sodium sulfite	3.00
Sulfuric acid	7.50
Urea	25.00
Water	To reach 1 L total volume

3.4. Characterization

Attenuated total reflectance Fourier transform infrared spectroscopy (ATR-FTIR, Nicolet 6700, Thermo Electron Company, USA) was used to elucidate the any change in chemical composition and the bonding arrangement of PVDC and Hypod through exposure to synthetic brine. Fourier transform infrared spectrometer (FTIR) was done in the range of 500–4000 cm^{-1}.

We used X-ray diffraction (X'pert Pro, PANalytical, USA) to evaluate any change in the crystalline structure of PVDC and Hypod after exposure to brine. X-ray diffraction

patterns were recorded by monitoring the diffraction angle 2θ from 5° to 60° under a voltage of 40 kV and a current of 40 mA.

Before and after film exposure to synthetic brine, we performed water permeation tests using a hydraulic dead-end filtration system (HP4750 Stirred Cell, Sterlitech Corp., USA). Before exposure, PVDC and Hypod showed that they are inherently impermeable to water. After exposure, if these polymers have a good chemical resistance to synthetic brine, we expect a permeation flux of zero. If water flux is measurable, this indicates that the synthetic brine destroyed the polymer films.

3.5. Result and Discussion

3.5.1. ATR-FTIR Results of PVDC

FTIR is an effective tool for studying the composition and monitor change in molecular bonds.[117] The main bands of PVDC structure include C-Cl stretch vibration in 850-550[118] Cm^{-1} (655 Cm^{-1}), the C–H wag of the -CH_2Cl group (alkyl halides) in 1300-1150 Cm^{-1}, C-H bending in 1480-1350 Cm^{-1} (the presence of the 1404 Cm^{-1} band indicating the block copolymerization of the used PVDC)[119], and C=O stretch in 1820-1670 Cm^{-1} (the carbonyl peak caused by the presence of plasticizer, end group modification, or the presence of comonomer)[119,120] (Table 3-2). The main bands are preserved after 15 months' exposure to brine; however, there are very few differences in the FTIR spectra obtained for PVDC films after exposure. For comprehensive investigation, special focus is made on the region of 600-1800 cm^{-1}. The differences are a light decrease in absorbance at 655 cm^{-1}, a shift to higher wavenumbers at peaks 1200-1100 Cm^{-1} region

(1137 Cm^{-1}), and an increase in absorbance of peak at 1820-1670 Cm^{-1} region (Figure 3-2).

The decrease in absorbance at 655 cm^{-1} is attributed to C-Cl stretch vibration. This change can be ascribed by the change in the molecular chain orientation or lower concentration due to sample thickness and smaller path length. The strength of an absorption band depends on the dipole moment of the bond and the number of specific

Table 3-2. Absorption Frequencies of Characteristic Vibrations of PVDC

Wavenumber (Cm^{-1})	Bond	Type of bond
850-550	C-Cl stretch	Alkyl halide
1100-1000	C-OH stretch	Primary alcohol
1300-1150	C-H (of CH_2Cl) bending	Alkyl halide
1480-1350	C-H bending	Alkane

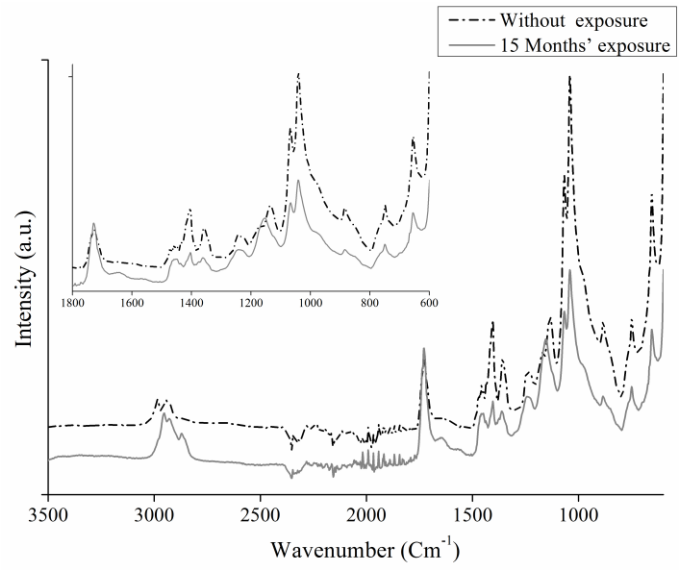


Figure 3-2. FTIR Spectra of PVDC Film Before and After Exposure to Synthetic Brine

bonds present. Because film thickness is much greater than depth of penetration, this change in strength cannot be attributed to film thickness alone. Accordingly, a decrease or increase in the strength of the C-Cl absorption peak implies a change in the molecular chain orientation of thin film.[121]

The gradual shift of the CH (1200-1100 Cm^{-1} region) to lower frequency (higher wavenumber) may have been caused by the lower energy required for CH bond bending. Lower energy requirements is caused by shortening the C-H bond, which results from decreasing hydrogen bonding between hydrogen of CH and Y (Y is an acceptor atom).[122,123] Additionally, the position of the peak for the C-H group and C-H … Y bond distance was observed, where a lower frequency for the peak correlated with a shorter hydrogen-bond distance, i.e., a stronger hydrogen bond and a longer C-H bond.[122]

The increase in intensity of the peak at 1760 Cm^{-1} of exposed films shows a change in the molecular chain orientation of the carbonyl group.

3.5.2. ATR-FTIR results of Hypod

Hypod is the aqueous solution of ethene-1-octene copolymer and ethylene acrylic acid copolymer. The chemical structure of these copolymers is drawn in Figure 3-3. The peaks at 1440-1395 Cm^{-1} and 3300-2500 Cm^{-1} is attributed to the bending and stretching of the - OH group, respectively. The large peaks at 295-2850 and 1480-1350 Cm^{-1} correlate to the stretching and bending of the - CH group, respectively. The peak at 1760-1690 Cm^{-1} results from the presence of functional carbonyl group of the carboxylic acid group. On close observation of the 600-1800 Cm^{-1} region, three

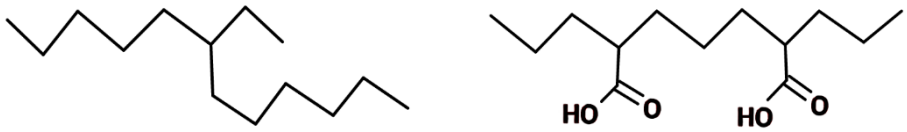


Figure 3-3. Chemical Structure of Hypod (Ethene-1-Octene Copolymer (Left) and Ethylene Acrylic Acid Copolymer (Right))

Table 3-3. Absorption Frequencies of Characteristic Vibrations of Hypod

Wavenumber (Cm^{-1})	Bond	Type of bond
1440-1395	O-H bending	Carboxyl acid
1480-1350	C-H bending	Alkyl
1760-1690	C=O stretch	Carboxyl acid
2950-2850	C-H stretch	Alkyl
3300-2500	O-H stretch	Carboxyl acid

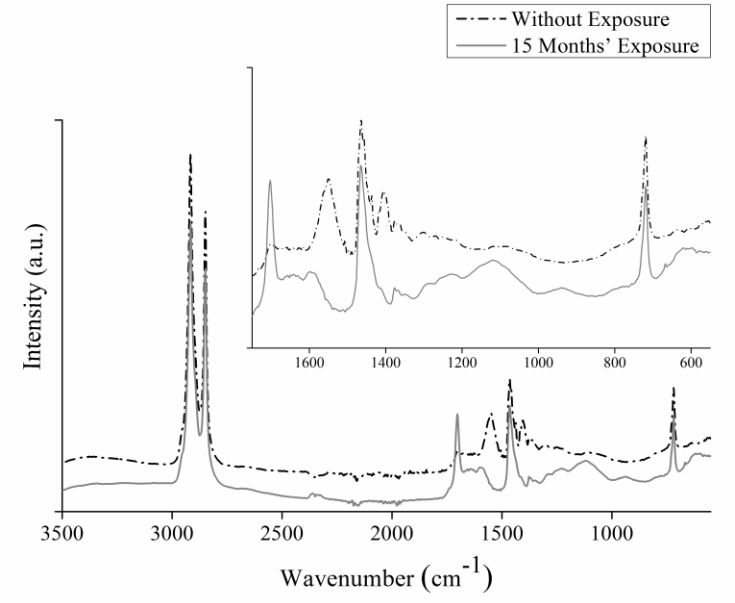


Figure 3-4. FTIR Spectra of Hypod Film Before and After Exposure to Synthetic Brine

discernable changes were seen in Hypod FTIR after 15 months' exposure. First, the peculiarity in the FTIR absorption spectra of Hypod film after 15 months' exposure to synthetic brine is the vanishing of the two peaks at 1405 and 1550 cm^{-1}. Another, significant growth of the C=O peak at 1702 cm^{-1} can be attributed to the formation carbonyl group. The absence of fundamental vibration of –CH and formation new carbonyl groups confirms chemical degradation of Hypod.

3.5.3. XRD Results

To further evaluation the extent of brine effects on polymers, X-ray diffraction study was carried out on the PVDC and Hypod films. Figure 3-5 and Figure 3-6 show the diffraction pattern acquired from the polymer films before and after exposure to brine. Both PVDC and Hypod polymer films show no sharp XRD features since they are amorphous and semicrystalline in their natures, respectively. Although the PVDC

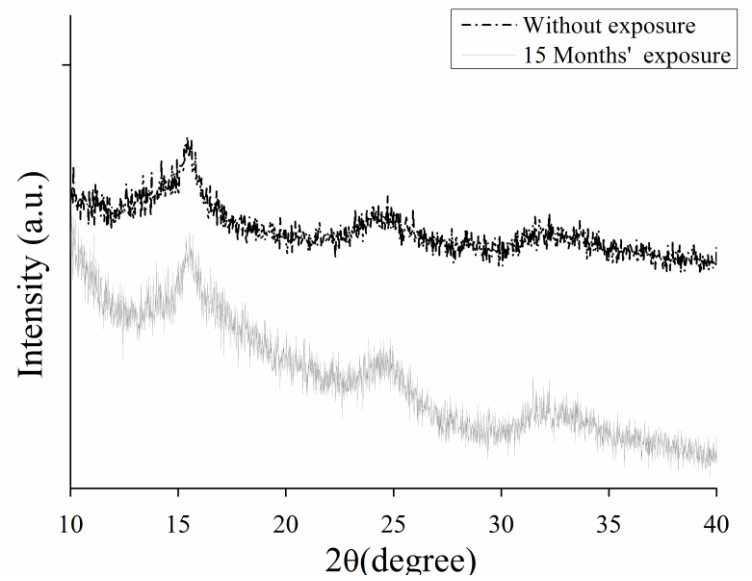


Figure 3-5. XRD Spectra of PVDC Film Before and After Exposure to Synthetic Brine

does not have any sharp crystalline peak (Figure 3-5) to inspect, its amorphous peaks centered at 15º, 24º and 32º are in the same locations on before and after exposure diffractograms. We conclude synthetic brine does not have any effect on the crystal structure of this polymer.

In the case of Hypod, the diffraction pattern of this polymer shows its semicrystalline structure, with the most intense peaks at 19º and 21º (Figure 3-6). The sequence of XRD patterns shows that brine does not affect crystalline structure of Hypod, because the shape of the reflections does not change significantly.

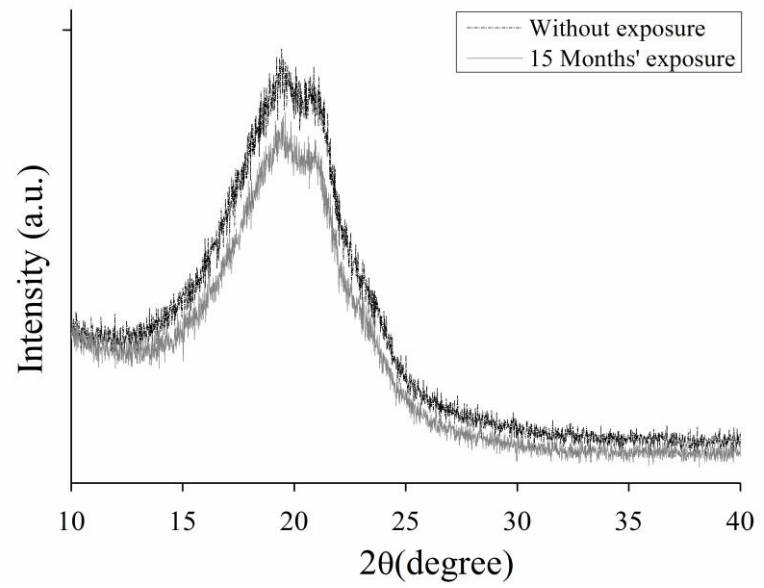


Figure 3-6. XRD Spectra of Hypod Film Before and After Exposure to Synthetic Brine

3.5.4. Water Permeation Results

We performed permeation tests of prepared film before and after exposure to synthetic brine. The average water permeation coefficient of zero for PVDC and Hypod films before exposure shows that they are defect-free films. The zero flux permeation

results of PVDC after 15 months' exposure show PVDC's high chemical resistance to synthetic brine and raw urine. Permeation results of Hypod show that although this polymer is inherently impermeable to water, after 15 months' exposure to synthetic brine, Hypod film absorbs water and swells. This swollen film will be found defective after exposure to water at high pressure. The Hypod results show that this polymer does not have sufficient chemical resistance to synthetic brine.

MOLECULAR SIEVES SYNTHESIS

4.1. Introduction

Zeolites, with the unique crystal aluminosilicate structure, have received considerable attention because of their unique frame structure, high thermal stability, and chemical stability. These unique characteristics have expanded the application of zeolite from household products to industries, e.g., aquaculture, agriculture, water treatment, detergents, separation adsorbents, catalysts, and ion exchange materials.[124,125] The narrow pore size of zeolite makes it a highly selective membrane in gas separation and the most technologically important of the molecular sieves.[126] There are more than 40 types of natural zeolites, and there are more than 150 types of manufactured zeolite.[127] Within this range, we considered pore size of zeolites in order to select zeolite for our mixed matrix membrane. The main goal of this research is wastewater treatment; therefore, in selecting pore size, we consider the molecular size of water (3Å)[128] and the smallest contaminating molecule of feed, such as urea (5 Å)[129].Therefore, we selected types of zeolite, which have a pore size greater than 3 Å and smaller than 5 Å, such as KFI, LTA, MEL, MFI, PAU, SOF, SVR, and TSC. Among the zeolites, zeolite LTA is of exclusive interest in water treatment because of its high hydrophilicity and the small size of its pore diameters (4 Å) (Figure 4-1). The second option is MFI zeolite (silicalite-1, ZSM-5) with a pore size of 4.5 - 6 (Figure 4-1). The lower alumina percentage of MFI zeolite provides higher stability in low pH conditions.[110]

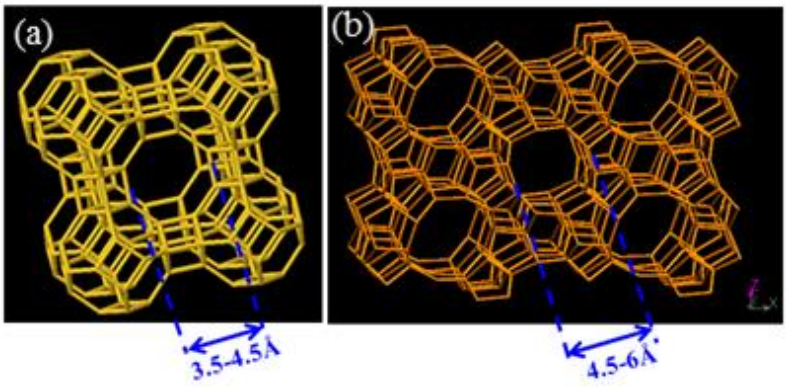


Figure 4-1. Zeolite Structure and Pore Size; (a) Zeolite LTA, (b) Zeolite MFI (Reproduced from Ref.[130])

Decreasing the size of zeolite particles results in an increase in their surface-to-volume ratio; consequently, the external surface area available for interaction in different reactions rises significantly.[131] Plenty of synthetic strategies and methods have been developed to make nanosized zeolite particles, including laser radiation,[132] microemulsion techniques,[131] confined space synthesis,[133] and using templates (structure-directing agents).[134] The common way to decrease zeolite particle size is with organic templates.[135] However, templates are expensive, environmentally-unfriendly organic chemicals. Additionally, the calcination process often used to remove the template from zeolite pores leads to irreversible aggregation of the particles and changes in the Si/Al ratio.[136-139,135] Therefore, template-free synthesis of uniform nanosized zeolites is a challenging and highly desirable research area.

One method to alter zeolite crystal size is controlling the ratio of the nucleation rate to the growth rate by manipulating the degree of supersaturation of the synthesis solution. Supersaturation of a zeolite precursor solution can be controlled by both changes in the composition factors (alkalinity, additives, concentration of the template)

and by change in conditions of crystallization (reaction temperature and time, stirring, seeding and gel aging,[140] and elapsed time between mixing reagents and elevating the temperature to crystallization temperatures).[141] To control the synthesis of zeolite, one must understand the fundamentals of nucleation, the initial stages of solid-state formation from liquid solution.[142-144]

4.1.1. Principle of Crystallization

Nucleation and growth occur if supersaturation, the difference between the actual and equilibrium concentration of solute at a specific temperature, exists.[145] From chemical and thermodynamic points of view, supersaturation is the driving force for crystallization.[146] Depending on the degree of supersaturation, the chance of nucleation and growth are different. Figure 4-2 shows the solubility curve's regions; at the stable zone, the solution is unsaturated. By decreasing the temperature (below the phase transformation point), increasing the concentration of solute (more than its equilibrium), or evaporating the solvent, supersaturation occurs.[147] The supersaturation region can be divided into three distinct regions:

- **Metastable zone:** There is limited chance for new nuclei to be created; previously existing nuclei can kinetically develop into crystals in metastable zones. [148,149]
- **Nucleation zone (**or liable zone**):** This is a region with sufficient supersaturation for nucleation and growth, which can occur simultaneously.[148,149] The time for any given driving force required for the first nuclei to form is called induction time, and is defined as a period of time which elapses between the achievement of supersaturation and the appearance of crystals.[148-150]

- **Precipitation zone:** Excess solute spontaneously precipitates because of a very high level of supersaturation.[151]

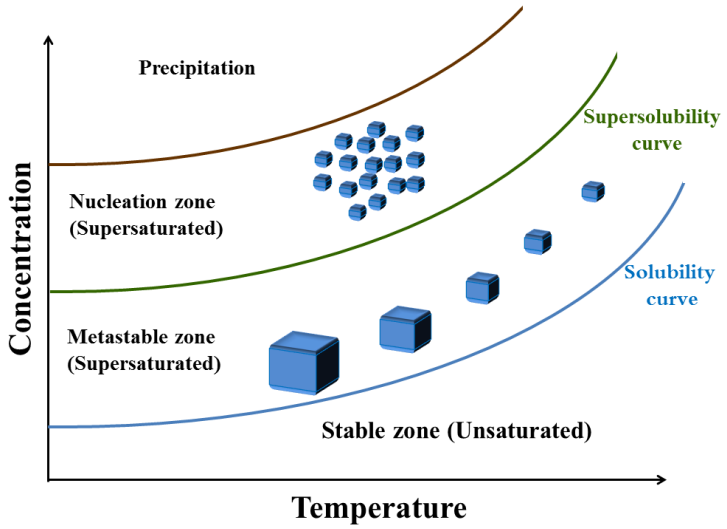


Figure 4-2. Solubility and Supersolubility Curve (Redrawn from Ref.[152])

In supersaturated solution, there is a competition between nucleation and crystal growth to determine ultimate zeolite crystal size. Higher nucleation rate leads to smaller particles.[137] Increased solute, decreased temperature, and/or evaporated solvent increase supersaturation and eventually increase nucleation rate. It is worth mentioning that a decrease in temperature decreases the growth rate as well.[153,137,154]

Based on classical nucleation theory, a supersaturated solution tends to decrease its high free energy via segregate excess solute out of the solution,[155] and form a new phase. The total free energy(Gibbs free energy)[156] (Figure 4-3, blue curve) is a sum of two terms; bulk free energy (Figure 4-3, green curve) and interfacial energy (Figure 4-3, red curve).

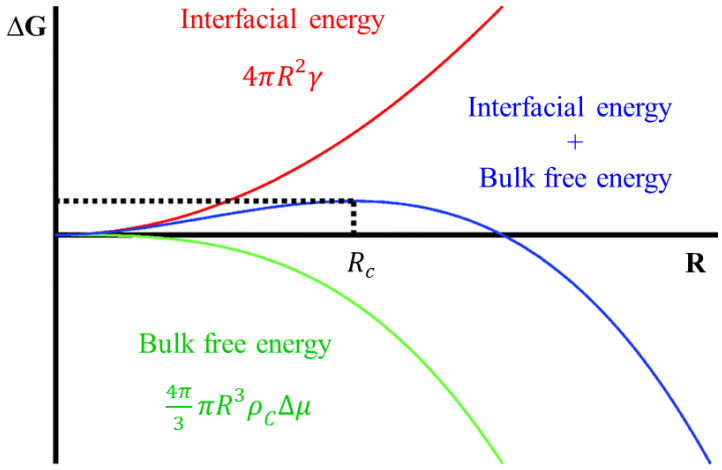


Figure 4-3. Thermodynamic Effects of Formation of a Second Phase Based on Classical Nucleation Theory: Increase in Interfacial Energy and Decrease in Bulk Free Energy. Image Reproduced From Gebauer[157]

The creation of a new phase (solid germ) reduces the bulk free energy (volume energy) since the free energy of the solid is much less than that of the liquid. However, the formation of solid germ increases interfacial energy (surface free energy)[143] In brief, the solid germ formation causes reduction of volume free energy and increases in the surface energy.[143] Based on classical nucleation theory, the change in total free energy (ΔG) due to formation of the solid germ equals to:

$$\Delta G = -V_S\left(G_V^L - G_V^S\right) + \left(A^{SL}\gamma^{SL}\right) \qquad \textbf{Equation 4-1}$$

$$\Delta G = \frac{4\pi}{3}\pi R^3\rho_C\Delta\mu + 4\pi R^2\gamma \qquad \textbf{Equation 4-2}$$

where V_S [m^3] is the volume of the solid sphere, A^{SL} [m^2] represents the solid/liquid interfacial area, γ^{SL} [J/m^2] is surface tension, and $(G_V^L - G_V^S)$ [J/m^3] signifies the difference between free energies per unit volume of solid and liquid. Since at a temperature less than melting temperature (T_m) G_V^S is less than G_V^L, the left term of

Equation 4-1 is negative when temperature is less than T_m, while the right term is always positive. At the point that the total free energy goes through a maximum, the critical nucleus radius obtain:

$$\frac{dG}{dr} = 0 \quad \rightarrow \quad R_c = -\frac{2\gamma}{\Delta G}$$ **Equation 4-3**

After a solid germ forms, there is a competition between minimizing energy and maximizing entropy. If size of the formed solid germ is less than critical nucleus radius, interfacial term dominates and increases overall free energy of the system, so the solid germ is not stable and will be dissolved. However, if the formed solid germ is larger than critical nucleus radius, bulk term dominates and decreases overall free energy of the system, so the solid germ converts to a stable nucleus.

4.1.2. Effect of Aging on Crystallization

Aging is a process of holding zeolite precursor gels at temperatures lower than their hydrothermal reaction temperature prior to synthesis. Aging of the precursor gel is a known method to make smaller zeolites with a narrow size distribution.[158-160,142,161] Previous research showed that aging of the precursor gel decreases particle size,[158,162] shortens induction period,[163,149] and increases the crystallization rate.[158,159,164]

The mechanism of the gel aging processes that leads to changes in particle size is not entirely understood.[141] The aging has effect on the initial stages of solid-state formation from liquid solution.[165] To understand the mechanism of aging, first we discuss steps of condensation phase transition processes; nucleation, growth, and Ostwald ripening.[166]

The first step of phase transition occurs as a result of two mechanisms: (1) nucleation, in which cluster formation starts from a metastable initial state, and (2) spinodal decomposition (or "barrierless phase transition")[167], in which cluster formation starts from an entirely unstable initial state.[168,169] Binary mixtures that have a negative curvature of the free energy versus composition curve undergo spinodal decomposition if they are quenched to a thermodynamically unstable state.[170] From a mathematical point of view, the theories of spinodal decomposition and nucleation are very different. However, from a physical point of view, phase separation is the same for nucleation (with a small thermodynamic barrier to form a new phase) and for spinodal decomposition (with no thermodynamic barrier to phase separation).[171] The phase separation rate is influenced by both the diffusion coefficient and the rate of temperature change.[172] Vekilov studied the dependencies of the nucleation rate of the protein lysozyme on temperature. He observed that upon cooling, the nucleation rate has a sharp maximum because of the transition from nucleation to spinodal decomposition.[173] Ruberti et al.[172] invented a method to control physical properties of vinyl polymer hydrogels without chemical cross-links or radiation.[174,175] They modulated the crystallization process by controlling the temperature. They demonstrated that during the freezing process, the system undergoes a phase separation through followed by crystallization, which leads to significant improvement in the mechanical properties of the polyvinyl alcohol (PVA).[174,175]

Ostwald ripening is a phenomenon appearing in the last stage of phase transitions.[176,177] Ostwald ripening is a thermodynamically driven, spontaneous process[178] to minimize the overall system energy.[179] Larger particles (which are more energetically

stable than smaller particles) grow at the expense of dissolution of smaller unstable particles, which have higher solubility as predicted from the Gibbs-Thomson equation.[180] Madras and McCoy showed that Ostwald ripening increases with decreasing temperature because of the effect of temperature on interfacial free energy, equilibrium solubility, and growth rate coefficients.[181] Madras presented how to assess the rate of denucleation according to the appropriate cluster dynamics equations.[176]

Independently, Alfaro et al.[155] and Bronic et al.[156] both demonstrated that zeolite LTA particles synthesized from precursor gels aged at 22 ºC yielded finer and more monodispersed crystals compared with zeolite LTA particles synthesized from unaged precursor gels.[158,159] They hypothesized that aging the precursor gel at room temperature increases the number of nuclei because the unaged gel and aged gel displayed the same linear rate of crystallization, while aged gels crystallized for a significantly shorter time compared to the unaged gel.[158-160] Although studies on zeolite LTA[158,159,164] showed aging has no effect on the rate of linear crystal growth, Twomey et al.[179] and Li et al.[140] independently demonstrated that prolonging aging time strongly increases growth rate of the silicalite-1 particles.[141,182] Katovic et al.[183] studied the effect of aging in co-crystallization of zeolites P and X.[183] They showed an increase in the aging time of the gel decreases the induction periods of both zeolites P and X. Furthermore, prolonging the aging time increases the yield of zeolite X; this is ascribed to the changes in the chemistry and structure of the solid and liquid phases as well as the kinetics of crystallization during gel aging.[183]

Koroglu et al.[136] and Zhdanov et al.[161] reported formation of smaller zeolite Y particles and shortening hydrothermal crystallization times when the zeolite Y precursor

gel was aged at a temperature below room temperature.[137,164] The Koroglu team[136] showed zeolite Y particles aged at 22 ºC are larger than those aged at 4 ˚C. However, Feoktistova et al.[160] reported different behaviour for zeolite LTA from that observed in Zeolite Y.[160] They showed that decreasing the aging temperature from room temperature to 7 ˚C leads to the increase in zeolite LTA particle size; however, they did not hypothesize an explanation for this behaviour.[160]

To the best of our knowledge, no previous studies have investigated the aging temperature range of 7 ºC to -20 ºC on any zeolite gels. In this work, we investigated the effect of different aging temperatures (from -20 to 40 ºC) and aging times on zeolite LTA crystal size and composition. Furthermore, the spinodal decomposition phenomenon has been widely investigated in various systems, including metallic alloys,[184,185] polymers,[186-189] colloids,[190] proteins[173], and liquid mixtures.[168] However, to the extent of our knowledge, there are no studies on spinodal decomposition in zeolite precursor gels. We use the concepts of Ostwald ripening and spinodal decomposition phenomena in the zeolite precursor to describe our results.

4.2. Materials

Sodium silicate, sodium hydroxide and anhydrous sodium aluminate were purchased from Sigma-Aldrich.

4.3. Synthesis Procedure

Initial hydrogels were prepared by adding a clear silicate solution into clear aluminate solution (Figure 4-4, c). The molar composition of the zeolite LTA

precursor gel is 1.6 Na_2O: SiO_2: 0.505Al_2O_3: 150H_2O.[191] Sodium silicate solution was prepared by adding 2.452 g of sodium silicate and 1.033 gr of sodium hydroxide in 45.895 g demineralized water (Figure 4-4, a). Sodium aluminate solution was prepared by dissolution of 1.225 g of anhydrous sodium aluminate in 50 g demineralized water (Figure 4-4, b). Each solution was stirred for 1 h; then the silicate solution was quickly poured into the aluminate solution and homogenized using a magnetic bar stirrer (vigorously) for an additional 1 h. The amorphous precursor gel was left to age for a certain period of time (0 hours, 7 days, 14 days, 21 days) at various temperatures (-20, -8, 0, 4, 8, 22, 40 ˚C) (Figure 4-4, d). To crystallize the precursor gels, we transferred them into a Teflon-lined stainless steel reactor (CIT-HTC230, COL-INT Tech) (and placed them in a preheated convection oven at 100 ºC for 72 hours (Figure 4-4, e). After the crystallization was complete, we washed the particles (centrifugation and decanting of supernatant) with deionized water until the pH value of the supernatant was less than 9. Finally, we dried the washed particles overnight at 80 ˚C.

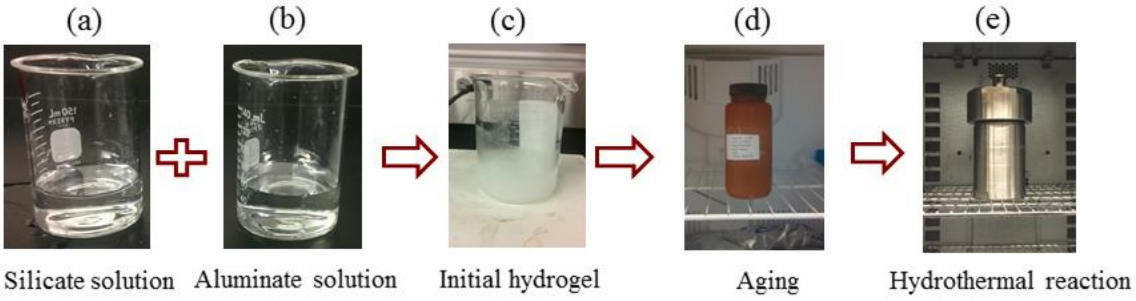


Figure 4-4. Procedure of Zeolite LTA Synthesis Including Precursor Preparation, Aging, and Hydrothermal Reaction

4.4. Characterization

We determined the average particle size and solid morphology using scanning electron microscopy (SEM, FEI/Philips XL-30 Field Emission ESEM-FEG). We used X-ray diffraction (XRD, X'Pert Pro, PANalytical) to identify the synthesized zeolite products. X-ray diffraction patterns were recorded by monitoring the diffraction angle 2θ from 5º to 40º under a voltage of 40 kV and a current of 40 mA. We utilized PANalytical X'Pert HighScore Plus, v3.0 (v2.2c) to index the XRD patterns. We proved formation of nuclei in aged precursor gels using transmission electron microscopy (TEM, FEI Titan 80-30). To prepare the TEM samples, we dispersed two drops of the precursor gel in 1 mL of ethanol with sonication for 10 minutes, then we placed one drop of the resulting suspensions onto a copper grid. Finally, we dried it at room temperature. We performed Raman characterization using a Renishaw inVia Raman microscope at a wavelength of 488 nm with power output of approximately 15 mW. Raman spectra of solid parts of the aged precursor gels identified any changes in Si/Al ratios. The aged precursor gels were centrifuged to separate the liquid phase and solid phase. The separated solid phase was washed once with deionized water, and a drop was put on the microscope slide and dried for two hours at room temperature prior to Raman analysis. We measured the freezing temperature of the gel by monitoring the solution as we cooled it from room temperature in a bath of methanol and dry ice.

4.5. Results and Discussion

4.5.1. Effect of Reaction Temperature on Zeolite LTA Crystal Size

The zeolite produced at 100 ºC for 72 h displays cubic-shaped crystals with planar surfaces, well-defined edges, and sharp crystals. Our results show that decreasing reaction temperature from 120 ºC to 60 ºC led to significant reduction of zeolite LTA crystal size **(**Figure 4-5**)**, but the fraction of crystalized products significantly decreases.

The reason for formation of smaller particle size by a decrease in temperature reaction is that by decreasing temperature, solubility generally decreases. Therefore, crystallization occurs at high supersaturation, and, domination of crystal nucleation over crystal growth, and formation of smaller particles.

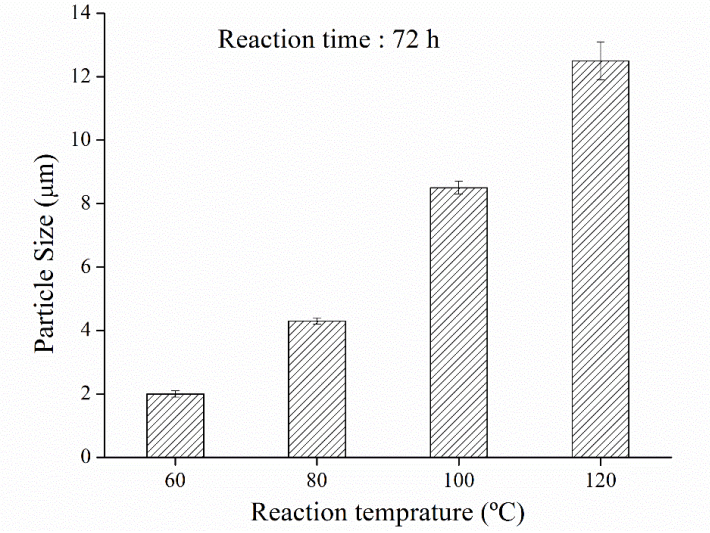


Figure 4-5. Effect of Reaction Temperature on Zeolite Particle Size

The error bar of Figure 4-5 shows that the higher temperature leads to the formation of a broad range of particles. When nucleation is fast (lower reaction temperature), many crystals form in the same time. Through their growth, the medium of

solute decreases significantly and may cease nucleation; therefore, the monodisperse particles form.[144] In contrast, slow nucleation (higher reaction temperature) leads to slow depletion of supersaturation, so the nucleation of new crystal continues while some of the nuclei are grown and a broader range of particle size obtains.

Therefore, we can conclude that decreasing reaction temperature leads to making smaller particles. But XRD results (Figure 4-6) show there is a limitation to decreasing the particles' size by lowering temperature since at lower temperature, the fraction of crystalized products drastically decreases. The XRD peaks of zeolite crystal synthetized at 100 ºC for 72 h clearly show intense peaks that have excellent compliance with zeolite LTA reference peaks. However, samples with 60 ºC reaction temperature present a few broad peaks that reveal a lower fraction of crystalized products zeolite. Samples with 40ºC reaction temperature did not give reflection in the XRD experiment.

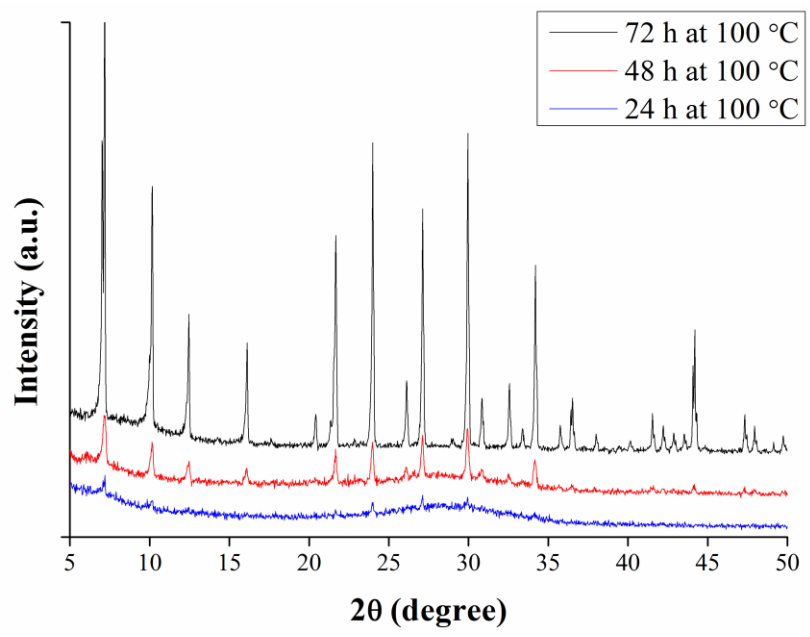


Figure 4-6. Effect of Reaction Temperature on Crystallinity of Zeolite Particles

4.5.2. Effect of Reaction Time on Zeolite LTA Crystal Size

Decrease in reaction time from 120 h to 48 h leads to forming zeolite with smaller crystal size (Figure 4-7). As SEM results show, by decreasing reaction time the size of the LTA zeolite particles decreases significantly, however, the zeolite crystals embedded in amorphous aggregates of unreacted chemicals (Figure 4-8). In the other words, reaction is incomplete and reaction yield is very low. We can conclude that the decrease

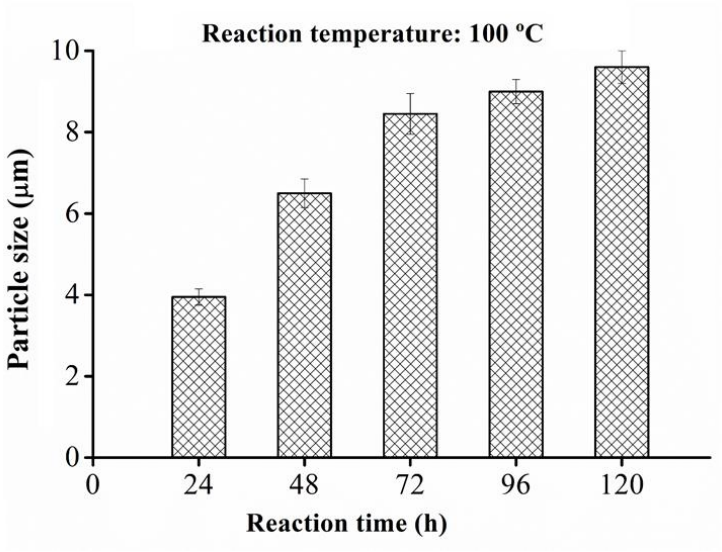


Figure 4-7. Effect of Reaction Time on Zeolite Particle Size

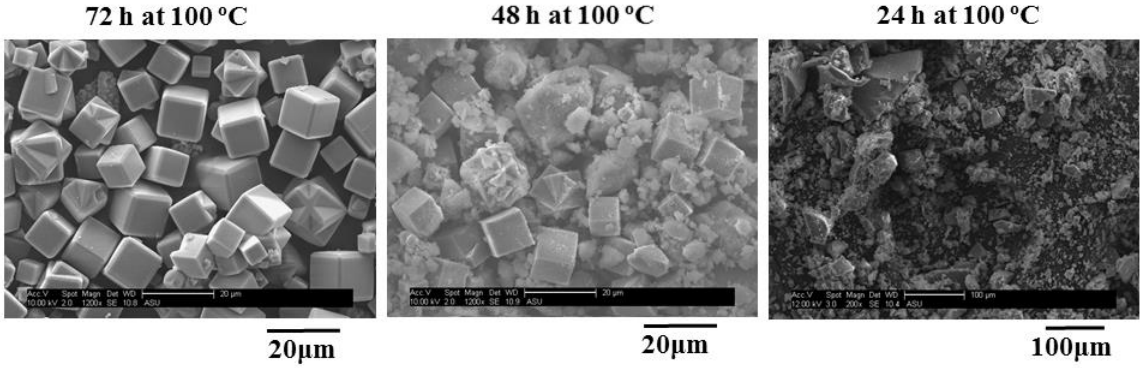


Figure 4-8. SEM Images of Zeolite LTA Synthetized with Different Reaction Time

in reaction time prevents the complete growth of particles and consequently formed particles are smaller. However, a great deal of chemical remains unreacted, therefore decreasing reaction yield.

While decreasing the time and temperature of reaction reduces the yield of the crystallization reaction, there is a tradeoff between crystallinity and particle size by decreasing reaction time or temperature. In other words, there is a limit to decreasing the particle size by reducing temperature or the time of reaction. Therefore, we investigated the effect of gel aging on particle size.

4.5.3. Effect of Time of Gel Aging On Zeolite LTA Crystal Size

Comparing the particle size of the samples without aging and the aged samples shows that aging has a significant effect on zeolite particle size (Figure 4-9). Note that the sample with 30 days aging time presents the smallest crystal size, in contrast with those at 0, 8, or 15 days of aging time. In addition, the 30-day aging time sample has morphology similar to the other samples, with the characteristic cube shape of the LTA zeolites with narrow dispersion.

As SEM results (Figure 4-9) show, the morphology of the aged samples which are crystalized at higher temperature display no difference, while that of the aged sample crystalized at lower temperature is improved to cubic-shaped crystals with planar surfaces. The average crystal size of the samples decreased from about 9μm to 2μm and 4.3 μm to 1.8μm when the gel aged for 0 to 30 days in 100 ºC and 70 ºC crystallization temperature, respectively. The decrease in particle size is sharper in the case of a particle synthesized at higher reaction temperature (100 ºC). However, in the case of particles

synthetized at lower temperature (70 ºC), which formed only a limited small crystal particles embedded in amorphous aggregates when no aged gel was used, the increase in aging time leads to formation of the sharply-edged and well-defined small crystals of zeolite LTA.

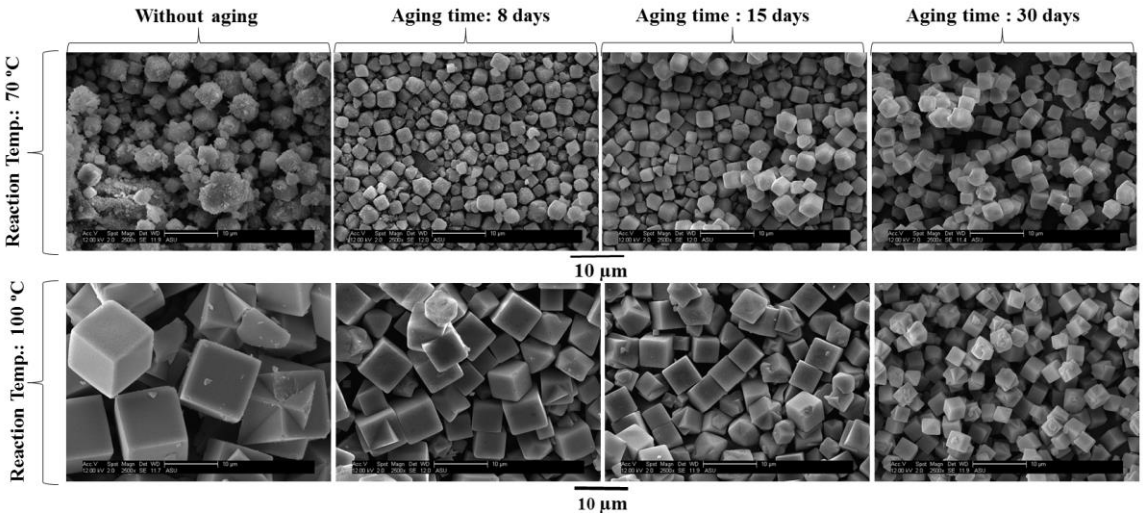


Figure 4-9. SEM Images Show Effect of Aging the Precursor Gel at Room Temperature on Size and Morphology of Synthetized Zeolite

Forming smaller particles from aged gel is evidence that the nuclei formed at room temperature are much more numerous than nuclei formed at crystallization temperature.[160] This can be explained by the fact that the formation of nuclei at lower temperature is more favorable than at higher temperature because of higher supersaturation at lower temperature. Therefore, during room temperature aging, the rate of nucleation increases significantly and a greater number of nuclei is formed. After aging, by increasing the temperature to the reaction temperature, crystal growth dominates; consequently, the formed particles are smaller with narrow size distribution. Therefore, aging at room temperature leads to high nucleation rates followed by faster growth, resulting in a large number of small crystals.

Although smaller zeolite crystals could be prepared by aging aluminosilicate gels before crystallization reaction, once the aging time is prolonged, the rate of this reduction in crystal size slowed down (Figure 4-10). After two months of gel aging, the decrease in zeolite LTA particles size is not noticeable anymore, however, the morphology of particles changes significantly. Figure 4-11 shows that by prolonging the gel aging period at room temperature, extra peaks (compared with the reference) appear. This change is discussed in the section 4.5.5.

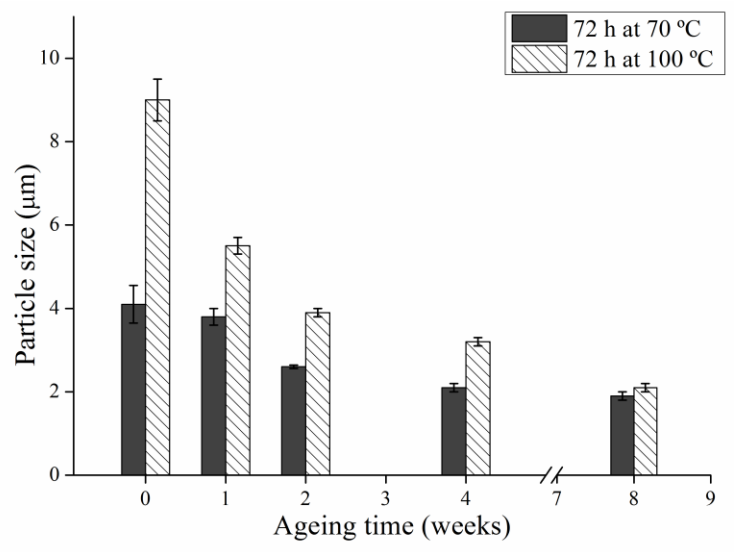


Figure 4-10. Effect of Time of Aging at Room Temperature on the Zeolite Particle Size

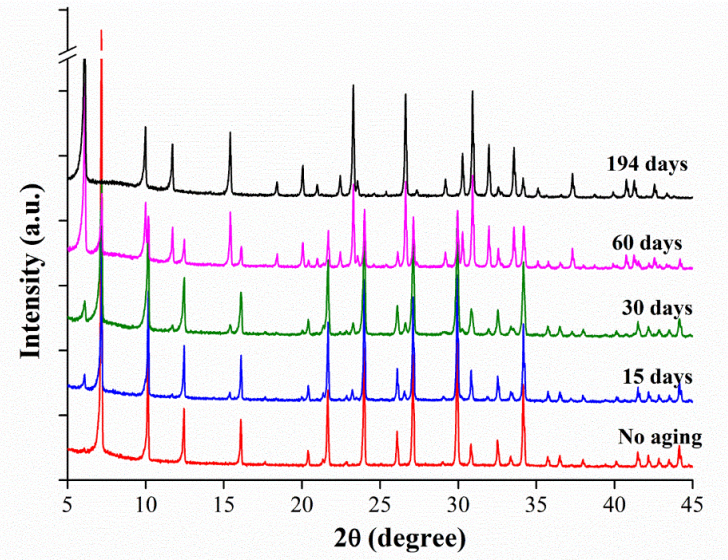


Figure 4-11. Effect of Long Room Temperature Aging on Crystallinity of Zeolite Particles, (Reaction: 72 h at 100 ºC)

4.5.4. Effect of Temperature of Gel Aging on Zeolite LTA Particle Size

We aged the zeolite LTA precursor gel at different temperatures, -20, -8, 0, 4, 8, 22 ºC, and 40 ºC, for times ranging from one week to three weeks. We crystallized all gels at 100 ºC for 72 hours. The SEM results present the morphology of the zeolites synthesized from unaged precursor gels (Figure 4-12 a) and precursor gels aged at different temperatures (Figure 4-12 b–f). The zeolites aged at temperatures lower than room temperature do not display any difference in morphology compared to the zeolites synthesized from the unaged precursor gels.

Figure 4-13 plots the average particle size of the synthesized zeolites as a function of the aging temperature with standard errors of the mean. Clearly, Figure 4-12 and Figure 4-13 demonstrate that aging temperature has a significant effect on average particle size. Zeolites synthesized from gels aged for two weeks at room temperature had an average particle size of 4.5 ± 0.56 μm, while zeolites synthesized from unaged gels

had an average particle size of 10.4 ± 0.4 μm. However, gel aging for two weeks at -8 ºC caused an extensive decrease in average particle size to 0.45 ± 0.07 μm. Based on classic nucleation theory, we expected that decreasing aging temperature would decrease particle size because aging temperature reduction increases gel supersaturation, which increases the nucleation rate. Conversely, we observed that a decrease in gel aging temperature results in unexpected changes in particle size.

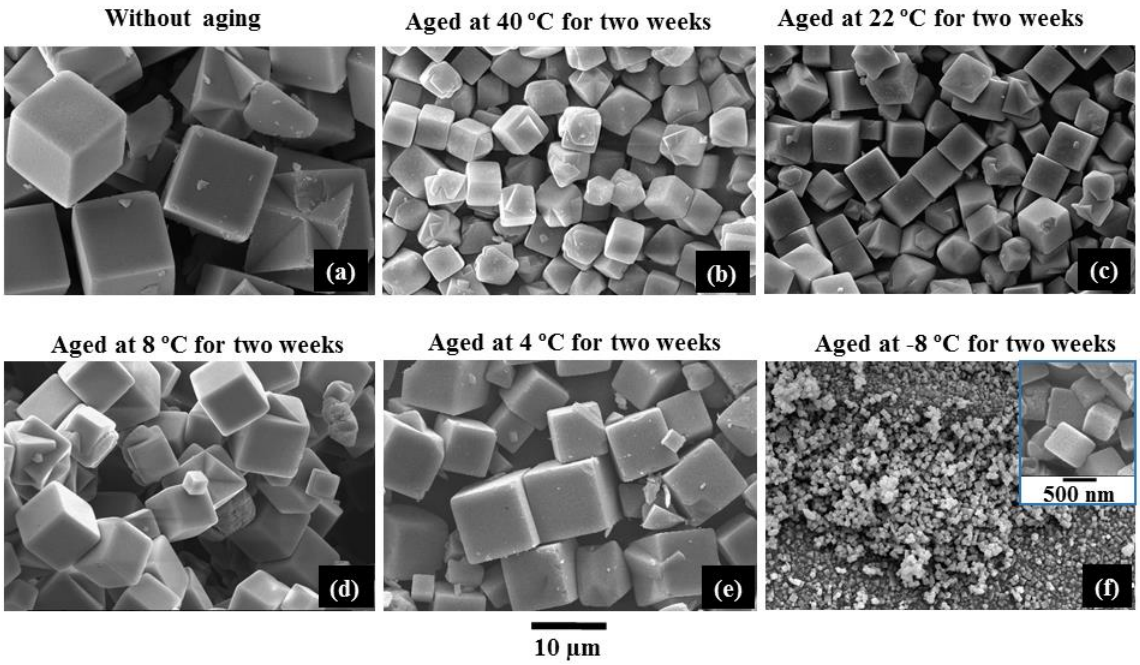


Figure 4-12. Effect of Aging Temperature on Zeolite Morphology (Crystallization Conditions: 72 h at 100 ˚C).[192]

Previous research[158,159,164] showed that aging of the precursor gel does has no effect on the linear rate of zeolite LTA growth. Therefore, the change in particle size from gel aging can be attributed to the influence of aging solely on the nucleation step. We hypothesize that the changes in particle size from changing the aging temperature of the precursor gels result from a combination of two factors: (1) phase separation (either

nucleation or spinodal decomposition), and (2) denucleation (Ostwald ripening).[180] We will discuss the effect of aging temperature on particle size in the two following intervals: aging temperatures from 40 ºC to 0 ºC and from 0 ºC to -20 ºC.

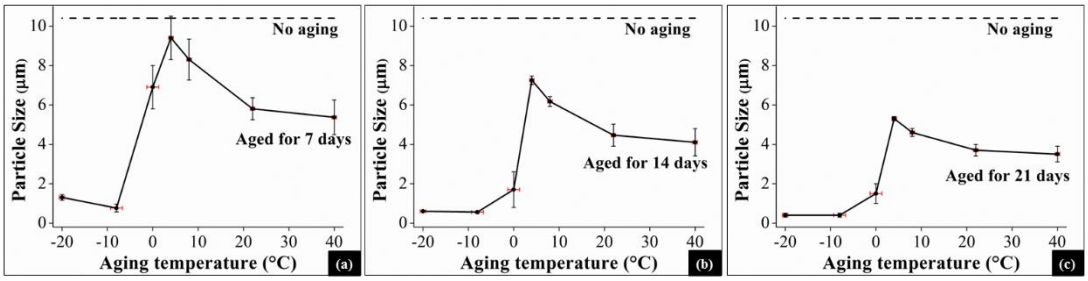


Figure 4-13. Effect of Temperature on Aged Zeolite Particle Size (Crystallization Conditions: 72 h at 100 ˚C). Each Aging Time Consists of Three Replicates. Error Bars Represent the Standard Error of the Mean.[192]

4.5.4.1. Aging Temperatures from 40 ºC to 0 ºC

Decreasing the aging temperature of the zeolite LTA precursor gel from 40 ºC to 0 ºC leads to a significant increase in particle size. We observed that the size of particles aged at 4 ºC is much larger than those aged at room temperature or 40 ºC. This is similar to the LTA results of Feoktistova et al.[160]; however, they proposed no reasons for such an unanticipated change in particle size.[160] Furthermore, we observed that by increasing gel aging time, polydispersity significantly decreases. For example, increasing aging time from one week to three weeks at 8 ºC decreases the standard deviation of particle size by 80%.

We hypothesize that the observed increase of zeolite LTA particle size as gel aging temperature decreased from 40 to 0 ºC occurs because the Ostwald ripening phenomenon dominates nucleation. As the precursor gel aging temperature decreases

(from 40 to 0 ˚C), the system tries to minimize its overall free energy. Therefore, the thermodynamically-favored larger particles (which have lower surface free energy) grow at the expense of consumption of smaller particles (which have higher interfacial free energy). Therefore, we can conclude that the increase in particle size and the decrease in the polydispersity (size distribution) in this region results from denucleation dominating nucleation. Consequently, there is formation of fewer particles with larger size as gel aging temperature decreases.

4.5.4.2. Aging Temperatures from 0 ºC to -20 ºC

Figure 4-13 also shows the effects of lowering the zeolite LTA precursor gel aging temperatures from 0 ºC to -20 ºC. Specifically, we observed that particle size significantly decreases with lower precursor gel aging temperatures. In this temperature region, the nucleation and denucleation can also be considered as possible phenomena to control nuclei numbers. In the Ostwald ripening process, after molecules detach from the surface of smaller crystals, the dissolved molecules should diffuse through the liquid phase and then deposit on the surface of large crystals.[176,177] We found that the zeolite LTA precursor gel freezes at a temperature of -2.7 ± 0.5 ˚C. Therefore, we can conclude that below the freezing point of the zeolite LTA precursor gel solution, the Ostwald ripening phenomena is negligible because diffusion through frozen media is minimal.

Lowering the precursor gel temperature increases supersaturation of the solution and makes the system thermodynamically unstable.[155] The sharp decrease in particle size observed in this region leads one to speculate that cooling to the freezing point leads to the spinodal regime, where the barrier for nucleation disappears.[168,143] At the spinodal

point, the free-energy barrier for the formation of the crystalline phase is lower than the thermal energy of the molecules; therefore, the rate of new phase generation is limited only by the kinetics of cluster growth.[173] The occurrence of spinodal decomposition creates many nuclei and causes an increase to the maximum nucleation rate.[143] Because we observe a large distribution in the particle sizes around 0 ºC, we conclude that the spinodal point of our system is very near the observed freezing point of the gel (-2.7 ºC). The wide size distribution of particles in this temperature range demonstrates that the nucleation mechanism near 0 ºC has changed. Consequently, a small variation of temperature results in a large difference in observed particle size. Our observations are similar to what Vekilov observed for the nucleation of the protein, lysozyme.[173] He observed a sharp maximum in nucleation rate of lysozyme by lowering temperature.[173] He attributed this sharp change to the existence of a spinodal through the crystal phase.[173] To investigate nuclei formation through aging, we utilized TEM. Figure 4-14 shows TEM images for zeolite gels aged for two weeks at -8 ºC, 8 ºC, and 40 ºC as well as the unaged gel. We prepared our TEM samples in ethanol to ensure that no nuclei were formed upon the drying step.[132] TEM images at Figure 4-14 (b)-(d) verify formation of nuclei through gel aging. The remarkable aspect of our TEM observation is that many crystalline structures form in the gel aged at -8 ºC (spinodal region) than those of gels aged at 8 ºC and 40 ºC. Additionally, no crystalline structure was observed in unaged gel, while several crystalline structures aggregate to form a larger crystal domain in the gel aged in -8 ºC.

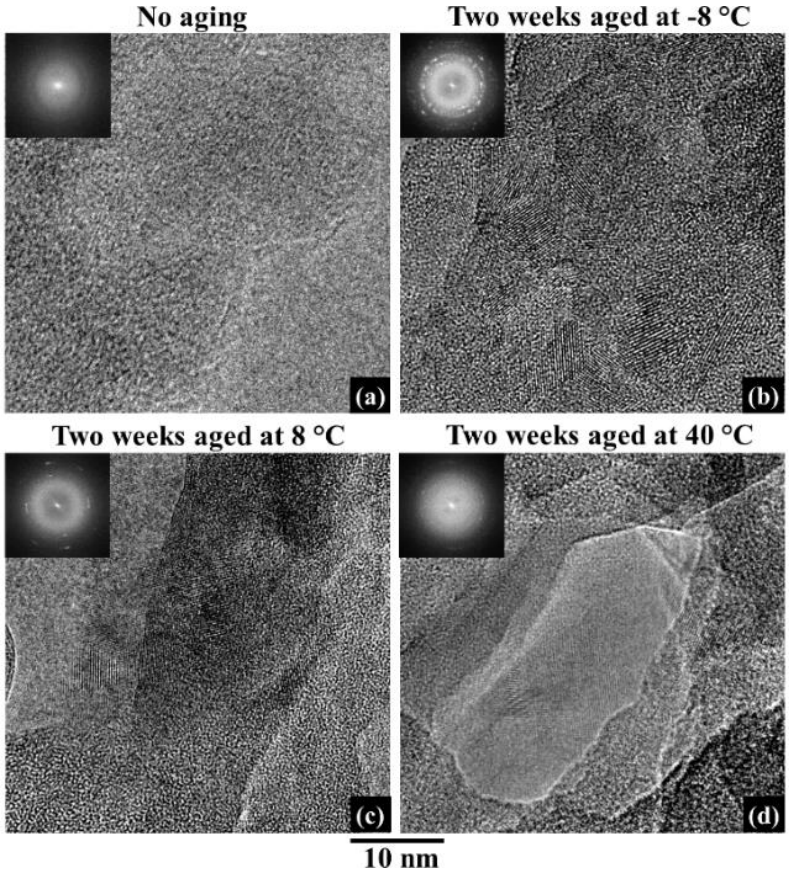


Figure 4-14. TEM of (a) Unaged Gel, and Gels Aged for Two Weeks at (b) -8 ºC, (c) 8 ºC, and (d) 40 ºC Before Crystallization Reaction at 100 ºC with the Corresponding FFT Electron Diffraction Diagram in the Insets. [192]

4.5.5. Effect of Precursor Gel Aging Temperature on Particle Crystallinity

Figure 4-15 presents the XRD patterns of the zeolites synthesized from the aged precursor gels. All patterns show the identification peaks of zeolite LTA (2-theta of 7.20º, 10.19º, and 12.49º).[193] However, there are extra peaks in the XRD patterns of the zeolites synthesized from the aged precursor gels compared with unaged samples. The samples aged at 40 ºC show new peaks arising at 2-thetas of 5.96º, 9.74º, 9.97º, and 11.42º, which are attributed to the formation of zeolite X.[193] Zeolite X is composed of four-membered ring (4R), six-membered ring (6R), and double six–membered ring (D6R)[194], and has a different crystal structure than zeolite LTA, composed of 4R, 6R, and double four–

membered ring (D4R).[195,194,196] For example, the pore diameter of zeolite X is 7.4 Å, while that of zeolite LTA is 4.2 Å.[197]

As Table 4-1 shows, aging the zeolite LTA precursor gels for two weeks at 40 ºC leads to the formation of 27% zeolite X, while aging for two weeks at -8 ºC only leads to formation of 2% zeolite X. This can be attributed to the changes in the chemistry of the precursor gel during aging.

Figure 4-16 shows the Raman spectra of the zeolite precursor gels that were separated from the unaged solution and solutions aged for two weeks at -20 ºC and 40 ºC in the region between 300 and 1200 cm^{-1}. The Raman spectrum of the 40 ºC sample is similar to the unaged sample except for a blueshift (shift to higher frequency) of the band around 1060 cm^{-1}. This blueshift is attributed to the asymmetric stretching vibration of the Si-O bond between SiO_4 and AlO_4 or between adjacent SiO_4 tetrahedra. The influence of the zeolites' Si/Al ratio on the Raman frequencies has been reported in previous research.[175-177] The significant blueshift of Raman bands of the Si-O band is attributed to the increase in the coupling between SiO4 with adjacent SiO4 or AlO4.[177] This supports the idea that the Si/Al ratio in the solid phase of the zeolite LTA precursor gel aged at 40 ºC increased[175-177] compared with that of gels aged at -8 ºC or unaged gels.

Ogura et al.[13] showed that silicate and aluminate in the solution easily form the simplest aluminosilicate of 4R.[10,13] Ginter et al.[198] showed that heating the gel leads to dissolution of more silica and thus increases the concentration of silicate anions into the solution.[198] The dissolved silicate species gradually react with the 4R aluminosilicate clusters to generate 6R clusters, which are essential to form zeolite X.[194,196] Therefore, we concluded that the appearance of zeolite X in the sample aged at 40 ˚C is likely a result of

the effect of the high temperature conditions, which increased the silicate anions in the solution and facilitated the formation of 6R clusters.

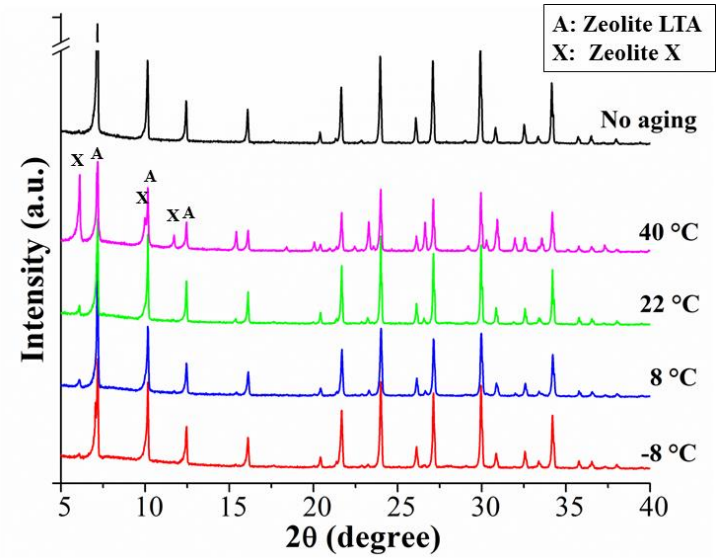


Figure 4-15. Effect of Aging Temperature on Crystallinity of Zeolites Aged for Two Weeks at Different Temperatures (Crystallization Conditions: 72 h at 100 ºC). The Label "A" Indicates the Zeolite LTA Identification Peaks. The Label "X" Indicates the Zeolite X Identification Peaks.

Table 4-1. Composition of Synthetized Zeolite from Aged Precursor at Different Temperatures. Based on PANalytical X'Pert HighScore Plus Analysis[192]

Temperature of aging (ºC)	Zeolite LTA (%)	Zeolite X (%)
No aging	100	0
-8	98	2
22	96	4
40	77	23

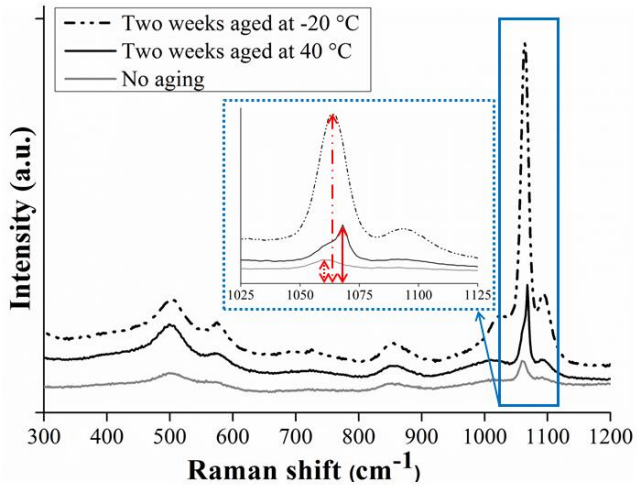


Figure 4-16. Raman Spectra of Zeolite Precursor Gels Aged for Two Weeks at -20 ˚C, 40 ˚C, and the Unaged Gel. [192]

4.6. Conclusion

For the first time, we demonstrated that aging the zeolite gel prior to the crystallization reaction at a temperature lower than 0 ˚C effectively decreases zeolite LTA particle size. Our results show that two weeks of aging the gel at room temperature results in a 56% decrease in particle size, and that two weeks of aging the gel at -8 ºC results in a 95% decrease in particle size. It is because aging zeolite LTA precursor gels near the freezing point (-2.7 ˚C) results in phase separation through spinodal decomposition, at which the nucleation barrier vanishes, and a significant decrease in particle size. The capability of freezing temperature aging to decrease zeolite particle size is significantly greater than room temperature aging.

Aging at temperatures between -2.7 and 25 ˚C increases average zeolite particle size through Ostwald ripening, spontaneous process to minimize the overall system energy by dissolving small particles and grown larger particles.

Aging above 25 ˚C changes the morphology of the zeolite. Aging at higher temperature increases the chance of formation of zeolite X due to the increased the concentration of silicate anions in the solution and consequently facilitating the formation of 6R clusters which are essential to form zeolite X.

SYNTHESIS OF INNOVATIVE MIXED MATRIX MEMBRANES

5.1. Introduction

Both reverse osmosis (RO) and nanofiltration (NF) processes have received great interest in water treatment. However, two major challenges are their low rejection of neutral nonionic molecules such as urea and their low chemical resistance[199], as discussed in detail in chapter three.

Various studies have evaluated rejection of organic chemicals through commercial RO membranes. Yoon and Lueptow[40] studied the rejection of five commercially available flat sheet RO membranes for three simulated space mission wastewaters.[40] They revealed that the solution with higher pH show higher rejection of ions because the higher pH of the solution results in higher electrostatic repulsion between ions and the membrane. They also showed that the rejection of dissolved organic carbon (DOC) depends on wastewater composition.[40] Lee and Lueptow's[39] research investigated the nitrogen compound rejection of two commercially available RO membranes. They demonstrated that while the membranes showed very high rejection (>99%) for sodium chloride (NaCl), they showed very low rejection for urea (~ 20%). Agenson et al.[200] investigated retention of a wide variety of organics, which are carcinogenic pollutants and/or endocrine disruptors, by nanofiltration (NF) and RO membranes. They showed that rejection is dependent on type of the membrane and size of the solute, though other factors like solute-membrane interaction have effects on the result.[200] The size and branching of solute functional groups has more impact on retention compared to the molecular weight of solutes.[200] Furthermore, solutes with larger widths, larger lengths, and higher logarithm of octanol–water partition coefficients show higher rejections.[200]

Kastelan-Kunst et al.[201] evaluated performance of commercial FILMTEC™ FT30 membranes (Dow Chemical Company) in removal of organic pollutants from aqueous solutions via reverse osmosis process.[201] They revealed three main conclusions. First, that the pore size distribution of the FT-30 membrane samples is narrow and unimodal with a maximum between 5.5 and 6.5 Å. Second, that reverse osmosis membrane separation cannot be thought of as a simple sieving process because there is no correlation between the organic pollutant separation coefficient and the molecular weight data. Third, that in the reverse osmosis separation process, the basic parameters are mutual interaction among the membrane material, organic nonionic solute, and water molecules, because of the observed relationship between the separation data of different organic pollutants and the solute molecule polarity.[201] Ozaki and Li investigated the rejection of ultra-low pressure reverse osmosis membranes for organic compounds.[202] They showed that retention, i.e., the percent removed, of most un-dissociated organic compounds rose linearly with molecular weight and molecular width when the molecular weight is less than 150. They also showed that feed pH and pKa values significantly influenced rejection of dissociated organic compounds.[202] Schutte[203] evaluated the rejection of two types of commercial RO membranes (cellulose acetate and composite polyamide) for various organic compounds.[203] He tested the solvophobic theory for predicting the rejection (preferential sorption) of RO membranes for organic compounds from diluted solution.[203] Radjenovic et al.[204] showed that NF/RO membranes reject more than 85% of pharmaceuticals with molecular weight greater than the molecular weight cut-off (MWCO) of NF/RO membranes.[204] However, the RO membranes showed low rejection

(73%) for pharmaceuticals with molecular size smaller than that of the MWCO of the membrane.[204]

To overcome these two limitations of RO and NF membranes, we designed a chemical-resistant mixed matrix membrane with the aim of high rejection for neutral molecules for recovering water from urine-containing wastewater. In this innovative mixed matrix membrane design, water-selective zeolites integrate into a liquid-barrier, chemical-resistant polymer film.[41] This MMM manipulates distinctive aspects of the two materials used to create the membranes: (1) the innate transport and selectivity of the molecular sieve nanoparticles and (2) the decay-resistant, versatile, and mechanical strength of the liquid-barrier polymer support matrix. Our new membrane design includes the following primary distinguishing characteristics, when compared with current mixed membranes:

First, we use an impermeable polymer matrix, enabling us to use a broader range of chemical-resistant polymers. In the case of corrosive/aggressive feed solutions, the polymer matrix of the common MMMs should have high permeability and high selectivity, as well as have high chemical resistance to feed. These criteria limit the range of polymers that can be used in a polymer matrix, or alternatively, one criterion will have to be passed up in selecting a matrix.

Second, we use latex dispersions as the polymer matrix source, enabling us to replace harsh solvent-based solutions with environmentally friendly water-based solutions. Latexes have low amounts of volatile organic compounds (VOC), low cost, and nontoxicity.

Third, we use the zeolite particles with specific pore size, to ensuring high rejection of the neutral molecules since water is transported through the zeolite rather than the polymer. By using zeolites that are somewhat larger than the expected polymer film thickness, we can ensure that zeolites penetrate the entire thickness of the polymer film and provide a single particle percolation threshold

In our mixed matrix membranes, a liquid-barrier, chemical-resistant polymer matrix binds a layer of selective molecular sieve nanoparticles into a versatile and vigorous nanocomposite thin film (Figure 5-1). This new design of mixed matrix membrane has the potential to address challenges of chemical compatibility.

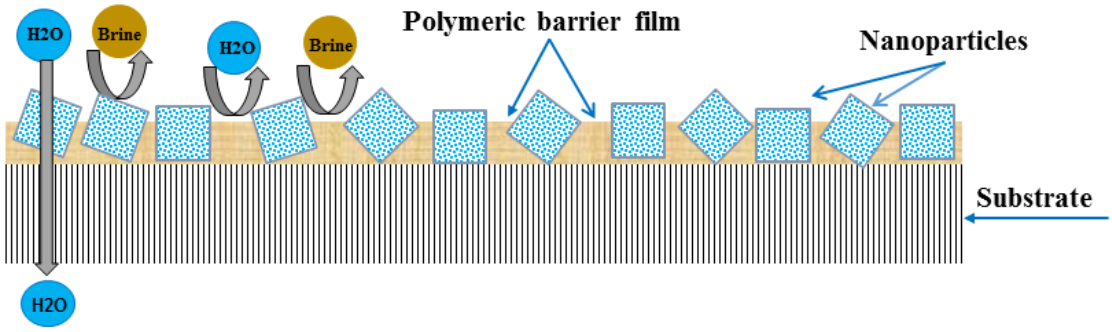


Figure 5-1. Schematic of Innovative Mixed Matrix Membrane in which the polymeric barrier film acts as a glue binding the molecular sieve particles.

5.2. Materials

Following chemicals are used in this study to optimize the method for synthesis and evaluation of the new design mixed matrix membrane: polyvinylidene chloride (PVDC, PVDC Diofan B204, Solvay), (3-aminopropyl)triethoxysilane (APTES, Sigma Aldrich), (3-glycidyloxypropyl)trimethoxysilane (GPTMS, Sigma-Aldrich), (3-chloropropyl)triethoxysilane (CPTES, Sigma-Aldrich), 3-chloropropyltrichlorosilane

(CPTCS, Sigma-Aldrich), acetone (99.9%, Sigma-Aldrich) , DI water, 0.02μm pore size anodized aluminum oxide membranes (AAO, Anodisc^{TM} 6809-5002, Whatman), dimethylformamide (DMF, Sigma Aldrich), and toluene (Alfa Aesar), acetone (Sigma Aldrich), dichloromethane (DCM, Sigma Aldrich), hexamethylphosphoramide (HMPA) and tetramethylene sulfoxide (TMSO), sodium chloride (NaCl, Sigma-Aldrich), and Rhodamine B (RB, $C_{28}H_{31}ClN_2O_3$, Acros).

5.3. Methods

We prepared Linde Type A (LTA) zeolites of various sizes according to the procedures of chapter four. We added the silane agent (ATES, GPTMS, CPTES or CPTMS) to the sonicated mixture of solvent (DMF, DCM, acetone or toluene) and zeolite. We left the zeolite in the silane solution overnight. Then we washed the zeolite with copious amounts of solvent through repeated sonication, centrifugation and decanting and put them in an oven at 85 °C for 4 h. Then, the zeolite was dispersed in the solvent and sonicated for 2 h. We cleaned the porous substrate (Anodisc) by immersing it in the boiling water for 1 h and then dried it under a gentle stream of argon. The cleaned substrate was immersed in the dispersion of zeolite in solvent and left overnight. At the last step, after washing the Anodisc substrate with copious amounts of solvent, it was dried at 85 °C for 4 h.

We prepared the polymer coating solutions by diluting the PVDC latex to a solid concentration of approximately 5 to 11 wt% (based on the results presented in chapter 2). We used dip coating to deposit a thin layer of the polymer latex solutions onto the Anodisc. To prevent the PVDC solution reaching the other side of the substrate, the

substrate was sealed on the Petri dish by using Parafilm®. First, we poured the PVDC solution on the side of substrate on which the zeolite particles were anchored. Second, after holding the substrate within the latex solution for 40 seconds, we removed latex solution and held the substrate vertically (to allow the excess solution to drip from the surface) under our previously determined slow drying procedure (24 h at 22 °C and 95% RH, followed by 24 h at 22 °C and 25% RH).[90]

5.4. Characterization

We used scanning electron microscopy (SEM, FEI/Philips XL-30 Field Emission ESEM-FEG, USA) to evaluate the morphology of the membrane. We performed water permeation tests using a hydraulic dead-end filtration system (HP4750 Stirred Cell, Sterlitech Corp., USA) at 20 bar pressure. Experimentally, the water permeability coefficient, A [μm s^{-1} MPa^{-1}], is the measured liquid flux through a membrane normalized by the pressure applied across a membrane, presented in Equation 5-1.

$$A = \frac{J_W}{(\Delta P - \Delta \pi)} \qquad \textbf{Equation 5-1}$$

Here, J_W [μm s^{-1}] is osmotic water flux calculated by dividing the volumetric flux by the membrane area, ΔP [MPa] is the applied pressure, and Δπ [MPa] is the osmotic pressure.

To characterize membrane rejection performance, we tested our membrane with Milli-Q water, NaCl (20 mM), and Rhodamine B (7.5 mg/L) solutions in the mentioned order, one at a time. The membrane was rinsed with Milli-Q water after each rejection test. The membrane's rejection of NaCl was measured by using a conductivity meter (Accumet Excel XL50, Fisher Scientific, USA). The rejection of membrane for

Rhodamine B was measured by using a UV-Vis spectrophotometer (UV-1700, Shimadzu, Japan). The rejection was calculated by

$$R = 100 \times \frac{(C_f - C_p)}{C_f}$$ ***Equation 5-2***

where C_f is solute concentration in feed [g/L], C_p is solute concentration in permeate [g/L] and R represents the rejection coefficient (%).

5.5. Results and Discussion

5.5.1. Effective Procedure to Synthesize the Innovative Mixed Matrix Membrane

First we synthetized the mixed matrix membrane by the standard procedure of dispersing the zeolite particles in the polymer matrix casting solution and then coating on a substrate followed by drying through solvent evaporation. However, the obtained membranes show no permeation flux for water for two reasons shown in Figure 5-2.

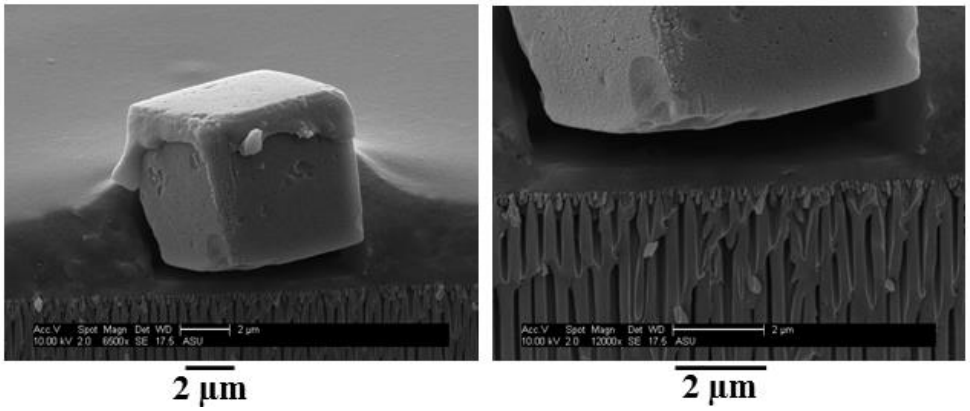


Figure 5-2. SEM Images of Zeolite in Composite Membrane Covered by the Impermeable Polymer

First, the impermeable polymer is deposited on the surface of the zeolite; therefore, zeolites are not exposed to water. Second, an impermeable polymer film is formed between zeolite particles and porous substrate, which prevents any water that penetrates the zeolite from exiting through the substrate. To prevent these obstacles we performed the following two tasks: (1) we anchored the zeolites to the substrate to prevent polymer formation between the substrate and the zeolite and (2) we performed etching of the top surface of the membranes to remove any polymer blocking the top pores of the zeolite.

5.5.2. Anchoring Zeolite Particles on Porous Substrate Using Silane Linkages

To prevent formation of an impermeable polymer layer between the zeolite particles and the porous substrate, we anchored the zeolite particles onto the porous substrate using silane covalent linkers. The goal of using a silane agent is to form bonds across the interface between zeolite particles and substrates. Indeed, an ultrathin layer of molecular linkage is placed between the zeolite and the porous substrate. Previous studies[205-210] investigated anchoring zeolite to solid substrates; however, our primary goal is anchoring zeolite to porous organic and inorganic substrates.

5.5.2.1. Immobilizing Zeolite to Non-Porous Substrates

Ha et al.[211,206] micropatterned zeolite particles onto glass by using silane covalent linkages. They treated the glass with (3-chloropropyl) trimethoxysilane (CPTMS) in toluene in order to anchor 3-chloropropyl (CP) groups on the glass plates, because siloxane linkages tend to react with the hydroxyl groups of zeolite surface and

consequently anchor the zeolite to glass.[211] A different study investigated the effect of various silylating reagents. They obtained the comparable coverage and bond strengths by using different silane agents which have different halide as well as different type and number of anchor groups on the silicon center.[205] Kulak et al.[207] demonstrated that polyamines effectively increase the strength of binding between the substrates and zeolite crystals. Using the polyamine specifically is beneficial for assembling micrometer-sized zeolite crystals, which need a large number of interconnects onto uneven curved glass surfaces.

Chun et al.[212] presented the capability of urethane agents for anchoring a monolayer of zeolite onto glass, these are effective because isocyanate groups have a high tendency to form urethane linkages with hydroxyl groups on glass and zeolites surfaces.[212] They showed that diisocyanates are an effective molecular binder to anchor zeolite crystals to glass substrates. Park et al.[213] anchored a highly oriented, closely packed mono- or multi-layer of zeolite microcrystal onto glass by making adenine-thymine hydrogen bonding.[213]

5.5.2.2. Immobilizing Organic Molecules to Porous Alumina Substrate

Some researchers have attempted to immobilize biomolecule proteins such as antibodies and enzymes to nanoporous alumina substrates.[214] Vlassiouk et al.[215] covalently linked DNA to modified nanoporous alumina. Their immobilizing process included three steps of silanization of the porous substrate using aminosilane, activation of the surface with glutaraldehyde, and finally covalent attachment of 5′-aminated DNA oligomer.[215] In another study, Vlassiouk et al.[216] silanized nanoporous alumina substrate

to immobilize DNA and used it to detect and separate/purify unmodified target DNA (and RNA).[216]

Despite abundant studies on anchoring biomolecules to nanoporous alumina substrates, to the best of our knowledge there are only two reports on anchoring inorganic particles to porous substrates. Holber et al.[214] immobilized (self-assembled) quantum dots (semiconductor nanoparticles) on nanoporous alumina using silane linkages. Szczepanski[210] anchored zeolites to porous alumina substrates, in which the alumina surface was passivated silica. Szczepanski et al.[210] showed that the stability of silanes covalently bound to the surface of nanoporous alumina substrates depends on the type of linker used. They passivated alumina surface with an atomic layer of silica in order to increase the stability of immobilized molecules on alumina surface.[210]

Most of the before-mentioned studies investigated the self-assembly of zeolite on flat solid substrates which have many functional groups (e.g., glass, silica and metal). Furthermore, they mostly used environmentally unfriendly organic solvents such as toluene. To the best of our knowledge, studies about anchoring zeolite to more common substrates (e.g., rough surfaces, or containing fewer functional groups) are rare. Consequently, creating applications of zeolite-oriented layers or films, and advancing a straightforward, efficient and environmentally friendly means to organize zeolite microcrystals directly, on a range of substrates under varied surface conditions, with a preferred orientation, is highly desirable.

5.5.2.3. Principle of Silanization Reaction

Reaction of the silane agents involves four steps; initially, the three hydrolyzable groups of silane agents are hydrolyzed to form silanol-containing structure, and then silanol groups are condensed to oligomers. Silanetriols are most stable at pH 3–6, but condense rapidly at pH 7–9; therefore, if the pH increases, the condensation rate increases. The oligomers and -OH groups of the substrate/zeolite formed hydrogen bond. Finally, a covalent linkage is formed during drying or curing. After exposing the functionalized zeolite / substrate to a non-functionalized zeolite / substrate, the hydroxyl

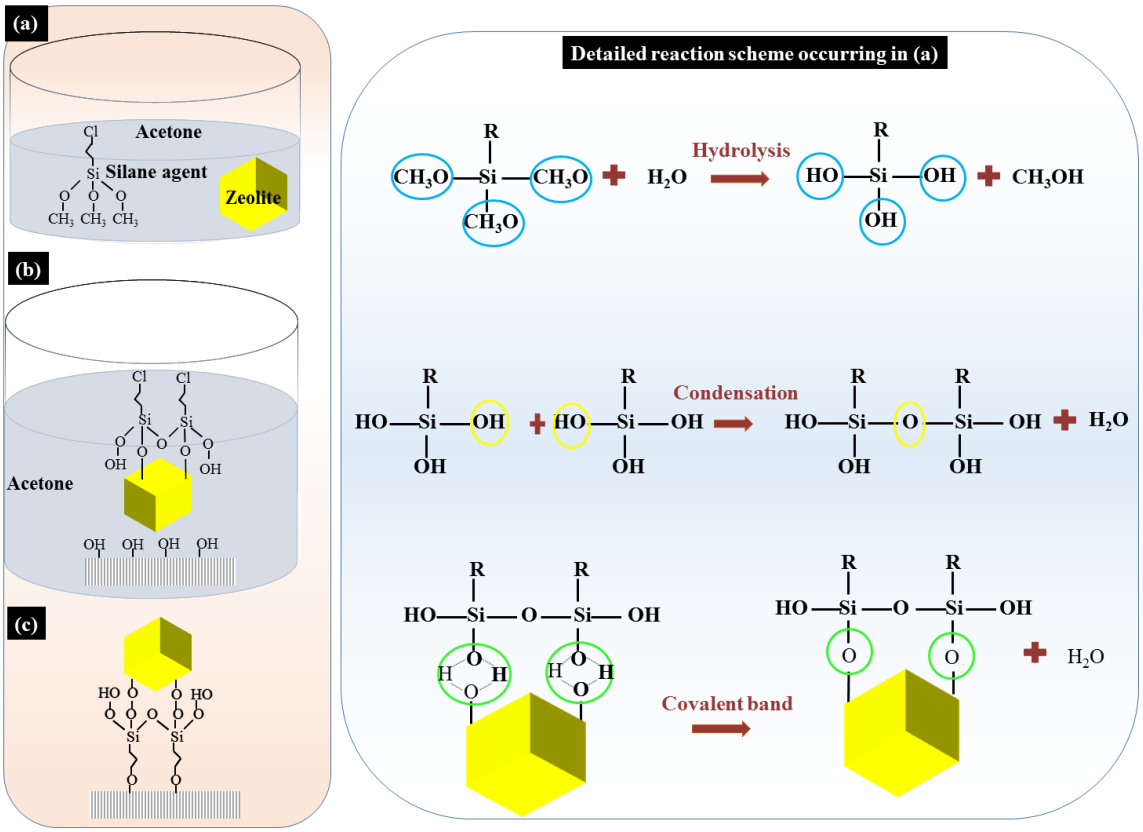


Figure 5-3. Schematic Procedure to Anchor Zeolite LTA to a Porous Substrate Using a Silane Agent (Left, (a), (b), and (c)), and the Mechanism of Reactions between Silane Agent and Zeolite (Right)

groups of the zeolite or of the hydroxylated substrate attack and displace the alkoxy groups on functionalized component, thus forming a covalent -Si-O-Si- bond (Figure 5-3).

5.5.2.4. Effect of Silane Agent and Solvent

We used different silane agents as a covalent linker and various solvents with different dipole moments to control formation of a uniform dense monolayer of zeolite particles on the porous substrate. The various silane agents (CPTES, CPTCS, GPTMS, and APTES) are selected based on their leaving group, a molecular fragment which departs with a pair of electrons in heterolytic bond cleavage (Figure 5-4). The ability of their leaving group defines the rate of silane agents' reaction. In addition, we used various solvents, including acetone and dimethylformamide (DMF) as polar aprotic solvents and toluene, and dichloromethane (DCM) as nonpolar solvents. The polarity and the ability of the solvent to stabilize the intermediate carbocation have an effect on the silanization reaction rate.

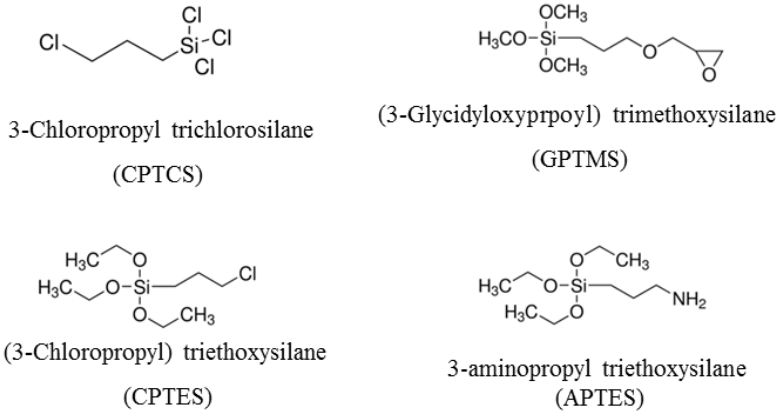


Figure 5-4. Chemical structure of silane agents used in this study

Figure 5-5 shows SEM results of three different silane agents and solvents used to anchor zeolites to porous substrates. For example, Figure 5-5 a shows that CPTCS covers the zeolite surface when it is treated with toluene. However, CPTES in toluene cannot effectively anchor zeolite to substrates (Figure 5-5 b) and CPTES in DMF causes noticeable aggregation of particles (Figure 5-5 d).

CPTCS is polymerized on the substrate and blocks the substrate pores when used with DMF (Figure 5-5 c). This issue (blocked pore of Anodisc) can be attributed to the vigor of their leaving group. All used organosilanes have three hydrolyzable substituents. Ordinarily, a single bond exists between each silicon atom of the organosilane and the zeolite or Anodisc surface. The two remaining silanol groups are present in either condensed or free form. In the case of CPTES and CPTCS, which have the strongest leaving groups, the chance of condensing two adjacent leaving groups to make continuous film is high.

The best result for anchoring LTA zeolites to anodicsc wasobtained by using APTES and GPTMS (Figure 5-5 e and f), which have weaker leaving groups. A mixture of APTES and acetone anchor more zeolite particles to the substrate in comparison with the other silane agents and solvents tested. The linkage formed by the opening of the nucleophilic ring of the epoxy group on APTES tethers to Anodisc, and the amine group on APTES tethers to zeolite particles.

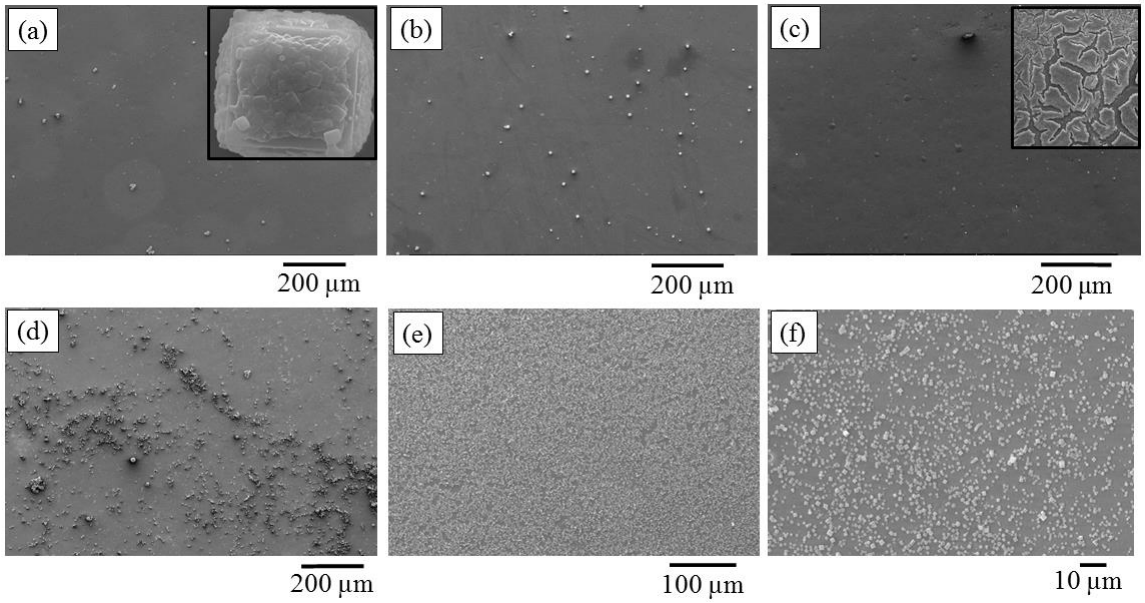


Figure 5-5. SEM Images showing the LTA Zeolites Anchored to Anodisc Substrate Using Various Silane Agent and Solvents; (a) CPTCS in Toluene, (b) CPTES in Toluene, (c) CPTCS in DMF, (d) CPTES in DMF, (e) APTES in Acetone, and (f) GPTMS in Acetone.

5.5.2.5. Effect of Silanization Procedure

We explored three different procedures for anchoring zeolites to Anodiscs:

1) silanized solely zeolite
2) silanized solely Anodisc
3) silanized both zeolite and Anodisc.

We obtained the best results (highest uniform density of coverage with minimal aggregation) when just one component was silanized (Figure 5-6). When both particle and substrate are silanized, the lowest density of anchored particles to Anodisc is obtained. Indeed, the zeolite particles anchored using silane groups on the surface did not bind to the silane-tethering Anodisc. This result clearly proves that, in order to form a covalent link between the zeolite particles and substrate, the existence of both a silane

group and hydroxyl groups is necessary. In the other words, we can conclude that when zeolite or substrate is silanized, the functional group on zeolite or substrate will be -NH, or -Cl which tend to make a hydrogen bond with -OH group of non-functionlized zeolite/Anodisc. However, when both the LTA zeolite and Anodisc are silanized there is a much lower tendency between the two -NH groups to react. Also, aggregation of particles in this case observed more than in the case where just the zeolite or substrate is silanized. This is beacause the -NH group of some particles bond with -OH group of other particles.

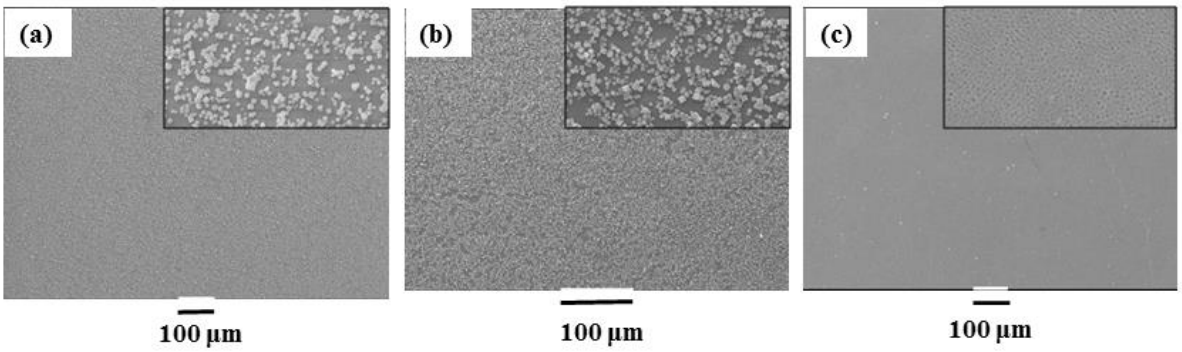


Figure 5-6. SEM Images of the Zeolite Anchored to Anodisc Substrate Using APTES at Room Temperature through (a) Silanization of Zeolite, (b) Silanization of Anodisc, and (c) Silanization of Both Zeolite and Anodisc

5.5.2.6. Lower Density of Anchored Zeolite to Alumina Porous Substrate Compared with Silica-Based Solid Substrates

While previous research[206] showedhigh density of anchored zeolites to nonporous silicon-based substrates, our results showed lower density of anchored zeolites to pourous alumina-based substrate. We hypothesize the main reason for lower density of anchored zeolite to alumina substrate is to the result of the difference in polarity of Si – O and Al –

O bonds. The Al – O bond is more polar than the Si – O bond, therefore, Al – O – Si is more polarized and consequently is much more vulnerable to activation by a base or an acid than Si – O – Si.[210]

The lower packing density of zeolites onto alumina substrate in comparison to packing density of zeolites onto silica substrate can be attributed to higher reactivity of silicone oxide in comparison to alumina oxide. The Al – O bond (μ= 2, D_{o298}= 512 kJ mol^{-1}) is more polar and less vulnerable than the Si – O bond (μ= 2, D_{o298}= 798 kJ mol^{-1});[2] therefore, the covalent bond between the silicone of the silane agent and the alumina substrate is more polarized than the bond between the silicone of the silane agent and the silicon substrate. Therefore, we can conclude that since the Si-O-Al linker is highly polarized, it is more vulnerable.[210]

Furthermore, we believe that substrate's porous nature has a significant effect on anchoring density. As previous research reported, a micrometer-sized cubic zeolite-A crystal requires over 600,000 interconnects in order to anchor to solid supports.[205] Additionally, it was demonstrated that the uneven nature of the surfaces of zeolite-A crystals and the supports decrease the real number of interconnecting covalent linkages, because each surface-anchored component is shorter than the peak-to-valley depths on each uneven surface, as shown in Figure 5-7. Therefore, we can conclude that the foremost reason for the lower number of covalent linkages in our results is due to the porosity of the surface.

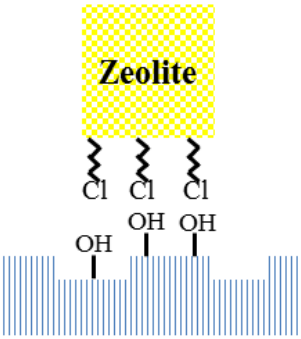


Figure 5-7. Schematic of Anchoring Zeolite to Not-Smooth Substrate, Image Reproduced from Kulak.[207]

5.5.2.7. Effect of Size and Concentration of Zeolite Particles

We used the various sizes of zeolite LTA particles (0.45, 1.5, 3, and 6 µm) at two different concentrations of zeolite in anchoring solution (0.5 and 1 wt. %). While zeolites with sizes larger than one micrometer show uniform dispersion (Figure 5-8), the small particles (0.45 µm) show noticeable tendency to aggregate. Therefore, a decrease in the size of particles leads to a significant increase in the aggregation of particles. The aggregation of zeolite particles prevents PVDC from effectively filling the gaps between

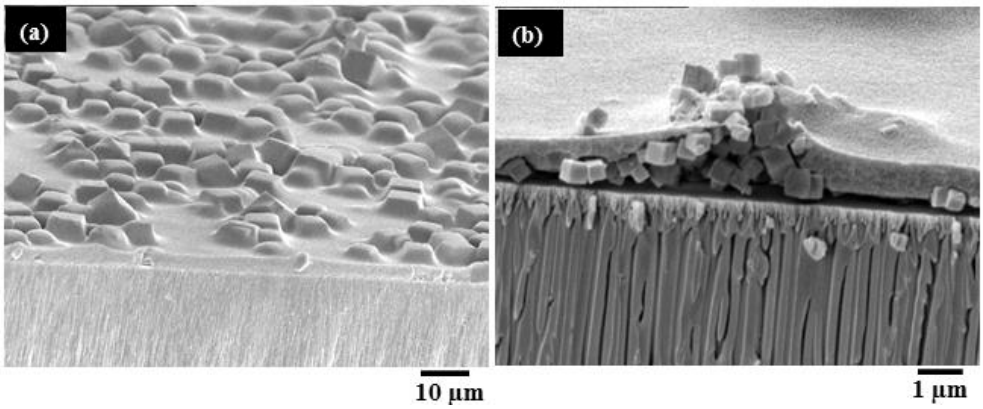


Figure 5-8. SEM Images of Membrane Cross Section Show (a) High Density of Large Zeolite (1 wt% Loading 6 µm Zeolite) Anchored to Anodisc Substrate Without Aggregation, (b) Aggregation of Small Zeolite (1 wt% Loading of 0.45 µm Zeolite).

the particles and forming a defect-free film. Therefore, we decreased the concentration of zeolite to 0.5 wt% to prevent aggregation.

5.5.3. Remove Impermeable Polymer Layer from Zeolite Surface

After anchoring the LTA zeolites to the substrate, we formed a thin polymer barrier film via dip-coating to fill the gap between the particles. As Figure 5-2 shows the impermeable polymer formed a layer on top of the zeolite and prevented zeolite exposure to the feed water. To remove this excess PVDC polymer layer, we applied either oxygen plasma or chemical etching to the surface, thereby exposing the zeolite particles to water.

5.5.3.1. Chemical Etching

Hexamethylphosphoramide (HMPA) and Tetramethylene sulfoxide (TMSO) are two solvents of PVDC that we used to remove the polymer layer from zeolite surface. First, the composite membrane was placed with the active side (coated side) down into a dish filled with the TMSO or HMPA for a predetermined amount of time. After which, the membrane was completely washed with DI water. As SEM images (Figure 5-9 a) show the membranes were destroyed when the solvent was not diluted prior to use. Therefore, we systematically changed both the concentration of solvents (10-60%) and etching time to optimize the results. Evaluation of the SEM results show that HMPA does not sufficiently remove polymer from the surface of zeolite. The best results have been attained by using 40% TMSO. However, while one minute of etching with 40% TMSO is not enough to remove PVDC from zeolite surface, two minutes of etching creates some gaps at the interface between particles and polymer.

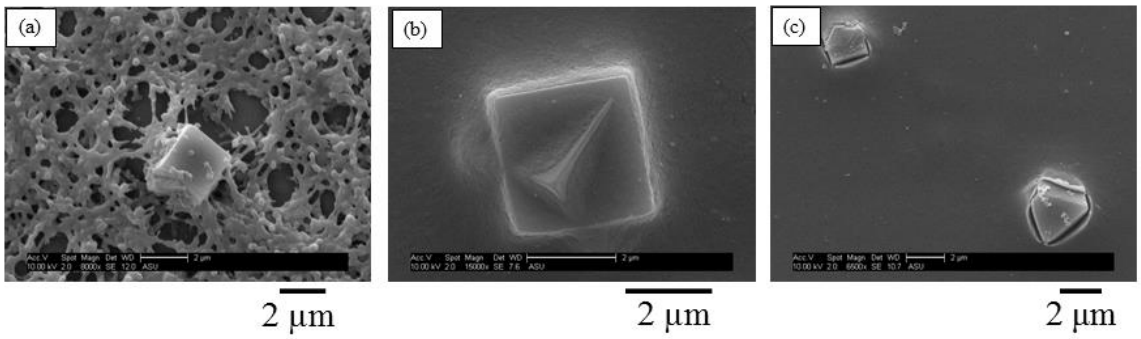


Figure 5-9. PVDC-Zeolite Composite After Chemical Etching by (a) 100% TMSO for 1 min, (b) 40% TMSO for 1 min and (c) 40% TMSO for 2 min

5.5.3.2. Oxygen Plasma

Oxygen plasma (plasma cleaning) is an effective and environmentally safe method for removal of organic contaminants by chemical reaction with highly reactive oxygen radicals and ablation by energetic oxygen ions. The plasma is created by using high frequency voltages to ionize the low pressure gas that is excited to higher energy states.[217] We changed the time (1 to 30 min) of oxygen plasma (7.2 W, 500 mTorr) systematically changes to obtain best results. As SEM results (Figure 5-10) show that 20 minutes of oxygen plasma leads to sufficient zeolite surface cleaning.

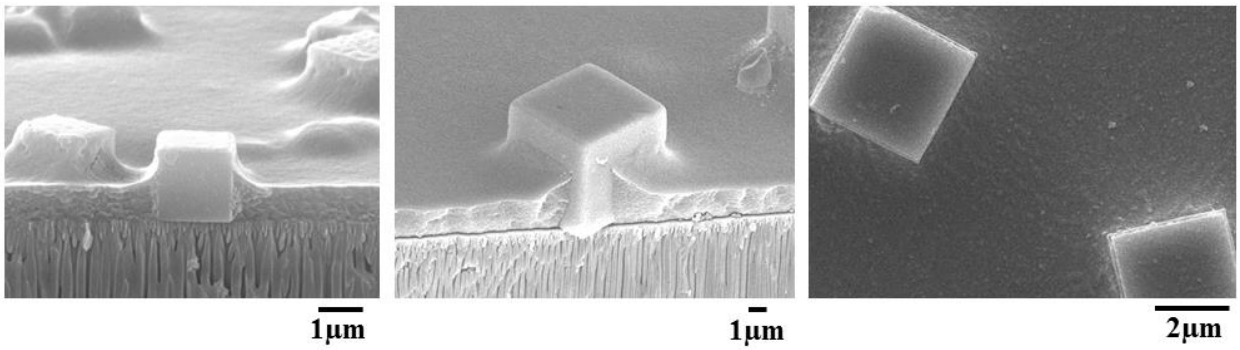


Figure 5-10. SEM Image of PVDC-Zeolite Composite After 20 min Oxygen Plasma

Figure 5-11 summarizes the overall membrane synthesis procedure. The first step is functionalizing the zeolite particles using silane agents such as APTES. Second step is anchoring the functionalized zeolite particles to the porous substrate. The third step is filling the gap between the particles using a chemical resistant impermeable polymer such as PVDC. The last step is removing impermeable polymer film formed on the zeolite surface using oxygen plasma to expose the zeolite to feed water.

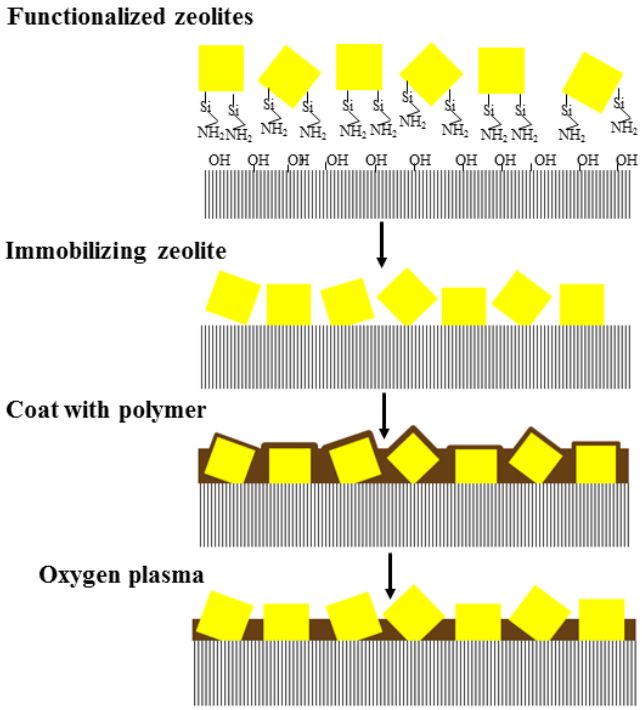


Figure 5-11. Overall Procedure of Making Innovative Mixed Matrix Membrane; Tethering LTA Zeolites to Anodiscs with Silane linkage, Forming a Latex PVDC Film, and Oxygen Plasma Etching to Remove Excess PVDC.

5.5.4. Permeation Results

To evaluate the performance of innovative designed membrane in recovering water, we performed water permeation tests using a hydraulic dead-end filtration system at 20

bar pressure. Figure 5-12 shows the permeation coefficient for pure water and rejection of a monovalent salt (sodium chloride) and an organic dye (rhodamine B).

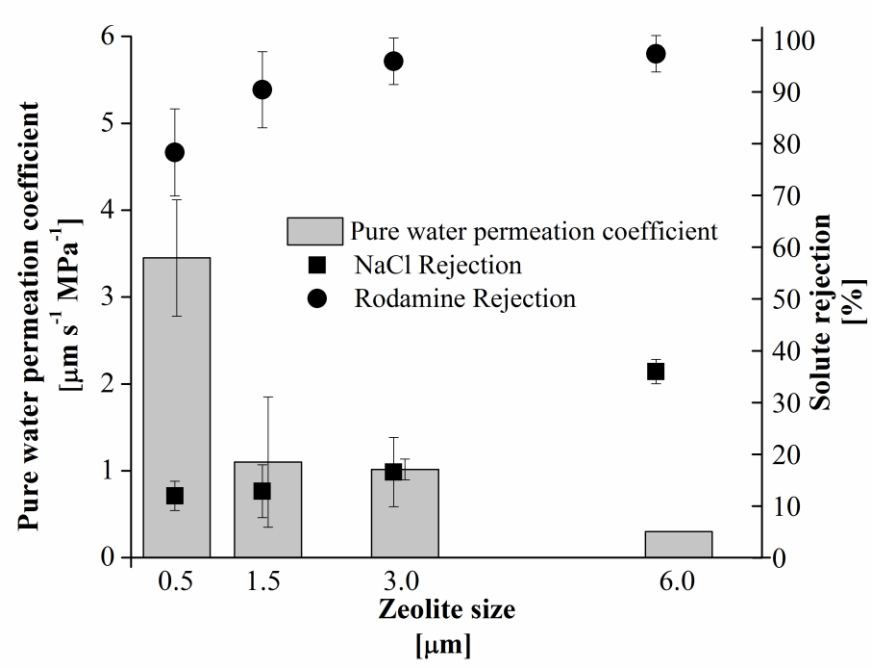


Figure 5-12. Permeation Results of the Prepared Membranes.

The prepared membranes show low rejection of the NaCl (less than 36%) and high rejection of the dyes (more than 78%). The low NaCl rejection of the membrane shows that defects exist in membrane that creates nonselective transport pathways through the membrane. However, because the membrane shows the size exclusion effect for larger organic molecules (higher rejection for larger molecules) most of the membrane defects should be nano-size defects; Therefore, the higher rejection rate of rhodamine B (Mw: 479.02 g/mol), than NaCl (Mw: 58.44 g/mol), can be attributed to its higher molecular weight.

Anodisc has bulk pore size of 200 nm and top-layer pore size of 20 nm. If there is defect in the Anodisc's top layer as shown in Figure 5-13, instead of micro porous substrate for membrane, we will have a mesoporous substrate. As we discussed in section 2.5.5, the chance of making defect free latex film on a mesoporous substrate is much less than on a micro porous substrate. Therefore, defects in the Anodisc (Figure 5-13) can be considered as a potential reason for the observed low NaCl rejection, because they result in formation of defective film, which leads to nonselective transport of the water through the membrane.

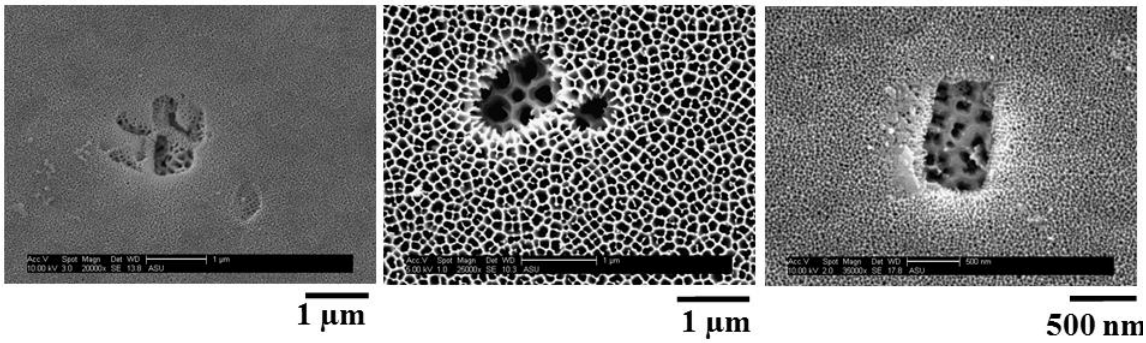


Figure 5-13. Defects in Top Layer of Anodisc.

By increasing the zeolite size from 0.5 to 6 µm, the rates of rejection of NaCl increased from 12.00 ± 2.80 % to 36.48 ± 2.35 % and rejection of rhodamine B increased from 78.30 ± 8.40 % to 97.38 ± 3.50 %. This result shows that the defects decrease with an increase in zeolite particle size. Therefore, we can conclude the aggregation of small particles (as shown in Figure 5-8) can be considered as another potential reason for the defects in membrane which leads to nonselective transport through the membrane.

By increasing the size of zeolite particles, permeation decreases from 3.5 ± 2.87 to 0.30 ± 0.015 $\mu ms^{-1}MPa^{-1}$. The decrease in permeation coefficient can be attributed to the increase in resistance to transfer of water through the membrane because of the increase in path of the water in membrane (the size of zeolite). Based on the design of new membrane, the zeolite pore is the pathway for transport the water through the membrane, so larger particles make a longer pathway, and leads to higher resistance to water transport.

SUMMARY AND FUTURE WORK

6.1. Conclusion

Today's membrane processes offer the capability to increase water recovery from wastewaters—pretreated urine and urine brines. As mentioned, the key drawback is that commercial RO membranes rapidly break down when exposed to acidic pretreated urine and urine brines. Furthermore, another problem with commercial osmotic membranes is that despite their high rejection of ionic solutes (99%), they lack a sufficient barrier to small organic compounds commonly found in urine, such as urea.[39,218,219] The broad goal of our research is to develop strong mixed matrix membranes that will fortify the performance and speed up the execution of membrane-based water production technologies.

The main distinguishing characteristics of our new membrane design compared with current mixed matrix membranes include: (1) we use an impermeable polymer matrix enabling a broader range of chemical resistant polymers; and (2) we use latex dispersions as the polymer matrix source. We manipulated the distinctive properties of polymer-nanomaterial mixed matrices to produce efficient separation membranes with customized performance. In our design, the zeolite particles are anchored to the porous substrate, while a liquid-barrier, chemical-resistant polymer matrix fills the space between the particles and binds zeolite nanoparticles into a versatile nanocomposite thin film. The objective of this study was to make a first systematic development and characterization of this new designed membrane to recover water from corrosive wastewater.

In the present stage, the synthesized membranes show promising rejection of organic molecules. Further adjustment of the new design chemical resistant pressure-driven membrane will hopefully improve its performance. Strategies for improvement could include:

1. Controlling the space between the zeolite particles by changing the zeolite concentration.
2. Modifying the anchoring by functionalizing zeolite with different functional groups to make oriented monolayer of zeolite.
3. Optimizing polymer layer thickness by varying the concentration of polymer latex.

Indeed, the synthesis of this new type of impermeable polymer based membranes with improved performance encouragingly meets the criteria of a next generation technology, one that may be a viable alternative to current commercial membranes for water separation applications.

REFERENCES

1 Carter, L. in *Environmental Systems* 1-11 (American Institute of Aeronautics and Astronautics, Barcelona, Spain, 2010).

2 Bundschuh, J.;Hoinkis, J. *Renewable energy applications for freshwater production*; CRC Press/IWA Pub.: London, 2012.

3 AWWA Research Foundation.;Lyonnaise des eaux-Dumez (Firm);South Africa. Water Research Commission. *Water treatment membrane processes*; McGraw-Hill: New York, 1996.

4 Shiklomanov, I. s. c. in *Water in Crisis: Guide to the World's Fresh Water Resources* (ed Peter H. Gleick) (Oxford University Press, **1993**).

5 Goulding, C. R., Bonafé, A., Goulding, C. G., . *The R&D Tax Aspects of the Growing U.S. Water Shortage*, 2014).

6 El-Dessouky, H. T.;Ettouney, H. M. *Fundamentals of salt water desalination*; Elsevier: Amsterdam ; New York, 2002.

7 Gleick, P. H.;Pacific Institute for Studies in Development Environment and Security.;Stockholm Environment Institute. *Water in crisis : a guide to the world's fresh water resources*; Oxford University Press: New York, 1993.

8 Krishna-Hensel, S. F. *New security frontiers : critical energy and the resource challenge*; Ashgate: Farnham, Surrey, England ; Burlington, VT, 2012.

9 Finkbeiner, M. *Special types of life cycle assessment*; Springer: 2016.

10 Loff, S. *Mars Planning Frequently Asked Questions*, 2012).

11 NASA SPACE TECHNOLOGY ROADMAPS AND PRIORITIES: Restoring NASA's Technological Edge and Paving the Way for a New Era in Space. (New York 2012).

12 Hurlbert, K., Bagdigian, B., Jeevarajan, A., Kliss, M. & Singh, B. National Aeronautics and Space Administration DRAFT Human Health, Life Support and Habitation Systems Technology Area. (2010).

13 Link, D. E., Carter, D.L., Higbie, S. Development of an Advanced Recycle Filter Tank Assembly for the ISS Urine Processor Assembly. *American Institute of Aeronautics and Astronautics.* 1-8

14 Eslamian, S. *Urban water reuse handbook*; CRC Press 2016.

15 Suffet, I. H. M., J.;Kawczynski, E.;AWWA Research Foundation.;Lyonnaise des eaux Advances in taste-and-odor treatment and control. (AWWA Research Foundation and Lyonnaise des Eaux, Denver, 1995).

16 Ettouney, H. M.;El-Dessouky, H. T.;Faibish, R. S.;Gowin, P. J. Evaluating the economics of desalination. *Chem Eng Prog.* **2002**, 98, 32-39.

17 Shatat, M.;Riffat, S. B. Water desalination technologies utilizing conventional and renewable energy sources. *Int Jnl of Low-Carbon Technologies.* **2014**, 9, 1-19.

18 Van der Bruggen, B.;Vandecasteele, C. Distillation vs. membrane filtration: overview of process evolutions in seawater desalination. *Desalination.* **2002**, 143, 207-218.

19 Drioli, E. *Encyclopedia of membranes*; Springer Berlin: 2016.

20 Duke, M.;Zhao, D.;Semiat, R. *Functional nanostructured materials and membranes for water treatment*; John Wiley & Sons: 2013.

21 Sagle, A.;Freeman, B. Fundamentals of membranes for water treatment. 137-154 (Texas Water Development Board, Austin, 2004).

22 Reisner, D. E. *Bionanotechnology II : global prospects*; CRC Press: Boca Raton, 2012.

23 McCutcheon, J. R.;McGinnis, R. L.;Elimelech, M. Desalination by ammonia-carbon dioxide forward osmosis: Influence of draw and feed solution concentrations on process performance. *J Membrane Sci.* **2006**, 278, 114-123.

24 Bergman, R. *Reverse osmosis and nanofiltration*; American Water Works Association: Denver, CO, 2007.

25 Ahmed, I., Mohd Yusof, Z., A., Beg, M. D. H. Fabrication of Polymer Based Mix Matrix Membrane - A Short Review. *International Journal of Basic & Applied Sciences.* **2010**, 10, 17.

26 Kesieme, U. K. M., N.; Aral, H.; Cheng, C. Y.; Duke, M. Economic analysis of desalination technologies in the context of carbon pricing, and opportunities for membrane distillation. *Desalination.* **2013**, 323, 66-74.

27 Loeb, S., Sourirajan, S. Seawater dimineralization by means of an osmotic membrane. *Advances in Chemistry Series.* **1963**, 38, 117-132.

28 Hobbs, C.;Hong, S. K.;Taylor, J. Effect of membrane properties on fouling in RO/NF membrane filtration of surficial groundwater. *Abstr Pap Am Chem S.* **2000**, 220, U322-U322.

29 Boerlage, S. F. *Scaling and Particulate Fouling in Membrane Filtration Systems*; CRC Press: 2001.

30 Belfort, G. Pretreatment and Cleaning of Hyperfiltration (Reverse-Osmosis) Membranes in Municipal Wastewater Renovation. *Desalination.* **1977**, 21, 285-300.

31 Benjamin, M. M.;AWWA Research Foundation. *Combining adsorbents with membranes for water treatment*; AWWA Research Foundation and American Water Works Association: Denver, CO, 2002.

32 Amjad, Z. *Reverse osmosis : membrane technology, water chemistry & industrial applications*; Van Nostrand Reinhold: New York, 1993.

33 Malaeb, L.;Ayoub, G. M. Reverse osmosis technology for water treatment: State of the art review. *Desalination.* **2011**, 267, 1-8.

34 Hilal, N.;Khayet, M.;Wright, C. J. *Membrane modification : technology and applications*; Taylor & Francis: Boca Raton, 2012.

35 Wang, L. K. *Membrane and desalination technologies*; Humana Press: New York, NY, 2011.

36 Federal Laboratory Technology Transfer. (National Institute of Standards and Technology, 2009).

37 Li, D., Yan, Y., Wang H.,. Recent advances in polymer and polymer composite membranes for reverse and forward osmosis processes. *Prog Polym Sci.* **2016**, 61, 104–155.

38 Petersen, R. J. Composite Reverse-Osmosis and Nanofiltration Membranes. *J Membrane Sci.* **1993**, 83, 81-150.

39 Lee, S.;Lueptow, R. M. Membrane rejection of nitrogen compounds. *Environ Sci Technol.* **2001**, 35, 3008-3018.

40 Khosravi, A.;Sadeghi, M.;Banadkohi, H. Z.;Talakesh, M. M. Polyurethane-Silica Nanocomposite Membranes for Separation of Propane/Methane and Ethane/Methane. *Ind Eng Chem Res.* **2014**, 53, 2011-2021.

41 Lind, M. L., Fink, S., Sasaki, K., Lin, J. . Nanocomposite membranes. USA patent WO2014159352 A1 (2014).

42 Van Herk, A. M., Landfester, Katharina *Hybrid Latex Particles: Preparation with (Mini)emulsion Polymerization*; Springer: 2010.

43 Aligizaki, K. K. *Pore structure of cement-based materials : testing, interpretation and requirements*; Taylor & Francis: Abingdon England ; New York, 2006.

44 Ngai, K. L. *Relaxation and diffusion in complex systems*; Springer: New York, 2011.

45 Ozerov, R. P.;Vorobyev, A. A. *Physics for chemists*; Elsevier: Boston, 2007.

46 Smirnov, I. V., Vysotskii, V.I., Kornilova, A.A. *Introduction to the Biophysics of Activated Water* Universal Publishers 2005.

47 Berl, W. G. *Physical methods in chemical analysis*; Academic Press: New York,, 1960.

48 Geise, G. M.;Paul, D. R.;Freeman, B. D. Fundamental water and salt transport properties of polymeric materials. *Prog Polym Sci.* **2014**, 39, 1-42.

49 Nightingale, E. R. Phenomenological Theory of Ion Solvation - Effective Radii of Hydrated Ions. *J Phys Chem-Us.* **1959**, 63, 1381-1387.

50 Keddie, J. L.;Routh, A. F. *Fundamentals of latex film formation : processes and properties*; Springer: Dordrecht ; New York, 2010.

51 Mariz, I. D. A.;Millichamp, I. S.;de la Cal, J. C.;Leiza, J. R. High performance water-borne paints with high volume solids based on bimodal latexes. *Prog Org Coat.* **2010**, 68, 225-233.

52 Peng, Y. X.;Zheng, Z. H.;Bin Ding, X.;Zhang, W. C.;Ye, Z. H. Nanometer polymer latex dispersion and its application in water-based coating. *Prog Org Coat.* **2003**, 48, 161-163.

53 Butt, H. J.;Kuropka, R.;Christensen, B. Latex Film Formation Studied with the Atomic-Force Microscope - Influence of Aging and Annealing. *Colloid Polym Sci.* **1994**, 272, 1218-1223.

54 Man, W. N.;Russel, W. B. Direct measurements of critical stresses and cracking in thin films of colloid dispersions. *Phys Rev Lett.* **2008**, 100

55 Steward, P. A.;Hearn, J.;Wilkinson, M. C. An overview of polymer latex film formation and properties. *Adv Colloid Interfac.* **2000**, 86, 195-267.

56 Brown, G. L. Formation of Films from Polymer Dispersions. *J Polym Sci.* **1956**, 22, 423-434.

57 Dillon, R. E.;Matheson, L. A.;Bradford, E. B. Sintering of Synthetic Latex Particles. *J Coll Sci Imp U Tok.* **1951**, 6, 108-117.

58 Feng, J. R.;Winnik, M. A.;Shivers, R. R.;Clubb, B. Polymer Blend Latex Films - Morphology and Transparency. *Macromolecules.* **1995**, 28, 7671-7682.

59 Kan, C. S. Role of particle size on latex deformation during film formation. *J Coating Technol.* **1999**, 71, 89-97.

60 Lively, R. P.;Mysona, J. A.;Chance, R. R.;Koros, W. J. Formation of Defect-Free Latex Films on Porous Fiber Supports. *ACS Applied Materials & Interfaces.* **2011**, 3, 3568-3582.

61 Provder, T.;Winnik, M. A.;Urban, M. W.;American Chemical Society. Division of Polymeric Materials: Science and Engineering. *Film formation in waterborne coatings*; American Chemical Society: Washington, DC, 1996.

62 Routh, A. F.;Russel, W. B. Deformation mechanisms during latex film formation: Experimental evidence. *Ind Eng Chem Res.* **2001**, 40, 4302-4308.

63 Sheetz, D. P. Formation of Films by Drying of Latex. *J Appl Polym Sci.* **1965**, 9, 3759-&.

64 Tirumkudulu, M. S.;Russel, W. B. Cracking in drying latex films. *Langmuir.* **2005**, 21, 4938-4948.

65 Tirumkudulu, M. S.;Russel, W. B. Role of capillary stresses in film formation. *Langmuir.* **2004**, 20, 2947-2961.

66 Vanderhoff, J. W.;Tarkowski, H. L.;Jenkins, M. C.;Bradford, E. B. Theoretical Consideration of Interfacial Forces Involved in Coalescence of Latex Particles. *Rubber Chemistry and Technology.* **1967**, 40, 1246-1269

67 Richter, K.;Feist, W. C.;Knaebe, M. T. The Effect of Surface-Roughness on the Performance of Finishes .1. Roughness Characterization and Stain Performance. *Forest Prod J.* **1995**, 45, 91-97.

68 Mader, A.;Schiro, A.;Brischetto, M.;Pizzo, B. Interactions and penetration of polymers and nanolatexes into wood: An overview. *Progress in Organic Coatings.* **2011**, 71, 123-135.

69 Plotze, M.;Niemz, P. Porosity and pore size distribution of different wood types as determined by mercury intrusion porosimetry. *Eur J Wood Wood Prod.* **2011**, 69, 649-657.

70 Hunt, C.;Bonura, T.;Mall, D.;Comm, J. C. F. P. Improving the Performance of Painted Wood Siding: Rain Screen, End-Grain Seal, and Back Priming. *Jct Coatingstech.* **2009**, 6, 30-33.

71 Dobler, F.;Holl, Y. Mechanisms of particle deformation during latex film formation. *Film Formation in Waterborne Coatings.* **1996**, 648, 22-43.

72 Winnik, M. A. Latex film formation. *Curr Opin Colloid In.* **1997**, 2, 192-199.

73 Routh, A. F.;Russel, W. B. A process model for latex film formation: Limiting regimes for individual driving forces. *Langmuir.* **1999**, 15, 7762-7773.

74 Petersen, C.;Heldmann, C.;Johannsmann, D. Internal stresses during film formation of polymer latices. *Langmuir.* **1999**, 15, 7745-7751.

75 Ludwig, I.;Schabel, W.;Kind, M.;Castaing, J. C.;Ferlin, P. Drying and film formation of industrial waterborne latices. *Aiche J.* **2007**, 53, 549-560.

76 Eckersley, S. T.;Rudin, A. Mechanism of Film Formation from Polymer Latexes. *J Coating Technol.* **1990**, 62, 89-100.

77 Pekcan, O.;Arda, E. Fluorescence methods for latex film formation. *Acs Sym Ser.* **2005**, 912, 137-165.

78 Ho, C. C.;Khew, M. C. Low glass transition temperature (T-g) rubber latex film formation studied by atomic force microscopy. *Langmuir.* **2000**, 16, 2436-2449.

79 Keddie, J. L. Film formation of latex. *Mat Sci Eng R.* **1997**, 21, 101-170.

80 Wang, Y. C.;Winnik, M. A. Latex Film Formation .3. Effect of a Coalescing Aid on Polymer Diffusion in Latex Films. *Macromolecules.* **1990**, 23, 4731-4732.

81 Crawford, K. S. *Microstructure Formation of Complex Latex Coatings* MASTER OF SCIENCE thesis, UNIVERSITY OF MINNESOTA, **2011**.

82 Cisneros-Zevallos, L.;Krochta, J. M. Dependence of coating thickness on viscosity of coating solution applied to fruits and vegetables by dipping method. *J Food Sci.* **2003**, 68, 503-510.

83 Jensen, D. P.;Morgan, L. W. Particle-Size as It Relates to the Minimum Film Formation Temperature of Lattices. *J Appl Polym Sci.* **1991**, 42, 2845-2849.

84 Gorton, A. D. T. Latex Dipping I. Relationship between Dwell Time, Latex Compound Viscosity and Deposit Thickness. *J. Rubber Res I Malay.* **1967**, 20, 27-35.

85 Blackley, D. C. *Polymer Latices*; Springer Science & Business Media: 1997.

86 Hatakeyama, T.;Liu, Z. *Handbook of thermal analysis*; Wiley: Chichester ; New York, 1998.

87 Lipták, B. G. *Analytical instrumentation*; Chilton: Radnor, Pa., 1994.

88 Lothar Mueller, A. S., Gunnar Lischeid. *Novel measurement and assessment tools for monitoring and management of land and water resources in agricultural landscapes of central Asia*; Springer International Publishing: 2014.

89 Salamone, J. C. *Polymeric materials encyclopedia*; CRC Press: Boca Raton, 1996.

90 Khosravi, A.;King, J. A.;Jamieson, H. L.;Lind, M. L. Latex Barrier Thin Film Formation on Porous Substrates. *Langmuir.* **2014**, 30, 13994-14003.

91 McGinity, J. W.;Felton, L. A. *Aqueous polymeric coatings for pharmaceutical dosage forms*; Informa Healthcare: New York, 2008.

92 Sperry, P. R.;Snyder, B. S.;Odowd, M. L.;Lesko, P. M. Role of Water in Particle Deformation and Compaction in Latex Film Formation. *Langmuir*. **1994**, 10, 2619-2628.

93 Feng, J. *Molecular and environmental aspects of latex film formation* doctor of philosophy thesis, University of Toronto, **1997**.

94 ASM International. *Characterization and failure analysis of plastics*; ASM International: Materials Park, OH, 2003.

95 Benedek, I. *Development and manufacture of pressure-sensitive products*; M. Dekker: New York, 1999.

96 Rigby, D.;Roe, R. J. Molecular-Dynamics Simulation of Polymer Liquid and Glass .1. Glass-Transition. *J Chem Phys.* **1987**, 87, 7285-7292.

97 Takeuchi, H.;Roe, R. J. Molecular-Dynamics Simulation of Local Chain Motion in Bulk Amorphous Polymers .1. Dynamics above the Glass-Transition. *J Chem Phys.* **1991**, 94, 7446-7457.

98 Kodani, T.;Sakai, H.;Takayama, A.;Nomura, M. Effect of storage on film-formation property of vinylidene chloride-acrylonitrile-methyl acrylate terpolymer latex. *J Appl Polym Sci.* **1998**, 69, 573-579.

99 Braun, D. *Polymer synthesis : theory and practice : fundamentals, methods, experiments*; Springer: Berlin ; New York, 2005.

100 Gedde, U. W. *Polymer Physics*; Chapman & Hall,: London 1995, 1995.

101 Bico, J.;Thiele, U.;Quere, D. Wetting of textured surfaces. *Colloid Surface A.* **2002**, 206, 41-46.

102 Bico, J.;Tordeux, C.;Quere, D. Rough wetting. *Europhys Lett.* **2001**, 55, 214-220.

103 Cassie, A. B. D.;Baxter, S. Wettability of porous surfaces. *T Faraday Soc.* **1944**, 40, 0546-0550.

104 Meiron, T. S.;Marmur, A.;Saguy, I. S. Contact angle measurement on rough surfaces. *J Colloid Interf Sci.* **2004**, 274, 637-644.

105 Rodriguez-Valverde, M. A.;Cabrerizo-Vilchez, M. A.;Rosales-Lopez, P.;Paez-Duenas, A.;Hidalgo-Alvarez, R. Contact angle measurements on two (wood and stone) non-ideal surfaces. *Colloid Surface A.* **2002**, 206, 485-495.

106 Takahira, N.;Yoshikawa, T.;Tanaka, T.;Holappa, L. Wettability of liquid in and Bi on flat and porous solid iron substrate. *Mater Trans.* **2007**, 48, 2708-2711.

107 Mittal, K. L. Vol. 5 52 (Technology & Engineering, 2009).

108 Leonardo, R. G. Film Formation - Aspects on the Coalescence of Latex-Particles. *Makromol Chem-M Symp.* **1990**, 35-6, 389-404.

109 Schantz, S., Carlsson, H. T., Andersson, T., Erkselius, S., Larsson, A., Karlsson, O. J. Poly(methyl methacrylate-co-ethyl acrylate) latex particles with poly(ethylene glycol) grafts: Structure and film formation. *Langmuir.* **2007**, 23, 3590-3602.

110 Jamieson, H. L.;Yin, H. D.;Waller, A.;Khosravi, A.;Lind, M. L. Impact of acids on the structure and composition of Linde Type A zeolites for use in reverse osmosis membranes for recovery of urine-containing wastewaters. *Micropor Mesopor Mat.* **2015**, 201, 50-60.

111 Cadotte, J. E.;Petersen, R. J.;Larson, R. E.;Erickson, E. E. New Thin-Film Composite Seawater Reverse-Osmosis Membrane. *Desalination.* **1980**, 32, 25-31.

112 Glater, J.;Hong, S. K.;Elimelech, M. The Search for a Chlorine-Resistant Reverse-Osmosis Membrane. *Desalination.* **1994**, 95, 325-345.

113 Glater, J.;Zachariah, M. R.;Mccray, S. B.;Mccutchan, J. W. Reverse-Osmosis Membrane Sensitivity to Ozone and Halogen Disinfectants. *Desalination.* **1983**, 48, 1-16.

114 Kawaguchi, T.;Tamura, H. Chlorine-Resistant Membrane for Reverse-Osmosis .1. Correlation between Chemical Structures and Chlorine Resistance of Polyamides. *J Appl Polym Sci.* **1984**, 29, 3359-3367.

115 Kawaguchi, T.;Tamura, H. Chlorine-Resistant Membrane for Reverse-Osmosis .2. Preparation of Chlorine-Resistant Polyamide Composite Membranes. *J Appl Polym Sci.* **1984**, 29, 3369-3379.

116 Shin, D. H.;Kim, N.;Lee, Y. T. Modification to the polyamide TFC RO membranes for improvement of chlorine-resistance. *J Membrane Sci.* **2011**, 376, 302-311.

117 Khosravi, A.;Sadeghi, M. Separation performance of poly(urethane-urea) membranes in the separation of C-2 and C-3 hydrocarbons from methane. *J Membrane Sci.* **2013**, 434, 171-183.

118 Utracki, L. A. *Polymer blends handbook*; Kluwer Academic Publishers: Dordrecht ; Boston, 2002.

119 Lobo, H., Bonilla, Jose V. *Handbook of Plastics Analysis (Plastics Engineering)*; CRC Press: 2003.

120 Scheirs, J. *Compositional and failure analysis of polymers : a practical approach*; Wiley: Chichester ; New York, 2000.

121 Koch, N.;Ueno, N.;Wee, A. T. S. *The molecule-metal interface*;

122 Mark, J. E. *Physical properties of polymers handbook*; AIP Press: Woodbury, N.Y., 1996.

123 Dhoot, G. *Estimation of Eugenol Diffusion Coefficient in LLDPE Using FTIR-ATR Flow Cell and HPLC Techniques*; Michigan State University: 2008.

124 Ismail, A. A.;Mohamed, R. M.;Ibrahim, I. A.;Kini, G.;Koopman, B. Synthesis, optimization and characterization of zeolite A and its ion-exchange properties. *Colloid Surface A.* **2010**, 366, 80-87.

125 Mohamed, R. M.;Ismail, A. A.;Kini, G.;Ibrahim, I. A.;Koopman, B. Synthesis of highly ordered cubic zeolite A and its ion-exchange behavior. *Colloid Surface A.* **2009**, 348, 87-92.

126 Kirk, R. E.;Othmer, D. F.;Kroschwitz, J. I.;Howe-Grant, M. *Encyclopedia of chemical technology*; Wiley: New York, 1991.

127 Wang, R.;Wang, L.;Wu, J. *Adsorption refrigeration technology : theory and application*;

128 Bagchi, B. *Water in biological and chemical processes : from structure and dynamics to function*;

129 Johnson, A. T. *Biology for engineers*; CRC Press: Boca Raton, FL, 2011.

130 Banerje, R., Phan, A. , Wang, B., Knobler, C., Furukawa, H. , O'Kefe, M. , Yaghi, O. M. Highthroughput synthesis of zeolitc imidazolate frameworks and aplication to CO2 capture. *Science.* **2008**, 319, 939-943.

131 Esmaeili, N.;Kazemian, H.;Bastani, D. Synthesis of Nano Particles of LTA Zeolite by Means of Microemulsion Technique. *Iran J Chem Chem Eng.* **2011**, 30, 1-8.

132 Navarro, M. *et al.* Laser Control of Zeolite Nucleation. *Chemphyschem.* **2012**, 13, 736-740.

133 Madsen, C.;Jacobsen, C. J. H. Nanosized zeolite crystals - convenient control of crystal size distribution by confined space synthesis. *Chem Commun.* **1999**, 673-674.

134 Jawor, A.;Jeong, B. H.;Hoek, E. M. V. Synthesis, characterization, and ion-exchange properties of colloidal zeolite nanocrystals. *J Nanopart Res.* **2009**, 11, 1795-1803.

135 Wang, H. T.;Holmberg, B. A.;Yan, Y. S. Synthesis of template-free zeolite nanocrystals by using in situ thermoreversible polymer hydrogels. *J Am Chem Soc.* **2003**, 125, 9928-9929.

136 Esmaeili, N.;Kazemian, H.;Bastani, D. Controlled Crystallization of LTA Zeolitic Nanoparticles from a Clear Solution Using Organic Template. *Iran J Chem Chem Eng.* **2011**, 30, 9-14.

137 Koroglu, H. J.;Sarioglan, A.;Tatlier, M.;Erdem-Senatalar, A.;Savasci, O. T. Effects of low-temperature gel aging on the synthesis of zeolite Y at different alkalinities. *J Cryst Growth.* **2002**, 241, 481-488.

138 Li, Z. J.;Lew, C. M.;Li, S.;Medina, D. I.;Yan, Y. S. Pure-silica-zeolite MEL low-k films from nanoparticle suspensions. *J Phys Chem B.* **2005**, 109, 8652-8658.

139 Wang, H. T.;Holmberg, B. A.;Yan, Y. S. Homogeneous polymer-zeolite nanocomposite membranes by incorporating dispersible template-removed zeolite nanocrystals. *J Mater Chem.* **2002**, 12, 3640-3643.

140 Steen, E., V. ; Callanan, L. H. in *Proceedings of the 14th International Zeolite Conference.* (ed E. Steen, V. ; Callanan, L. H.) 248 (Gulf Professional Publishing).

141 Li, Q. H.;Mihailova, B.;Creaser, D.;Sterte, J. Aging effects on the nucleation and crystallization kinetics of colloidal TPA-silicalite-l. *Microporous and Mesoporous Materials.* **2001**, 43, 51-59.

142 Mintova, S.;Olson, N. H.;Valtchev, V.;Bein, T. Mechanism of zeolite a nanocrystal growth from colloids at room temperature. *Science.* **1999**, 283, 958-960.

143 Vekilov, P. G. Nucleation. *Cryst Growth Des.* **2010**, 10, 5007-5019.

144 Zhang, X. Q. *Kinetic Monte Carlo modelling of the initial stages of zeolite synthesis*, Eindhoven: Technische Universiteit Eindhoven, **2012**.

145 Couldry, N. *Media, society, world : social theory and digital media practice*; Polity: Cambridge ; Malden, MA, 2012.

146 Robson, H. E. *Verified syntheses of zeolitic materials*; Elsevier: Amsterdam ; New York, 2001.

147 Cao, G.;Wang, Y. *Nanostructures & nanomaterials : synthesis, properties, and applications*; World Scientific: New Jersey, 2011.

148 Aguilera, J. M.;Lillford, P. *Food materials science : principles and practice*; Springer: New York, 2008.

149 Mullin, J. W. *Crystallization*; Butterworth-Heinemann: Oxford ; Boston, 2001.

150 Ottens, M. *et al.* Impurity effects on the crystallization kinetics of ampicillin. *Ind Eng Chem Res.* **2004**, 43, 7932-7938.

151 Dougall, D. S. *A Protein Sequence-properties Evaluation Framework for Crystallization Screen Design*; ProQuest: University of Pittsburgh, 2007.

152 Fulcher, J. *Water-Recycling Technology in Space Evolves*, 2013).

153 Feoktistova, N. N.;Zhdanov, S. P. On the Kinetics of Crystallization of Silicalite-I. *Zeolites.* **1989**, 9, 136-139.

154 Mintova, S.;Valtchev, V.;Vultcheva, E.;Veleva, S. Crystallization Kinetics of Zeolite Zsm-5. *Zeolites.* **1992**, 12, 210-215.

155 Abyzov, A. S.;Schmelzer, J. W. P. Nucleation versus spinodal decomposition in confined binary solutions. *J Chem Phys.* **2007**, 127

156 Atkins, P. W.;De Paula, J. *Elements of physical chemistry*; Oxford University Press: Oxford, 2013.

157 Gebauer, D.;Kellermeier, M.;Gale, J. D.;Bergstrom, L.;Colfen, H. Pre-nucleation clusters as solute precursors in crystallisation. *Chem Soc Rev.* **2014**, 43, 2348-2371.

158 Alfaro, S.;Rodriguez, C.;Valenzuela, M. A.;Bosch, P. Aging time effect on the synthesis of small crystal LTA zeolites in the absence of organic template. *Mater Lett.* **2007**, 61, 4655-4658.

159 Bronić, J., Subotić, B., Smit, I., Despotović, L.J.A. Influence of Gel Ageing on Zeolite Nucleation Processes. *Studies in Surface Science and Catalysis.* **1988**, 37, 107-114.

160 Feoktistova, N. N.;Vtyurina, L. M. Temperature-Dependence of Naa Zeolite Nucleation in Silicoalumina Gels. *B Acad Sci Ussr Ch+*. **1988**, 37, 617-619.

161 Szostak, R. *Molecular sieves : principles of synthesis and identification*; Blackie Academic & Professional: London ; New York, 1998.

162 Bronic, I. K.;Srdoc, D.;Obelic, B. The Mean Energy Required to Form an Ion-Pair for Low-Energy Photons and Electrons in Polyatomic Gases. *Radiat Res.* **1988**, 115, 213-222.

163 Jones, A. G. *Crystallization process systems*; Butterworth-Heinemann: Oxford ; Boston, 2002.

164 Zhdanov, S. P. S., N.N. . in *The Fifth International Conference on Zeolites.* (ed L.V.C. Rees) 75-84.

165 Zhang, X. Q.;van Santen, R. A.;Jansen, A. P. J. Kinetic Monte Carlo modeling of silicate oligomerization and early gelation. *Phys Chem Chem Phys.* **2012**, 14, 11969-11973.

166 Madras, G.;McCoy, B. J. Transition from nucleation and growth to Ostwald ripening. *Chem Eng Sci.* **2002**, 57, 3809-3818.

167 Yang, J. A.;McCoy, B. J.;Madras, G. Cluster kinetics and dynamics during spinodal decomposition. *J Chem Phys.* **2006**, 124

168 Goldburg, W. I.;Shaw, C. H.;Huang, J. S.;Pilant, M. S. Spinodal Decomposition in a Binary-Liquid Mixture. *J Chem Phys.* **1978**, 68, 484-494.

169 Schmelzer, J. W. P.;Abyzov, A. S.;Moller, J. Nucleation versus spinodal decomposition in phase formation processes in multicomponent solutions. *J Chem Phys.* **2004**, 121, 6900-6917.

170 Marro, J.;Valles, J. L. Relevance of the Cahn-Hilliard-Cook Theory at Early Times in Spinodal Decomposition. *Phys Lett A.* **1983**, 95, 443-446.

171 Riste, T. *Fluctuations, instabilities, and phase transitions : [proceedings]*; Plenum Press: New York, 1975.

172 Cahn, J. W. Phase Separation by Spinodal Decomposition in Isotropic Systems. *J Chem Phys.* **1965**, 42, 93-&.

173 Vekilov, P. G. The two-step mechanism of nucleation of crystals in solution. *Nanoscale.* **2010**, 2, 2346-2357.

174 Fink, J. K. *Handbook of Engineering and Specialty Thermoplastics, Water Soluble Polymers*; John Wiley & Sons: 2011.

175 Ruberti, J.;Braithwaite, G. Systems and methods for controlling and forming polymer gels. USA patent (2004).

176 Madras, G.;McCoy, B. J. Denucleation rates during Ostwald ripening: Distribution kinetics of unstable clusters. *J Chem Phys.* **2002**, 117, 6607-6613.

177 Madras, G.;McCoy, B. J. Distribution kinetics theory of Ostwald ripening. *J Chem Phys.* **2001**, 115, 6699-6706.

178 Raja, K. *et al.* Sol-gel synthesis and characterization of alpha-Fe2O3 nanoparticles. *Superlattice Microst.* **2015**, 86, 306-312.

179 Sattler, K. D. *Handbook of nanophysics. Nanoparticles and quantum dots*; Taylor & Francis: Boca Raton, 2011.

180 Thessing, J.;Qian, J. H.;Chen, H. Y.;Pradhan, N.;Peng, X. G. Interparticle influence on size/size distribution evolution of nanocrystals. *J Am Chem Soc.* **2007**, 129, 2736-+.

181 Madras, G.;McCoy, B. J. Temperature effects on the transition from nucleation and growth to Ostwald ripening. *Chem Eng Sci.* **2004**, 59, 2753-2765.

182 Twomey, T. A. M.;Mackay, M.;Kuipers, H. P. C. E.;Thompson, R. W. In-Situ Observation of Silicalite Nucleation and Growth - a Light-Scattering Study. *Zeolites.* **1994**, 14, 162-168.

183 Katovic, A.;Subotic, B.;Smit, I.;Despotovic, L. A.;Curic, M. Role of Gel Aging in Zeolite Crystallization. *Acs Symposium Series.* **1989**, 398, 124-139.

184 Androulakis, J. *et al.* Spinodal decomposition and nucleation and growth as a means to bulk nanostructured thermoelectrics: Enhanced performance in Pb1-xSnxTe-PbS. *J Am Chem Soc.* **2007**, 129, 9780-9788.

185 Hays, C. C.;Kim, C. P.;Johnson, W. L. Large supercooled liquid region and phase separation in the Zr-Ti-Ni-Cu-Be bulk metallic glasses. *Appl Phys Lett.* **1999**, 75, 1089-1091.

186 Degennes, P. G. Dynamics of Fluctuations and Spinodal Decomposition in Polymer Blends. *J Chem Phys.* **1980**, 72, 4756-4763.

187 Kyu, T.;Lee, J. H. Nucleation initiated spinodal decomposition in a polymerizing system. *Physical Review Letters.* **1996**, 76, 3746-3749.

188 Pincus, P. Dynamics of Fluctuations and Spinodal Decomposition in Polymer Blends .2. *J Chem Phys.* **1981**, 75, 1996-2000.

189 Winkler, A.;Virnau, P.;Binder, K.;Winkler, R. G.;Gompper, G. Hydrodynamic mechanisms of spinodal decomposition in confined colloid-polymer mixtures: A multiparticle collision dynamics study. *J Chem Phys.* **2013**, 138

190 Bukusoglu, E.;Pal, S. K.;de Pablo, J. J.;Abbott, N. L. Colloid-in-liquid crystal gels formed via spinodal decomposition. *Soft Matter.* **2014**, 10, 1602-1610.

191 Bronic, J.;Palcic, A.;Subotic, B.;Itani, L.;Valtchev, V. Influence of alkalinity of the starting system on size and morphology of the zeolite A crystals. *Mater Chem Phys.* **2012**, 132, 973-976.

192 Khosravi, A. *et al.* Coarsening and Spinodal Decomposition of Zeolite Linde Type A Precursor Gels Aged at Low Temperatures. *Cryst Growth Des.* **2016**, 16, 3224-3230.

193 Treacy M.M.J., H. J. B. Collection of Simulated XRD Powder Patterns for Zeolites. *Elsevier, Amsterdam.* **2001**,

194 Iwama, M. *et al.* Location of Alkali Ions and their Relevance to Crystallization of Low Silica X Zeolite. *Cryst Growth Des.* **2010**, 10, 3471-3479.

195 Ismail, A. F., Khulbe, K., Matsuura, T. *Gas Separation Membranes: Polymeric and Inorganic*; Springer: 2015.

196 Ogura, M.;Kawazu, Y.;Takahashi, H.;Okubo, T. Aluminosilicate species in the hydrogel phase formed during the aging process for the crystallization of FAU zeolite. *Chem Mater.* **2003**, 15, 2661-2667.

197 Bhatia, S. *Zeolite catalysis : principles and applications*; CRC Press: Boca Raton, Fla., 1990.

198 Ginter, D. M.;Bell, A. T.;Radke, C. J. The Effects of Gel Aging on the Synthesis of Nay Zeolite from Colloidal Silica. *Zeolites.* **1992**, 12, 742-749.

199 Hu, M.;Mi, B. X. Enabling Graphene Oxide Nanosheets as Water Separation Membranes. *Environ Sci Technol.* **2013**, 47, 3715-3723.

200 Agenson, K. O.;Oh, J. I.;Urase, T. Retention of a wide variety of organic pollutants by different nanofiltration/reverse osmosis membranes: controlling parameters of process. *J Membrane Sci.* **2003**, 225, 91-103.

201 KastelanKunst, L.;Kosutic, K.;Dananic, V.;Kunst, B. FT30 membranes of characterized porosities in the reverse osmosis organics removal from aqueous solutions. *Water Res.* **1997**, 31, 2878-2884.

202 Ozaki, H.;Li, H. F. Rejection of organic compounds by ultra-low pressure reverse osmosis membrane. *Water Res.* **2002**, 36, 123-130.

203 Schutte, C. F. The rejection of specific organic compounds by reverse osmosis membranes. *Desalination.* **2003**, 158, 285-294.

204 Radjenovic, J.;Petrovic, M.;Ventura, F.;Barcelo, D. Rejection of pharmaceuticals in nanofiltration and reverse osmosis membrane drinking water treatment. *Water Res.* **2008**, 42, 3601-3610.

205 Choi, S. Y.;Lee, Y. J.;Park, Y. S.;Ha, K.;Yoon, K. B. Monolayer assembly of zeolite crystals on glass with fullerene as the covalent linker. *J Am Chem Soc.* **2000**, 122, 5201-5209.

206 Ha, K.;Lee, Y. J.;Lee, H. J.;Yoon, K. B. Facile assembly of zeolite monolayers on glass, silica, alumina, and other zeolites using 3-halopropylsilyl reagents as covalent linkers. *Adv Mater.* **2000**, 12, 1114-+.

207 Kulak, A. *et al.* Polyamines as strong molecular linkers for monolayer assembly of zeolite crystals on flat and curved glass. *J Am Chem Soc.* **2000**, 122, 9308-9309.

208 Lee, G. S.;Lee, Y. J.;Ha, K.;Yoon, K. B. Orientation-controlled monolayer assembly of zeolite crystals on glass using terephthaldicarboxaldehyde as a covalent linker. *Tetrahedron.* **2000**, 56, 6965-6968.

209 Mcgovern, M. E.;Kallury, K. M. R.;Thompson, M. Role of Solvent on the Silanization of Glass with Octadecyltrichlorosilane. *Langmuir.* **1994**, 10, 3607-3614.

210 Szczepanski, V.;Vlassiouk, I.;Smirnov, S. Stability of silane modifiers on alumina nanoporous membranes. *J Membrane Sci.* **2006**, 281, 587-591.

211 Ha, K.;Lee, Y. J.;Jung, D. Y.;Lee, J. H.;Yoon, K. B. Micropatterning of oriented zeolite monolayers on glass by covalent linkage. *Adv Mater.* **2000**, 12, 1614-+.

212 Chun, Y. S. *et al.* Diisocyanates as novel molecular binders for monolayer assembly of zeolite crystals on glass. *Chem Commun.* **2002**, 1846-1847.

213 Park, J. S.;Lee, G. S.;Lee, Y. J.;Park, Y. S.;Yoon, K. B. Organization of microcrystals on glass by adenine-thymine hydrogen bonding. *J Am Chem Soc.* **2002**, 124, 13366-13367.

214 Hobler, C.;Bakowsky, U.;Keusgen, M. A functional immobilization of semiconductor nanoparticles (quantum dots) on nanoporous aluminium oxide. *Phys Status Solidi A.* **2010**, 207, 872-877.

215 Vlassiouk, I.;Takmakov, P.;Smirnov, S. Sensing DNA hybridization via ionic conductance through a nanoporous electrode. *Langmuir.* **2005**, 21, 4776-4778.

216 Vlassiouk, I.;Krasnoslobodtsev, A.;Smirnov, S.;Germann, M. "Direct" detection and separation of DNA using nanoporous alumina filters. *Langmuir.* **2004**, 20, 9913-9915.

217 Shun'koa, E. V.;Belkin, V. S. Cleaning properties of atomic oxygen excited to metastable state 2s(2)2p(4)(S-1(0)). *J Appl Phys.* **2007**, 102

218 Yong, J. S.;Phillip, W. A.;Elimelech, M. Coupled reverse draw solute permeation and water flux in forward osmosis with neutral draw solutes. *J Membrane Sci.* **2012**, 392, 9-17.

219 Yoon, Y.;Lueptow, R. M. Reverse osmosis membrane rejection for ersatz space mission wastewaters. *Water Res.* **2005**, 39, 3298-3308.